8-10-2020

High Conductivity Metal–Carbon Nanotube Hybrid Conductors via Chemical Vapor Deposition and Electroplating

Anthony P. Leggiero
apl5353@rit.edu

R·I·T

High Conductivity Metal–Carbon Nanotube Hybrid Conductors via Chemical Vapor Deposition and Electroplating

by

Anthony P. Leggiero

A dissertation submitted in partial fulfillment of the requirements
for the degree of Doctorate of Philosophy in Microsystems Engineering

Microsystems Engineering Program
Kate Gleason College of Engineering

Rochester Institute of Technology
Rochester, New York
10 August 2020

High Conductivity Metal–Carbon Nanotube Hybrid Conductors via Chemical Vapor Deposition and Electroplating

by
Anthony P. Leggiero

Committee Approval:

We, the undersigned committee members, certify that we have advised and/or supervised the candidate on the work described in this dissertation. We further certify that we have reviewed the dissertation manuscript and approve it in partial fulfillment of the requirements of the degree of Doctor of Philosophy in Microsystems Engineering.

_____

Dr. Brian J. Landi — Date
Professor, Department of Chemical Engineering

_____

Dr. Parsian K. Mohseni — Date
Assistant Professor, Department of Microsystems Engineering

_____

Dr. Ivan Puchades — Date
Assistant Professor, Department of Electrical and Microelectronic Engineering

_____

Dr. John-David R. Rocha — Date
Assistant Professor, School of Chemistry and Materials Science

_____

Dr. Cory D. Cress — Date
Materials Research Engineer, U.S. Naval Research Laboratory

Certified by:

_____

Dr. Bruce W. Smith — Date
Director, Microsystems Engineering Program

ABSTRACT

Kate Gleason College of Engineering
Rochester Institute of Technology

Degree: Doctor of Philosophy **Program:** Microsystems Engineering

Authors Name: Anthony P. Leggiero

Advisors Name: Dr. Brian J. Landi

Dissertation Title: High Conductivity Metal–Carbon Nanotube Hybrid Conductors via Chemical Vapor Deposition and Electroplating

Metal-carbon nanotube (CNT) hybrid conductors aim to combine the high conductivity of traditional metals with the low mass and temperature coefficient of resistance (TCR) of carbon nanotubes. The high conductivity of copper makes it a promising candidate to combine with CNTs in a hybrid structure, but there is limited physical and electrical interaction between copper and CNTs. The use of an interfacial layer offers one method of improving the interconnection of a Cu-CNT hybrid conductor. In this dissertation, a joule heating-driven chemical vapor deposition (CVD) technique is developed to deposit nanometal seeds throughout a porous, low-density (0.12 g/cm^3, ~9 mg/m) CNT roving template. Modification of the applied current to the CNT roving allows for the tuning of depositions towards either hot-spot site-specificity or overall uniformity. The effects of temperature, pressure, precursor mass, and the interval of applied current are investigated, demonstrating nanometal depositions ranging from less than 5 % w/w to over 85 % w/w. The versatility of CVD allows for a wide variety of metals to be deposited including copper, nickel, silver, tungsten, palladium, platinum, ruthenium, rhodium, and iridium. In particular, platinum acetylacetonate [$Pt(acac)_2$] deposits with enhanced adhesion to the CNT roving and exhibits smaller nanometal seed diameters of 5 nm compared to 40 nm for copper. The $Pt(acac)_2$ depositions also lead to improvements in the resistance of seeded CNTs across all mass loadings studied, with the largest improvements to the specific conductivity measured with 20-50 % w/w platinum seeds. CVD seeded CNT conductors with ~30 % w/w platinum are electroplated with copper, densified, and annealed produce Cu-CNT hybrid conductors with specific conductivities as high as 5772 $S \cdot m^2/kg$ and TCR (from 300–600 K) as low as 2.74×10^{-3} K^{-1}, indicating good interconnection of the metal and CNT portions. Room temperature electrical conductivities of 29.8 MS/m are achieved, comparable to traditional metallic electrical conductors like aluminum and copper. High conductivity, low TCR electrical conductors such as the nanometal interconnected Cu-CNT hybrids have numerous future applications towards high efficiency motors, generators, and transformers.

ACKNOWLEDGMENTS

I would like to thank my advisor, Dr. Brian Landi, for his guidance and mentorship. Through the various projects, milestones, and life events he has been a constant source of encouragement and support. He has provided me with a tremendous opportunity at RIT in the NanoPower Research Laboratories, and his focus on a healthy work–life balance has made the rigors of the PhD process not only manageable, but enjoyable. He has helped me to grow in my research, presentation, publication, and interpersonal skills. It has been a pleasure to have been a part of his research group for the past five years.

I would like to thank my committee: Dr. Ivan Puchades, Dr. Cory Cress, Dr. Parsian Mohseni, and Dr. John-David Rocha. Their support in my research cannot be overstated. I have learned much from them both in class and in project discussions. I owe them all my deepest gratitude for their contributions to my progress and successes. I would also like to thank Microsystems Engineering Department Head, Dr. Bruce Smith.

I would like to also give a special thanks and acknowledgement to the staff who make day to day operations possible including Stephanie Hart, Lisa Zimmerman, Elaine Lewis, Jim Smith, and Ross Hisert.

I would like to thank all of my friends and colleagues in NPRL and the Microsystems program including Ali Abrand, Mohad Baboli, Dan Broderick, Nate Cox, Kyle Crompton, Martin Dann, Mike Fanto, Anastasiia Fedorenko, Matthew Ganter, Meng Hsu, Arvind Jaikumar, Xi Li, Elizabeth McClure, Dylan McIntyre, Andrew Merrill, Steve Polly, Aaron Rape, Jamie Rossi, Chris Schauerman, Karen Soule, Jason Staub, Paul Thomas, Alex Tomkiewicz, Thomas Wilhelm, Yali Zhang, and any others that I may have missed. Through all of the times we've spent in the lab, in classes, playing board games, at McGregors, or downtown – the friendship and camaraderie are what have made the challenges of the PhD program possible.

I owe a special debt of gratitude to the undergraduates and graduate students that I have had the privilege of working with during my Ph.D. studies including Kylie Trettner, Heather Ursino, Erin Loughran, Shannon Driess, and Meleni Sarantos. Their contributions and insights into the work have been invaluable.

I would like to thank my coworkers and friends from Corning for all of their support and encouragement as I was considering leaving for RIT, especially Shivani, Chris, Steve, Rahul, Catherine, Andy, Anders, and Michael. I would also like to give a special mention to Dr. Kishor Gadkaree who motivated me to further my academic studies.

Finally, I would like to give a special thanks to my family, who have supported me throughout the Ph.D. process. My wife, my love, Irene, who was willing to uproot our lives and move for my studies. She has been especially patient over the five years of late nights and sometimes irregular schedules. My mother, who has always been only a call away. My brothers, who have always been there for me. And finally my in-laws for all of their help (especially with childcare) over the past few years.

TABLE OF CONTENTS

TABLE OF FIGURES

CHAPTER 1: INTRODUCTION

1.1. Carbon Nanotube Conductors: Translating Nano to Macro

Graphite is the most commonly occurring natural allotrope of carbon in nature. It consists of stacked sheets of Sp^2-bonded carbon atoms in a hexagonal alignment. An individual, atomically thin layer of graphite is known as graphene. Carbon nanotubes are an allotrope of carbon that can be envisioned as a sheet of graphene rolled into a tubular form. A CNT may consist of a single cylindrical layer of graphene, creating a single-wall CNT, or multiple concentric cylindrical layers, creating a multi-walled CNT [1,2]. A special case is that of a double-walled CNT, consisting of exactly two concentric cylindrical layers [1].

The way in which the graphene sheet is rolled determines the characteristics of the CNT. This property is quantified as the nanotube's chiral vector, which takes the form:

$$C_h = n\hat{a}_1 + m\hat{a}_2$$

and connects two crystallographically equivalent points on the graphene sheet [2]. In this equation, $\hat{a}_1$ and $\hat{a}_2$ represent the basis vectors of graphene, and *n* and *m* are integers known as indices. The length of the chiral vector is related to the circumference of the carbon nanotube. The *n* and *m* indices represent the chiral angle θ of the nanotube as [3]:

$$\theta = \tan^{-1}\left[\frac{\sqrt{3}n}{2m+n}\right]$$

The chiral angle may vary between $0° \leq \theta \leq 30°$ with $m \leq n$. For the special cases where $\theta = 30°$ and $m = n$ a nanotube is said to be in the "armchair" configuration. Likewise, when $\theta = 0°$ and $m = 0$ a nanotube is said to be in the "zigzag" configuration. All angles in between are said to be "chiral" nanotubes [2,3]. Armchair nanotubes are all metallic (specifically, zero bandgap semimetals). Zigzag and chiral tubes may either be semimetals when $\frac{n-m}{3} = i$ (an integer), or semiconductors otherwise (with bandgap dependent on tube diameter).[3] Thus, the (n, m) indices are a useful metric for the identification of single-walled nanotubes, as in e.g. a (7,7) armchair nanotube [2].

An approximation of the electronic properties of nanotubes may be understood through examination of the band structure of graphene. Graphene has bands which touch at the six corners (the K and K′ points) of the hexagonal Brillouin zone [4,5]. Around these points, known as the Dirac points, the band structure forms a "Dirac cone" where charge carriers act as massless fermions with speed 1/300 that of light [6]. This accounts for extremely high carrier mobility at low excitation energies. Through what is known as the "zone-folding" approximation, the energy bands of a CNT can be derived by applying a periodic boundary condition to the band structure of graphene, perpendicular to the direction of the direction of the tube's length. The periodic "slices" taken from this band structure represent the band structure of the CNT [5], as shown in Figure 1. If one of these slices passes through the center of the Dirac cone, the resultant CNT will be metallic (Figure 1a). If the slices do not cross through this point, the resultant nanotube will be semiconducting (see Figure 1b). The zone folding approximation has limitations, as the curvature of a CNT causes deviations from the graphene band structure. This effect is greatest in CNTs with small diameters, and diminishes with increasing diameter [2,5].

Compared to single-wall CNTs, the properties of multi-walled nanotubes are less well defined due to the various possible combinations of chiralities and number of layers that may be present [5]. However, in computational studies of double-walled CNTs it was observed that even two concentric semiconducting tubes may behave as if they are metallic [7].

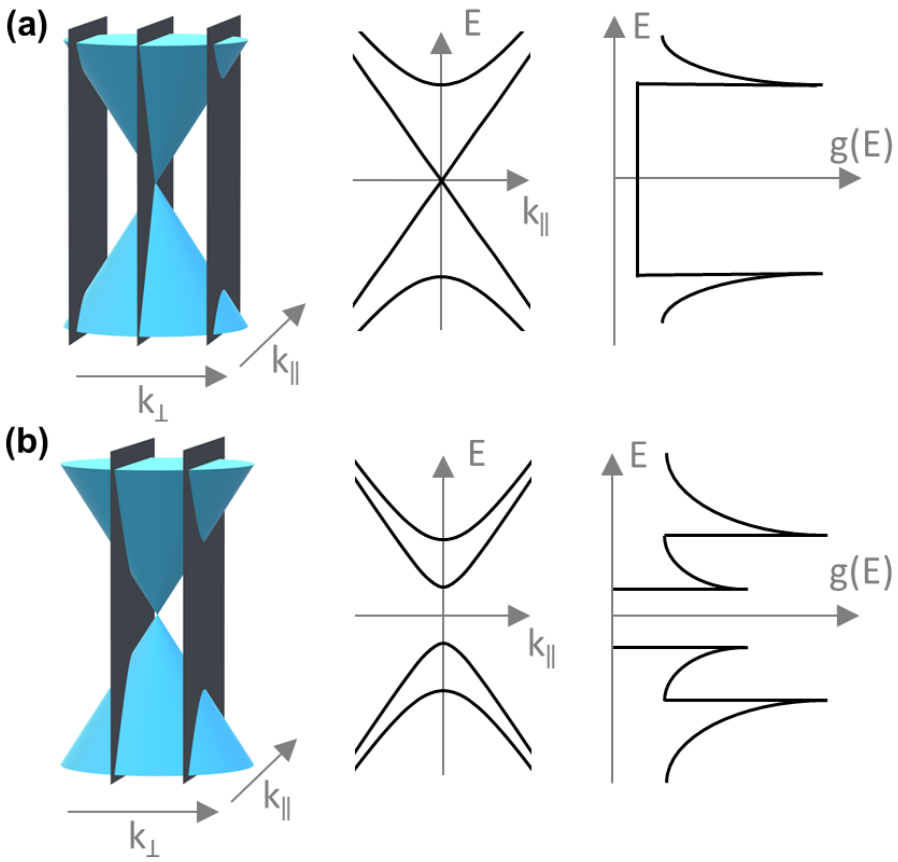

Figure 1: (a) A representation of the slices through the Dirac cone of a CNT as predicted by the zone-folding approximation, demonstrating the expected metallic band structure and resultant density of states. (b) A representation of the slices through the Dirac cone of a CNT as predicted by the zone-folding approximation, demonstrating the expected seminconducting band gap and resultant density of states.

Theoretically, the quantum confinement of the electrons within CNTs allows them to act as 1D ballistic conductors, i.e. conductors whose length is longer than the

mean free path (l_{mfp}) of their charge carriers [8]. The conductance (G) of such systems is governed by the Landauer equation for 1D systems:

$$G = \frac{2e^2}{h}\sum_i \Im_i(E_f) = G_0 \sum_i \Im_i(E_f)$$

where e is the elementary charge, h is the Planck constant, and $\Im_i(E_f)$ represents the transmission probability of the i^{th} subband state at the fermi level E_f [8]. The conductance quantum, G_0, represents the conductance of two degenerate electron states through a band when the transmission probability is 1. The above equation can also be written as:

$$G = G_0 MT$$

for an equivalent transmission probabilities $\Im_i(E_f) = T$ over *M* bands at the fermi level [9]. In single-wall CNTs, there are two conductance bands ($M = 2$). In the case of perfect transmission ($T = 1$), this results in an ideal ballistic resistance (R = 1/G) of 6545 Ω [9]. Practically, ballistic conduction has been observed in CNTs over distances of up to ~500 nm, with measured resistance of 6-7 kΩ in a single-wall CNT [10]. Beyond this, resistance tends to scale linearly at around 6 kΩ/μm [10], a result that has been experimentally demonstrated to near centimeter lengths [11]. This indicates in practice a mean free path in CNTs on the order of microns. Thus, a modified equation for the resistance of a single-wall CNT longer than l_{mfp} can be found as:

$$R = \frac{1}{2 * G_0}\left(\frac{L}{l_{mfp}}\right)$$

where L is the length of the CNT [9].

Studies into the conductance of individual multi-walled CNTs have proved more difficult. This is in part due to the innumerable combinations of chiralities that can exist for each of the shells of a multi-walled CNT. In addition, different production methods yield multi-walled CNTs with different internal structures [12,13]. Early studies into the conductance of individual multi-walled CNTs by Frank *et al.* produced the unexpected result of conductance values that were either odd integers or fractions of the quantum conductance [14]. In this study, multi-walled CNTs were attached to the gold tip of a scanning probe microscope using conductive silver paint. The microscope was used to lower the CNTs into a liquid metal bath acting as the second electrical contact. The authors suggested that conductance values that were fractions of the quantum conductance (i.e. 0.5 G_0) may be due to a taper in the tip of the multi-walled CNTs leading to elastic scattering and/or defects within the multi-wall CNTs, which short out when submerged below the surface of the liquid metal electrode to produce the more typical integer values of conductance. More generally, the lower than expected values of conductance were taken to indicate that only the surface layer of the multi-walled CNT contributed to the conductance [14]. An investigation of these results by Sanvito *et al.* through computational modelling demonstrated that the odd integer values of conductance could be caused by inter-wall interactions blocking certain conduction channels [12]. The authors also found that higher conductance was obtainable if the inner electrode shells were in contact with both electrodes [12].

1.1.1. Synthesis of Carbon Nanotubes

The “discovery” of CNTs may date back to as far as two centuries ago, though techniques capable of observing and characterizing them (such as electron microscopy)

had not yet been developed [15]. Early relevant studies include those by Radushkevich and Lukyanovich, who in 1952 demonstrated the production of nanoscale hollow cylinders of carbon [15]. In 1956, Roger Bacon proposed a rolled graphitic structure in his 1956 studies of the melting of graphite under an arc discharge [3]. However, it was a 1991 Nature article by Iijima demonstrating the production of multi-walled CNTs that sparked sustaining interest in this unique allotrope of carbon and its properties [1–3,15]. The production of single-wall CNTs soon followed, published in two independent 1993 articles by Bethune *et al*. and Iijima and Ichihashi [1,15].

The earliest process for the intentional production of CNTs are based on the arc-discharge method. In the arc discharge method, a low-voltage, high-current power supply is used to create an electrical arc between two graphite electrodes under an Ar or He atmosphere, as shown in Figure 2a. In Iijima's 1991 study, multi-walled CNTs were found to form on the cathode, along with soot and fullerene byproducts. The addition of iron (by Iijima) or cobalt (by Bethune) catalyst to the carbon anode produced the first single walled CNTs in a set of 1993 papers [3]. The arc discharge method allows for gram-level production of CNTs with high crystallinity and low defect density [2].

Larger scale, multi-gram production of single-wall CNTs was achieved through a laser ablation process pioneered by Smalley *et al*. in 1996 [2,3]. In this process, a laser pulse is used to ablate a carbon target containing catalyst particles (such as Ni/Co) placed within a furnace, as shown in Figure 2b. Carbon nanotubes grow from the vapor plume ejected from the target and are carried in an inert gas flow out of the furnace to collect on a cold finger [2].

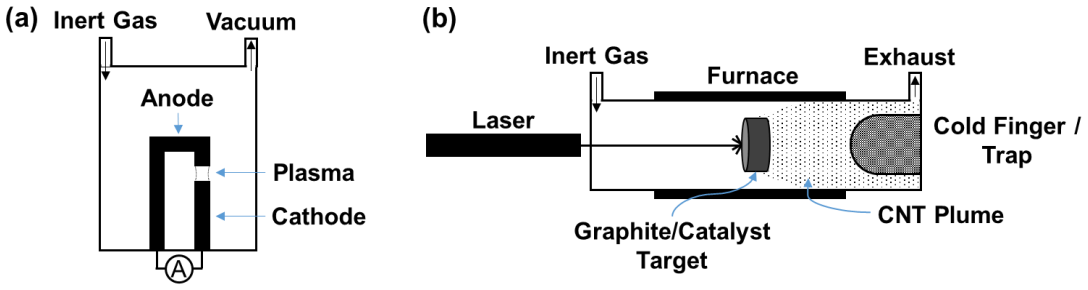

Figure 2. (a) An arc-discharge reactor for CNT synthesis.
(b) A laser vaporization system for CNT synthesis.

While both arc-discharge and laser vaporization techniques require high energy and temperature to produce CNTs, somewhat milder conditions are utilized in the chemical vapor deposition (CVD) techniques [16]. These techniques have been adapted towards the production of kilogram-scale amounts of CNTs, to the great benefit of commercialization efforts [3,16]. Generally, these techniques rely on the decomposition of a gaseous carbon-containing precursor (such as methane, acetylene, carbon monoxide, etc.) onto a catalytic metal nanoparticle surface. In these processes, the carbon precursor dissociates on the catalytic nanoparticle surface. Due to the limited solubility of carbon within the nanoparticle, precipitation of the carbon occurs from the surface of the particles forming a tubular structure [2]. In a basic configuration, catalyst particles are supported on a substrate, and tubes grow from these particles off of the surface [3]. The CVD technique allow for novel structures such as vertically aligned arrays of CNTs, and is adaptable to the production of both single-wall and multi-walled CNTs [16].

There are a few notable variants of CVD techniques. The first is known as the high-pressure carbon monoxide (HiPCO) method. This process utilizes a carbon monoxide carbon feedstock and iron carbonyl, nickel carbonyl, or ferrocene as the gaseous catalyst [3,16]. Both are injected into a furnace at 900-1100°C and 30-50 atm pressure. The catalyst particles are formed *in situ* from the decomposition of the injected

compounds [3]. Kilograms of small-diameter, high-quality (up to 97% pure) single-wall CNTs may be produced by this method [3,16]. Plasma-enhanced CVD (PECVD) techniques have also demonstrated great promise. These methods utilize a radio-frequency generated plasma to assist in the breakdown of precursor gasses [3,16]. In one implementation, the hydrocarbon precursor is broken down by a hot filament near the entrance of the reaction furnace. This allows for lower temperatures to be utilized at the deposition substrate, allowing for a wider variety of materials to be utilized as the substrate [3]. PECVD may also be adapted towards the selective growth of low diameter or preferentially semiconducting single-wall CNTs [16]. Finally, floating-catalyst CVD (FCCVD) methods, as shown in Figure 3, were developed in order to assist in the scaling of CVD production towards a continuous process [17,18]. In these methods, similar to the HiPCO method, a catalytic metal precursor (such as ferrocene) is injected into the CVD furnace with the carbon feedstock (typically a hydrocarbon or alcohol). As the carbon and metal precursors are both floating within the gas flow in the CVD furnace, no substrate is needed. The CNTs are produced as a loose aerogel which flows through the furnace. Fibers consisting of CNT may then be directly condensed and drawn or wound from the end of the furnace [17,18]. The unspun CNT fiber drawn from an FCCVD reactor is referred to as CNT roving in this text.

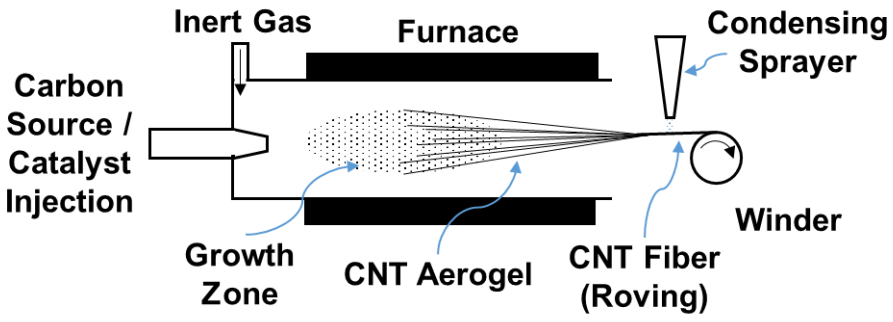

Figure 3. A floating catalyst CVD (FCCVD) reactor for CNT synthesis.

1.1.2. Production of Bulk Carbon Nanotube Wires

Carbon nanotubes (CNTs) exhibit great promise for electrical conductor applications due to a combination of high electrical conductivity [19], great flexure tolerance [20], high tensile strength [21], and an order of magnitude lower temperature coefficient of resistance relative to conventional wiring metals [22,23]. Individual carbon nanotubes have exhibited conductivities as high as 10^8 S/m [20,24], higher even than that of traditional metallic conductors such as copper (with a conductivity of 5.8×10^7 S/m) [25]. Estimates towards the maximum conductivity of bulk carbon nanotube structures range from 1.8×10^7 S/m for a fully dispersed network of metallic single-wall CNTs [26] to 5.6×10^{16} S/m for a km-length metallic monocrystalline CNT wire [24]. However, the junctions between individual carbon nanotubes [27] and bundles of CNTs [28], along with their alignment within the wire [29] presents a unique challenge in the translation of the electrical conductivity to bulk structures.

Carbon nanotubes preferentially align themselves into a hexagonally-packed bundles due to van der Waals forces between the tubes [1,30]. The bundling of CNTs may change their electronic density of states from that of individual tubes – for instance opening a pseudogap in bundles of armchair nanotubes [1,5]. Xu *et al*. have computationally investigated the effects of tube overlap on electron transport [31]. That group has suggested that large (essentially infinite length) overlap between carbon nanotubes may be preferable to shorter junctions to achieve high conductivity in CNT wires. The authors state that while there exist ideal overlap lengths to achieve a high probability of transmission between tubes, with large overlap between tubes only an

estimated ~0.04 eV potential may be required to transmit along the length of the entire wire [31].

A variety of strategies have been explored for the production of wires from CNT feedstock. One of the simplest methods is the rolling and densification of CNT sheet material. Nanotube purification from as-produced soot commonly involves a refluxing in acid to remove metallic and amorphous carbon impurities. The refluxed suspension is then commonly filtered to remove the acid and dissolved impurities, forming a freestanding carbon nanotube sheet called a “bucky paper” [32]. These sheets may be rolled into cylinders and pulled through drawing dies to form wires [20]. While this method is quite straightforward and adaptable to larger diameter wires, CNT bundles are typically isotropically aligned in plane in the sheets. The lack of axial CNT alignment in rolled wires means that the wires contain numerous junctions, limiting the conductivity that may be achieved.

An alternative is the “wet-spinning” method. In this method, CNTs are dissolved into a suitable solvent, such as pure sulfuric acid or chlorosulfonic acid [23,33]. A concentration of CNTs is typically chosen so that a liquid crystalline phase of CNTs is present in the solution [34,35]. The solution is loaded into a syringe, and the nanotubes are extruded from the syringe into a coagulant bath that is miscible with the CNT solvent, but does not form solutions with the CNTs. Thus, the CNTs precipitate and coagulate into a filamentous wire [30,34]. Wet processing techniques of this sort can produce high quality wires with a high degree of CNT alignment and limited crystalline-defect/void space [36,37].

The “dry-spinning” methods are another strategy for the production of CNT wires. The first dry-spinning method is process of “direct spinning” from a FCCVD reactor. In this process, the CNTs are collected by a metal rod as they leave the CVD reactor [17,30]. The “plume” of CNTs is then tensioned into a wire through e.g. rolling spindles [18,38] This tensioning pulls the tubes into alignment through their van der Waals interactions [30]. The second commonly utilized dry spinning method is the “forest spinning” technique. In this technique, a wire is pulled directly from a vertically-aligned CNT forest grown onto a substrate via CVD. Similar to the direct spinning technique, the van der Waals interactions between the CNTs pull the wire into alignment [30,39–41]. Dry processing methods are typically followed by a densification process to reduce the porosity of the wires and improve conductivity [30,42–44].

Whether inter-tube or inter-bundle resistance dominates the resistance of a CNT networks has been a matter of much discussion. Early results by Fuhrer *et al*. of a thick CNT mat assigned defects within a CNT bundle (i.e. inter-tube resistance) as the primary cause of charge localization [45]. Conversely, more recent results by Garrett *et al*. of single-wall CNT thin films found inter-bundle resistance to be 3-3.5X higher than inter-tube resistance. The authors attribute the difference in results to improvements in CNT production methods, as well as their thin film’s more sparse CNT network [28]. Work by Hecht *et al.* [10] also concludes that inter-bundle contacts dominated the resistance of their single-walled CNT network. They propose that longer length CNTs (up to 20-30 μm long) may close the gap between inter-tube and inter-bundle resistance. A more recent proposal by Dini *et al.* posits that the dominant resistance in thicker wires and fibers may be a factor of the wire production method [46]. CNTs that are grown as vertical arrays

naturally form closely packed bundles with their nearest neighbors. When wires are produced from the drawing or forest spinning of CNT arrays, the natural bundles may form discrete areas of conduction within the bulk structure. As a result, the inter-bundle resistance dominates in wires spun from CNT arrays. In wires produced from FCCVD or wet-spinning methods, the individualized CNTs form a more continuous structure with no specific bundle length. In this situation, the electrical transport preferentially takes place through metallic percolation networks, and thus inter-tube transport dominates [46]. Therefore, depending on the particular source and morphology of the CNT network, both types of resistance must be considered. Overall, longer CNTs and more tightly-packed crystalline bundles are generally proposed to produce the highest conductivity wires [10,22,28].

1.2. Metal-Carbon Nanotube Composites and Hybrids

Over the past few decades much research has been done toward improving the characteristics of bulk CNT conductors [20,30]. Some methods have focused on assembly of the bulk CNT materials, aiming to limit the amount of empty space and resistive junctions in as-produced wires [19,34,36]. Other post-processing techniques such as stretching [47], ionic doping [48–50], densifications [43,44,51], and heat treatments [52] have also been employed to lower the resistance within the micro- and nanostructure of a CNT wire. Such efforts have led to chemically doped CNT wires with conductivities between 10^6–10^7 S/m [36]. Alternatively, there are efforts focused on combining CNTs with traditional metallic conductors to produce hybrids which aim to combine the advantages of each material into one hybrid conductor [53–58].

Conventional metals such as copper offer high electrical conductivity (58 MS/m) around room temperature, but decline in operation at elevated temperatures from a high temperature coefficient of resistance (TCR) (3.83×10^{-3} K^{-1} with respect to 300 K) [25]. For example, the conductivity of copper decreases by a more than half from 300 K to 600 K. This high temperature coefficient is a results of electron-phonon scattering within the metallic crystal structure [59]. Conversely, bulk carbon nanotube (CNT) conductors offer a combination of a low TCR [22,29,60] and robust mechanical properties (i.e. high tensile strength, flexibility, and corrosion resistance) [20,30], but have an order of magnitude lower room temperature electrical conductivity compared to both common conductor metals like copper at 58 MS/m [25] and the theoretical limit for individual CNTs of >100 MS/m [24,61]. Thus, a hybrid material that is able to combine the high electrical conductivity of a metal like copper with the low TCR of CNTs promises to reduce ohmic energy losses, especially in higher temperature applications such as in transformers, generators, and motor stator windings [30].

To combine the high conductivity of metals and the low TCR of CNTs, the internal structure of a hybrid electrical conductor should consist of a relatively high quality, well dispersed CNTs that are ideally contacted with one another through metal interconnections [9,62]. Furthermore, the metal matrix should not perturb the ballistic conduction of the CNTs [9]. In this way, the ballistic conduction of the CNTs can be combined with the high quality bulk structure of a metal, as illustrated in Figure 4. Hjortstam *et al.* have suggested that ideal structures may be able to double the conductivity of copper though the incorporation of a minimum of 30-60 % SWNTs by

volume [9]. In the remaining sections of Chapter 1, a variety of techniques that have been investigated to produce metal-CNT hybrids will be discussed.

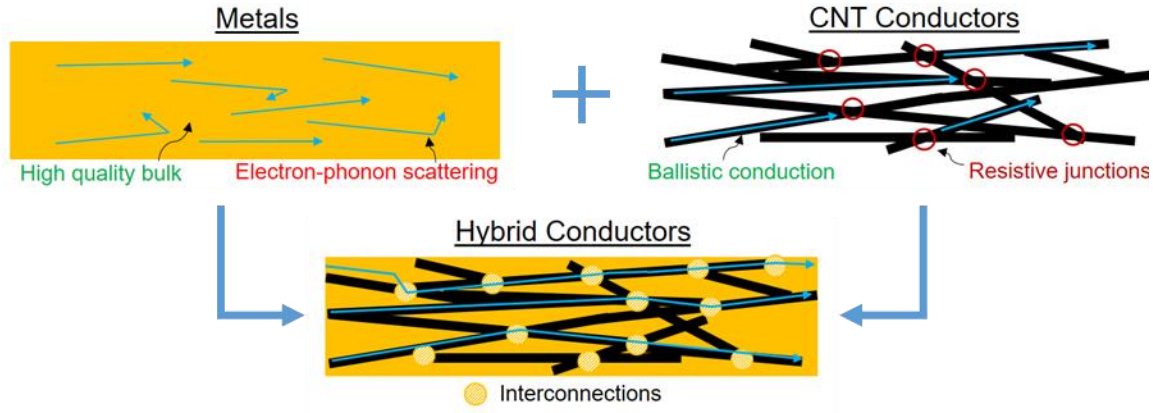

Figure 4. A scheme illustrating the goal of a combination of a metallic and CNT conductor to form a hybrid electrical conductor.

1.2.1. Electrodeposition

An early study into the combination of a macroscopic CNT conductor with metal was carried out by Randeniya *et al*. in 2010 [60]. In this study, a multi-walled CNT fiber produced through drawing from a vertically aligned CNT "forest" was used as the template for deposition. This attempt uses an electrochemically active sacrificial anode to plate metal onto the CNT cathode. Various metal deposition baths are proposed to deposit Cu, Au, Ag, Pt, Pd, and Ni onto the 13 μm diameter CNT conductor. The Ag deposition was noted to deposit dendritic crystallites onto the surface of the CNTs, while the Cu, Au, Pt, and Pd formed smoother deposits on the surface. Plated wire conductivities were seen to increase up to a wire diameter of 23 μm, after which the conductivities generally plateaued. High, metal-like conductivities were obtained from the Cu (~3×10^7 S/m) and Au (~2×10^7 S/m) plated CNTs. However, these were coupled with metal-like TCR values of 3.9×10^{-3} K^{-1} for Cu plated CNTs and 3.2×10^{-3} K^{-1} for Au plated CNTs over

the temperature range of ~0 to 300 K. The authors claim that this demonstrates the dominance of the metal in the composite's conduction. Conversely, the Pd and Pt depositions led to an order of magnitude lower conductivity (~2×10^4 S/m and ~5×10^3 S/m, respectively), but exhibited negative semiconductor-like TCR (similar to the starting CNT conductor).

A 2013 paper by Subramaniam *et al*. [53] demonstrated a two-step electrodeposition process to incorporate copper into carbon nanotubes. The first step consisted of an organic electrodeposition from a 2.75 mmol solution of copper acetate in acetonitrile, which "wets" the CNT and deposits a seed layer of copper uniformly throughout the CNT matrix. In this process, the CNTs are allowed to sit in the electroplating solution for 20 minutes prior to the electrodeposition. The CNTs are then applied to a stainless steel mesh backing, and then sandwiched between two strips of pure copper, which act as anodes. The CNTs are separated from the copper by a piece of Anodyne filter paper that acts as the separator. A slow deposition rate of 1-5 mA/cm^2 is used in the initial deposition to ensure that copper nucleation along the CNTs (rather than ion diffusion through the network) is the rate-limiting step. The CNT network was observed to achieve maximum filling of copper after 600 minutes at 5 mA/cm^2, beyond which the solution would begin to plate onto the surface. In the second step, the copper fraction was brought from ~40 vol% to ~55 vol% through the subsequent electroplating step in a commercially available aqueous electroplating solution. After each electrodeposition step, the copper was annealed at 250°C in a H_2 environment. From this process, a room-temperature electrical conductivity of $(4.7 \pm 0.3) \times 10^7$ S/m was obtained for a 2.5 × 3.5 cm coupon and a room-temperature electrical conductivity of

$(2.1 \pm 0.3) \times 10^7$ S/m was obtained for a linear microscopic conductor. A density of 5.2 g/cm^3 was measured for the composite, which equates to a specific conductivity of ~9000 S·m^2/kg for the coupon and ~4000 S·m^2/kg for the microscopic conductor. In addition, a TCR of 7.5×10^{-4} K^{-1} was evaluated for the conductor.

The two-step deposition practice was adapted to bulk scale wires by Sundaram *et al.* in 2017 [56]. In that work, a commercially available multi-walled CNT single filament wire from Muratec with a diameter of 40 μm was used as the CNT template. A similar electroplating and annealing setup to the Subramaniam work was employed [53]. A current of 2.5 mA/cm^2 was utilized for seeding, and 10 mA/cm^2 was utilized for filling. In this study, the impact of the copper filling was evaluated on the wires. The starting conductivity of the MWCNT conductor was $(9.09 \pm 0.83) \times 10^4$ S·m^2/kg. A wire with aqueous copper overcoating only ("core-sheath", 84-88 wt% Cu) exhibited a conductivity of $(3.03 \pm 0.25) \times 10^6$ S/m. With Cu seeding alone (90-94 wt% Cu) from the organic deposition, the composite exhibited a conductivity of $(1.33 \pm 0.18) \times 10^6$ S/m. A "partially-filled" composite (95-97 wt% Cu) exhibited a conductivity of $(3.23 \pm 0.34) \times 10^6$ S/m. Finally, a fully filled composite (96-98 wt% Cu) exhibited a conductivity of $(6.25 \pm 0.63) \times 10^6$ S/m. Density was observed to increase with increasing copper filling: 0.55 g/cm^3 from the MWCNT conductor, 1.6 g/cm^3 in the core-sheath configuration, 3.2 g/cm^3 in the Cu seeded conductor, 3.4 g/cm^3 in the partially filled conductor, and 5.2 g/cm^3 in the fully filled conductor. TCR was also seen to vary with the degree of filling. The core-sheath structure exhibited the highest TCR at $(3.0 \pm 0.4) \times 10^{-3}$ K^{-1}. With Cu seeding alone, a TCR of $(-4.0 \pm 0.6) \times 10^{-4}$ K^{-1} was obtained. Upon partial filling, a substantially higher TCR of $(2.8 \pm 0.4) \times 10^{-3}$ K^{-1} of was obtained. This dropped to (1.7 ±

0.2) × 10^{-3} K^{-1} with full filling. Thus, full filling appears to mitigate the effects of increasing TCR brought on by the higher Cu wt%. An important consideration of this work [56] as well as a subsequent paper [63] is that a 24 hr or greater time is required to fully seed the CNT fiber template with Cu seeds.

An aqueous copper sulfate electrolyte consisting of 200 g/L $CuSO_4$ and 40 g/l H_2SO_4 was utilized by Hannula *et al*. to electrodeposit copper both on the interior and exterior of a CNT fiber [64]. The CNT fibers varied between 5-30 μm in diameter and were produced through a CVD method. The average conductivity of the starting fiber was measured as 3 × 10^4 S/m with an estimated density of ~0.7 g/cm^3. A bath-type electrodeposition setup was utilized in this paper, with the CNT fiber suspended within a nonconductive frame in the electroplating bath. This initial work demonstrated that the specific conductivity of the Cu-CNT hybrid was seen to drop from 98.3% of pure copper's value at 0.25 wt% CNT (99.75 wt% Cu) to ~50% of pure copper's value at 5 wt% CNT (95 wt% Cu). Latter work by Hannula *et al*. investigated the use of anodization [65] and ionic doping through submersion in a Watts bath (used to deposit Ni) or boric acid for up to 72 hrs [66] to produce higher conductivity wires. In the latter study [66], a specific conductivity 87% of copper's was obtained from an 95.3 wt% Cu/4.7 wt% CNT yarn with a diameter of 150-200 μm. The authors attribute this increase in specific conductivity to a higher degree of surface plating compared to internal deposition [66].

Xu *et al*. explored an anodization pretreatment method for the continuous electrodeposition of Cu onto CNT fibers. In their continuous setup, a CNT fiber was pulled from a vertically aligned CNT forest produced through chemical vapor deposition.

The fiber is pulled through an anodization bath of 10 wt% solution of H_2SO_4, where it is exposed to an anodic potential of 2.6V. After ~49 seconds of anodization, the fiber is then pulled through an aqueous plating bath of 160 g/L $CuSO_4$, 12 ml/L H_2SO_4, and 1 mL/L octylphenyl poly-(ethylene glycol) ether for times ranging from 11-56 s. From a 1 μm thick Cu coating onto the 16-23 μm diameter anodized fiber, the conductivity rose from 4.16×10^4 S/m to 4.08×10^6 S/m. This conductivity is ~4X higher than a similarly coated fiber that has not undergone anodization. With a 3 μm thick copper coating, the conductivity of the anodized fiber rose to 1.84×10^7 S/m. However, as the thickness of the copper coating increases beyond 3 μm, the conductivity differences between the anodized and non-anodized fibers begin to decrease due to the dominating effect of the copper overcoat on the conductivity.

Zou *et al.* compare oxidative anodization and aqueous nickel depositions pretreatment processes for the production of electrodeposited core-shell Cu-CNT conductors (coated by aqueous electrodeposition of copper) [55]. In their process, multi-walled CNT fibers were produced by pulling a fiber from a vertically aligned forest of CNTs on a silicon wafer. The initial fiber exhibited a conductivity of 4.3×10^4 S/m to 5.2×10^4 S/m with a diameter of 15 μm. The nickel buffer layer was deposited form a solution of 120 g/L $NiCl_2$ and 200 mL/L HCl. For comparison, an oxide buffer layer was produced through anodization at 3V in a 10% H_2SO_4 solution. After the buffer layer was deposited, copper was deposited from a solution of 160 g/L $CuSO_4$ and 12 mL/L H_2SO_4. The deposition time for the nickel and copper layers was 25s. All of the fibers were annealed at 300°C for 30 minutes after the depositions. The final densities of the annealed fibers were 3.61 g/cm^3 for the CNT-oxide-Cu fiber (CNT-O-Cu) and 3.83 g/cm^3 for the

CNT-Ni-Cu fiber. The diameter of the finished fibers was ~19 μm after the deposition of the ~2 μm thick copper layer. Conductivities of $(1.26 \pm 0.06) \times 10^7$ S/m for the CNT-O-Cu and $(2.03 \pm 0.05) \times 10^7$ S/m for the CNT-Ni-Cu fiber were obtained. In addition, the CNT-Ni-CNT fiber exhibited a TCR of 1.14×10^{-3} K^{-1} over the range of 300 K to 500 K with improved bending tolerance and flexibility compared to the CNT-Cu and CNT-O-Cu fibers. This electrodeposition study indicates that buffer layers of a suitable metal may lead to both improved electrical and physical properties of a finished CNT fiber.

Another type of strategy that has been evaluated for the production of Cu-CNT composites are the so-called co-deposition methods. These methods use a plating solution containing dispersed CNTs that become incorporated into the deposition. In a typical example, Arai *et al*. used a variety of methods to disperse single-wall CNTs into an electroless plating bath [67]. Magnetic stirring was found to leave bundles of carbon nanotubes with average sizes greater than 100 μm. Ultrasonic homogenization was able to disperse the CNTs into bundles with sizes between 10-100 μm. Finally, mechanical atomization was able to disperse tubes into much smaller 10-100 nm bundles. The dispersed tubes were mixed at a concentration of 0.2 g/L into a $CuSO_4$ based electroless plating bath. A copper foil was sensitized by $SnCl_2$ and then plated with palladium seeds from $PdCl_2$ to prepare the cathode for electroless plating. The plated electrode exhibited the presence of CNTs throughout the uniform deposited composite film after a 120 minute deposition from the solution prepared from the mechanical atomization method. A similar study was carried out by Zheng *et al*. demonstrating the active electrochemical co-deposition of copper and carboxylate-functionalized CNTs [68]. In that work 0.42 wt% of the composite was evaluated to be CNTs. However, as mentioned in a work by

Sundaram *et al*. [62] both of these co-deposition methods have a disadvantage in that the concentration of CNTs within the deposition solution is limited and the directionality of the CNTs in the finished composite is arbitrary, neither of which is necessarily ideal for a Cu-CNT hybrid wire.

1.2.2. Physical Vapor Deposition

Han *et al.* evaluated magneton sputtering, a form of physical vapor deposition, to produce Cu-CNT composites [58]. Like most physical vapor deposition methods, magnetron sputtering is limited to line-of-site deposition of metals onto a surface [69], creating a layered Cu-CNT composite rather than a fully integrated hybrid. This work utilized a CNT fiber produced from a floating catalyst chemical vapor deposition (FCCVD) process [58]. The deposition time was used to control the thickness of the copper layer from the magnetron sputtering process. Times of 0.5, 1.0, 1.5, and 2.0 hr were investigated, leading to deposited copper thicknesses of 5 ± 1 μm, 10 ± 4 μm, 15 ± 3 μm, and 20 ± 3 μm respectively. These equate to 62.0%, 78.5%, 82.5%, and 86.5% Cu, respectively, by weight. From this process, with an initial CNT fiber conductivity of $(4.46 \pm 1.3) \times 10^5$ S/m, conductivities from $(1.37 \pm 0.10) \times 10^7$ S/m (for 0.5 hr deposition) to $(2.36 \pm 0.10) \times 10^7$ S/m (for 2.0 hr deposition) were obtained. The 0.5 hr deposited Cu-CNT composites was drawn through radial dies decreasing from 140 μm diameter to 100 μm diameter, which led to a final conductor diameter of 100 ± 2 μm. The density of the fiber increased from 1.71 ± 0.23 g/cm^3 to 2.66 ± 0.33 g/cm^3. This also led to a corresponding increase in conductivity to $(1.56 \pm 0.11) \times 10^7$ S/m. In a subsequent paper, it was found that the densification process allowed for the compression and removal of void space from the underlying CNT fiber,

without damaging the fiber [70]. In a further follow-up paper [71], the researchers pushed the densification of the Cu-CNT fiber further through planar densification in a rolling mill. A composite with 71.3 wt% Cu was densified from 1.72 g/cm^3 to 4.61 g/cm^3. With the increased densification, the conductivity was measured to increase from $(8.6 \pm 0.6) \times 10^6$ S/m to $(2.6 \pm 0.3) \times 10^7$ S/m.

1.2.3. Powder Processing

In contrast to the solvated metal ions of electroplating and the metal vapors of PVD, powder processing methods are those in which the metal precursor remains in the solid phase during the mixing process with the CNTs. This category of technique is particularly prevalent in the field of metal matrix composites (MMCs), where enhanced mechanical attributes are typically the major goal [72].

A straightforward method of powder processing was explored by Lekawa-Raus *et al*. to deposit silver nanoparticles within a CNT network [73]. In this work, a commercially available silver nanoparticles suspension within an organic, low viscosity solvent mixture was dropped onto the carbon nanotube fiber. Nanoparticle of silver were seen to adhere about and around the bundles of the CNTs. With sequential exposures to the solution the conductivity of the wires was seen to rise by as much as ~7× the CNT fiber's original conductivity after 8 exposures. However, the specific conductivity of the fiber was seen to decrease by as much as ~4× due to the increased mass from the nanoparticles. This paper demonstrates perhaps the simplest form of incorporation of metals via powder processing into CNT fibers.

An alternative powder processing method that has demonstrated success in metal-CNT composite formation is the "molecular-level mixing" strategy. In this method, as demonstrated by Cha *et al*. [74], the CNTs to be incorporated are first functionalized to improve their interaction with the metal. In the process described, CNTs produced by thermal CVD were first soaked in HF for 24 hr. Then they were transferred to a 3:1 mixture of H_2SO_4/HNO_3. This acid treatment serves to functionalize the CNTs with amide and carboxylate functionalities. After suspending 20 mg of the functionalized CNTs in 500 mL ethanol via sonication, 3 g of copper acetate was added to the suspension. The functionalization allows the copper ions to interact and bond to the surface of the CNTs in this suspension. Then the solvent is evaporated, and the particles are oxidized at 300°C in air to remove functional groups from the composite powder. This powder consists of embedded CNTs within a CuO matrix. Next, the powder is reduced to CNT/Cu via exposure to H_2 gas at 250°C. Some oxide functionalities remain to link the CNTs to the copper phase after this process. Finally, this CNT/Cu powder may be sintered (by spark plasma sintering) into a bulk nanocomposite cylinder. Composites consisting of both 1.0 wt% and 2.2 wt% CNTs were produced. While this initial study focused on the improved mechanical properties of the composite (i.e. a 20.3× increase in yield strength), later studies would delve into the electrical characterization.

Arnaud *et al*. utilized a similar molecular mixing and freeze drying technique to produce Cu-CNT composite wires [75]. Double-walled carbon nanotubes were soaked in a solution of HNO_3 and H_2SO_4 to form a suspension. HCl was added to this suspension, and the mixture was neutralized with aqueous ammonia. From this, a 1.1 g/L suspension of acid functionalized CNTs was produced. Under ultrasonic agitation, an aqueous

solution of Cu powder was then added to the suspension. The mixture was frozen using liquid N_2, and then freeze dried. The dried powder was then heated to 214°C, under H_2 for 1 hr to reduce copper oxides to metallic copper. The CNT/Cu powder was then spark plasma sintered at 700°C into an 8 mm × 33 mm cylinder. The cylinder was drawn through conical tungsten carbide dies in order to produce wires with 0.5 vol% CNTs. These wires were seen to have 10% improvement in ultimate tensile strength compared to pure Cu, but with the tradeoff of ~11% lower conductivity. In a later study by the same group [76], two different size Cu powders were incorporated into the Cu-CNT composite wire to produce a bimodal grain size distribution. A further 20% increase in ultimate tensile strength over the previous study was measured in the Cu-CNT composite with a bimodal grain size distribution, with slightly less decrease in conductivity than the unimodal grain size distribution Cu-CNT composite wires.

The idea of interfacial adhesion layers for Cu-CNT composites has also been investigated through powder processing techniques. Cho *et al*. investigated the use of a chromium carbide (Cr_7C_3) interfacial layer to boost the interaction between the Cu and CNT phases in a hybrid [77]. The group utilized multi-walled CNTs synthesized via CVD and annealed to 2600°C. The CNTs were suspended in a solution of 3:1 H_2SO_4 and HNO_3 and ultrasonicated for 24 hr to disperse the tubes. It was noted in a previous work that the CNTs exhibit an amorphous carbon defect layer on their surface after processing [78]. After drying the CNTs, the CNTs were mixed with a CuCr solid solution powder (5 μm dia., 0.085 at.% Cr) in ethanol [77]. Thorough mixing of CuCr and CNTs was observed up to 5 vol% CNTs after spark plasma sintering of the powder mixture. Due to the compression of the sintering process, the CNTs were observed to align themselves in

a two dimensional plane normal to the axis of compression. It was observed that, during sintering, the Cr phase of the solid solution migrates to the amorphous carbon layer coating the CNTs, producing Cr_7C_3 at the interface. With increasing CNT concentration, the TCR lowered from 2.4987×10^{-3} K^{-1} at 1 vol% CNT to 1.6083×10^{-3} K^{-1} at 3 vol% CNT to 1.4511×10^{-3} K^{-1} at 5 vol% CNT. Consequently, the conductivity also decreased from 5.740×10^7 S/m at 1 vol% CNT to 5.514×10^7 S/m at 3 vol% CNT to 5.491×10^7 S/m at 5 vol% CNT.

1.2.4. Chemical Vapor Deposition

While there have been a number of studies in the production of metal-CNT hybrid electrical conductors through techniques such as electroplating [53,55,56,60,66,79], powder processing [73,75–77], and physical vapor deposition [58,70,71,80], there have been few attempts to produce hybrid conductors through chemical vapor deposition (CVD). In one of the limited studies that investigated CVD, CNTs are grown onto a metal surface (such as aluminum) that has been prepared by the deposition of a catalytic nickel layer [72]. However, in these studies, the CNTs are primarily used as a mechanical reinforcement for the metal phase [72], rather than a conductor in their own right. Thus, compared to the previously mentioned techniques [62], the use of CVD towards the production of metal-CNT hybrid conductors remains a novel area for exploration.

In nanoscale studies, it has been demonstrated that the Joule heating of junctions between individual carbon nanotubes may be used to drive the deposition of metal from a gaseous organometallic precursor in a process called “nanosoldering” [81]. The deposited metal bridges the CNT junctions, improving the electrical conductivity of the network.

Applications of this principle towards bulk CNT wires have yet to be explored. Ideally, by preferentially depositing metal at the higher temperature junctions within a bulk CNT conductor, the amount of surplus non-contributing metal can be limited, thereby improving the utilization of metal mass and volume within the conductor.

Using Joule heating driven CVD presents novel alternative compared to the other techniques described in this chapter for the production of bulk metal-CNT hybrid conductors. Modification of the applied current used to heat the CNT substrate conductor allows depositions to be specifically targeted towards hotter regions in the conductor, which can naturally exist near areas of high resistance. Furthermore, the use of a penetrating vapor allows for the deposition of metal throughout the volume of the CNT substrate conductor, in contrast to physical vapor deposition and certain demonstrations of aqueous electroplating. Thus, the potential exists for nanometal depositions that are able to bridge areas of high resistance and form interconnections both between discrete bundles of CNTs and between CNTs and metal overcoats, thereby enabling enhanced electrical transport throughout the composite. Additionally, Joule heating driven CVD processing can be carried out within the period of an hour or less, a substantial improvement over the up to 24 hour period that metal seeding via electroplating in an organic solution may take [82]. The nanometal deposits formed during CVD processing may then act as nucleation sites or "seeds" for subsequent overcoating. Compared to PVD, CVD allows for the penetration of vapor into the interior of the CNT network, allowing for better integration of the metal and CNT portions of the hybrid. Compared to powder processing techniques, CVD does not require the time and energy intensive dispersion of CNTs to create a composite. Higher volume fractions of CNT may be

utilized, and the CNT fraction may be anisotropically aligned to axis of the wire. Generally, CVD is adaptable to a wide variety of precursors and processing conditions, allowing for ultimate flexibility in both the CNT and metallic fractions of the conductor. Combined with conventional electroplating, CVD presents an efficient and scalable method towards the production of high conductivity hybrids.

1.2.5. Summary of Previous Techniques

Recent efforts to produce metal-CNT hybrid wires have typically focused on electrodeposition [53–56] or physical vapor deposition [57,58,83] methods. While high-quality coatings can be produced through either of these methods, they share a disadvantage in that the depositions are not intentionally site-specific. Instead, the deposited metal results at all locations across the CNT surface and/or within the CNT network. Furthermore, penetrating techniques such as organic electroplating can often take a full 24 hours to deposit an appropriate amount of copper seeds for further processing (e.g. through aqueous electrodeposition) [82]. In addition, some studies [56,58] have observed that, in certain configurations, layered structures of copper deposited onto CNTs produce higher conductivity than structures with partially intermixed copper and CNTs. In such studies [56] the partial intermixing of copper and CNTs leads to a large number of discretized copper islands that provide negligible contributions to the conductivity of the resultant wire, resulting in wasted mass. Powder processing techniques demonstrated a notable high conductivity and low TCR, but with highly limited CNT fractions and densities similar to those of the bulk metal [62]. Furthermore, there have not been many efforts to produce wires from sintered cylinders, so it is unclear how the composite would handle mechanical processing. Alternatively, if

a method such as CVD could quickly and effectively deposit metal throughout a CNT network, specifically targeting areas of higher resistance, it could greatly improve the utilization of deposited metal mass by allowing for the presence of additional copper where it is needed. Metal-seeded conductors produced by CVD could then be processed through fast and inexpensive techniques such as conventional aqueous electroplating to produce finished conductors, as shown in Figure 5.

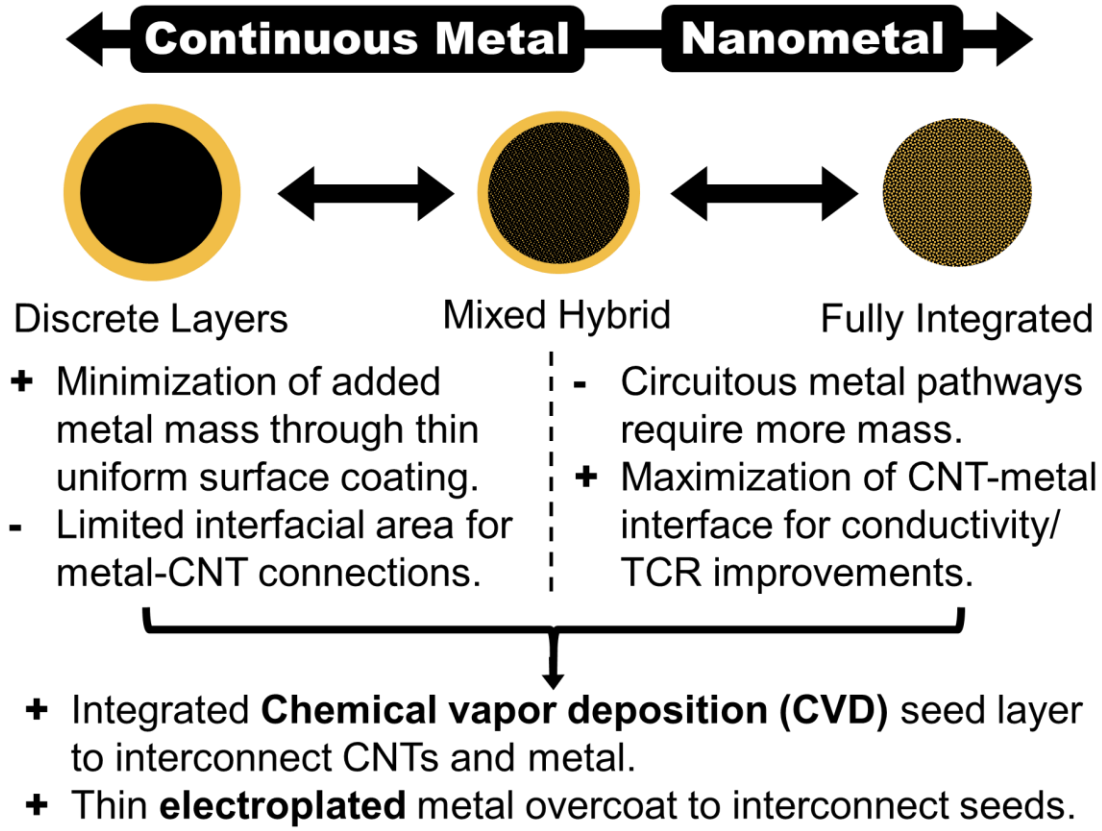

Figure 5: A combined approach towards the production of integrated metal-CNT hybrid conductors through CVD and electroplating.

CHAPTER 2: DISSERTATION OVERVIEW AND METRICS

2.1. Summary of Dissertation Goals

The goal of this dissertation is to develop the technique of site-selective Joule heating driven CVD in concert with subsequent electroplating towards the production of Cu-CNT hybrids with high electrical conductivity and improved high temperature performance compared to traditional metals. A fundamental characterization of how various CVD parameters impact the deposited seed metal mass and morphology is key to the development of Cu-CNT hybrids and composites. Therefore, a systematic study of CVD parameters will be carried out. Microscopy, physical, electrical, and mechanical measurements of seeded and electroplated conductors will be utilized to understand the impact of processing steps and experimental on the characteristics of the hybrid conductor.

This dissertation is subdivided into four main areas of research:

1. Development and demonstration of a Joule heating driven CVD method for the deposition of nanoscale seeding particles throughout a CNT network.
2. Investigation of the CVD reaction conditions in order to provide experimental control over deposited metal mass loadings and particle morphology.
3. Identification of appropriate precursors/metals to act as an interface between individual CNTs, bundles of CNTs, and metal overcoating with characterization of the metal-CNT interactions.
4. Optimization of the deposited CVD nanometal seeds and electroplated metal overcoating to produce integrated metal-CNT hybrid electrical conductors.

The remainder of Chapter 2 is devoted to the discussion of the metrics and techniques used for characterization of the samples. Chapter 3 deals with the initial qualification of the Joule heating driven CVD technique to deposit nanometal seeds. The chapter also discusses the ability to tune the CVD technique to produce depositions that are site-specific or uniform over the CNT roving template conductor. Chapter 4 is a systematic investigation of the effects of CVD conditions on the mass and morphology of deposited nanometal particles. Chapter 5 contains a survey of various precursors and metals used to produce seeds, with microscopic and electrical characterization of the depositions. Finally, Chapter 6 focusses on the optimization of platinum nanometal seed depositions to produce Cu-CNT hybrids with electrical conductivity comparable to metals. The impact of the areas of research is further expanded upon at the beginning of each of the respective chapters.

2.2. Metrics and Techniques

2.2.1. Conductivity and Specific Conductivity

As the primary goal of this work is to produce carbon nanotube based conductors that can compete with traditional metallic conductors, the electrical conductivity and specific conductivity of the material are of utmost importance. Measures of conductivity (σ) require knowledge of the resistance (R) of a material over a given length (L) and the materials cross sectional area (A) as:

$$\sigma = \frac{L}{R * A}$$

Measures of resistance per length (R/L) can be evaluated through four point probe measurements, with the advantage that the lead and contact resistance of the current supplying probes can be eliminated. In this setup, current is passed through the outer probes, while the inner probes measure the potential.

The cross sectional area can be determined in a number of ways. For a conventional cylindrical conductor, measurements of the wire's diameter may be used to determine the cross sectional area non-destructively. However, for an irregularly-shaped conductor, cuts must be made to evaluate the cross-section along the conductor's length. While these cuts may be made by slicing the conductor with a razor blade, this may cause deformation of the cross-sectional area. Thus, techniques such as laser cutting, microtoming, or focused ion beam milling may be employed to produce an accurate cross-section.

A simpler metric for irregularly shaped conductors is the specific conductivity (σ_{sp}). This value is equal to the conductivity (σ) normalized to the density (D) of the material:

$$\sigma_{sp} = \frac{\sigma}{D} = \frac{\frac{L}{RA}}{\frac{M}{LA}} = \frac{L^2}{RM}$$

The specific conductivity eliminates the need for knowledge of the cross sectional area (A), simplifying the equation to the product of the inverse of the resistance per length (R/L) and the inverse of the linear density (M/L). The specific conductivity is therefore normalized to the mass of the conductor rather than its cross-sectional area. This value can be obtained through a combination of four-point resistance measurements and measurement of the conductor mass using a microbalance.

For conductivity and specific conductivity measurements a Mettler Toledo XP-2U microbalance is used to measure sample mass. Sample lengths are determined using Marathon CO030150 high precision digital calipers. Electrical resistance was measured through a room temperature current-voltage (IV) sweep up to 50 mA for CVD seeded samples or 100 mA for electroplated and finished conductors in a four-point probe configuration with a National Instruments NI PXI-4110 programmable power supply and PXI-4072 digital multimeter.

Electrical characterization at different temperatures is also be critical to understanding of the impact of the metal fraction of the hybrid on the temperature coefficient of resistance. As heating up the sample may cause the oxidation or degradation of the metal fraction, passivation techniques may be required. Alternatively, the use of an inert environment, such as vacuum or Ar gas, may be utilized. Temperature dependent resistance measurements are be carried out in vacuum from 80 K – 700 K using a Janis cryostat connected to a National Instruments NI PXI-4110 Programmable Power Supply and an NI PXI-4072 digital multimeter. At least two temperature cycles are measured for each sample and the data presented is from the second cycle which eliminates the effects of high temperature annealing and atmospheric doping [84,85] from the measurements. Metallic samples typically have a linear relationship between the change in temperature and the relative resistance. Thus, the temperature coefficient of resistance (TCR) a_x for a given reference temperature T_x may be found from the relationship [25]:

$$a_x = \frac{R - R_x}{R_x * (T - T_x)}$$

where R_x is the resistance at T_x. In such cases, the TCR can be determined from the average slope of the resistance relative to a reference value with respect to temperature. For samples with nonlinear behavior, the temperature coefficient may vary in a nonlinear manner, and thus the equation:

$$a_x = \frac{1}{R_x} * \frac{\delta R}{\delta T}$$

may be more appropriate. This latter equation, however, limits the predictive usefulness of a_x.

Other equations have been developed to model the resistance of CNT networks based on theories of variable range hopping and/or phonon assisted tunneling conduction mechanisms [86–89]. One such model, proposed by Kaiser *et al.*, uses the following equation to fit the temperature dependent conductivity $\sigma(T)$ of a CNT network [89]:

$$\sigma(T) = \left[A\ exp\left(-\frac{T_m}{T}\right) + B\ exp\left(\frac{T_b}{T_s + T}\right)\right]^{-1} + H\ exp\left[-\left(\frac{T_0}{T}\right)^{\gamma}\right]$$

This model has three main components, prefaced by the scaling factors A, B, and H. The first term models pseudo-1D metallic conduction:

$$A\ exp\left(-\frac{T_m}{T}\right)$$

with resistance caused by metallic backscattering of charge carriers by zone-boundary phonons in the carbon nanotubes [89]. The factor T_m can be multiplied by Boltzmann's constant (k_B) to find the energy of zone boundary phonons for the CNTs. The value of this energy has been estimated to fall in the range of 1000-1500 cm^{-1} [90] for single-wall carbon nanotubes. This corresponds to temperatures between 1439-2158 K. The second term:

$$B\ exp\left(\frac{T_b}{T_s + T}\right)$$

models the phenomenon known as fluctuation assisted (or induced) tunneling (FAT). This term is related to electron transfer between large conducting segments separated by small barriers within a disordered material [91]. The magnitude of the barriers for electron transfer is related to $k_B T_b$. The factor T_b is related to the onset temperature of FAT and governs the low to room temperature conductivity of a sample. The factor T_s relates to retention of the conductivity near absolute zero, and is typically reported as a proportion of T_b. Finally, the third component of the equation:

$$H\ exp\left[-\left(\frac{T_0}{T}\right)^{\gamma}\right]$$

models conduction through variable range hopping (VRH) – tunneling between localized states through the absorption of phonons. The factor γ is related to the dimensionality of the hopping and T_0 is related to the localization length of the hopping. VRH relates to hopping between conductive regions that are more separated than those modelled by FAT [86,89]. Thus, the VRH term is less significant in thicker networks with larger conductive regions [48].

A second model proposed by Lekawa-Raus *et al*. [23] utilizes a similar pseudo-1D metallic term to model resistance at high temperature coupled with a Landauer ballistic conduction based formula to model resistance at lower temperatures:

$$R(T) = \beta * exp\left(-\frac{\delta}{T}\right) + R_{T_0}\left[exp\left(-\frac{T_A}{T}\right) + \left[1 - exp\left(-\frac{T_A}{T}\right)\right] * exp\left(-\frac{|T - T_0|}{T_C}\right)\right]^{-1}$$

Here, β and δ are analogous to A and T_m from the pseudo-1D metallic term of the Kaiser model. The values $R_{T_0}$and T_0 are respectively the minimum resistance and the

temperature at which it occurs. Similar to T_b from the Kaiser model, T_A represents the activation energy for hopping between ballistically conducting regions. Finally, T_C represents the "correlation energy" [23] which describe the shape of the curve at low temperature (similar to T_S in the Kaiser equation). Both the Kaiser and Lekawa-Raus models are useful for understanding the physical nature of temperature-dependent resistance behavior observed in FCCVD produced CNT conductors [46].

2.2.2. Microscopy

A firm understanding of the measured electrical properties will require a thorough evaluation of the physical and chemical characteristics that allow the properties to manifest. Sample surface morphology may be evaluated through techniques such as optical and electron microscopy. Since the conductors are macroscopic, optical microscopy is a versatile technique for evaluating conductor size, shape, and the macro- to micro-scale distribution of deposited compounds. For cylindrical conductors, optical microscopy can be used to efficiently gather a large number of diameter measurements for determination of conductivity and density.

Scanning electron microscopy (SEM) can be used to further delve into the micro and nanoscale morphology of depositions. Secondary electron (SE) images portray the surface topography of the analyzed samples. This provides insight into the size and distribution of deposited particles. Backscatter electron imaging (BSE) enables contrast based on the atomic number (Z) of the imaging region. Metal nanoparticles will show up much more brightly on the CNT surface in BSE imaging. This will allow for ease of particle counting and measurement. Many SEMs are equipped with energy dispersive x-

ray spectroscopy (EDS) as a peripheral tool for atomic characterization. This technique observes the characteristic x-rays emitted from relaxation to lower energy states after excitation or ejection of an electron by the incident electron beam [92]. EDS may be utilized to evaluate the distribution of CNTs and deposited metals within a hybrid conductor (especially when combined with cross-sectional imaging).

Through vertical mounting of samples, SEM allows for the accurate measurement of cross-sectional area. There are three main methods that may be utilized to produce an accurate cross-section from a given conductor. The first is sectioning with a razor blade. This technique is valuable in its simplicity but may cause some dislocation of CNTs due to compressive forces. It will find the most utility in the sectioning rigid samples, such as composites and hybrids with heavy surfaces coatings, which are less likely to distort due to such compressive forces A second option for cross-sectioning is to mount the sample in epoxy resin, and then use polishing and/or microtoming to expose a cross-sectional area. This technique is more labor intensive than sectioning with a razor blade but may be completed using local resources. A conductive carbon coating may need to be applied via sputtering to avoid charging. A final option is focused ion beam (FIB) milling. This technique requires the use of an SEM equipped with a FIB/LMIS (Liquid metal ion source) tool. This technique has the advantage of observing the cross section *in situ* following milling. However, the technique is time intensive and more expensive.

2.2.3. Mechanical Characteristics

While the primary focus of this dissertation is related to the electrical properties of the metal-CNT hybrid conductor, mechanical characteristics are still an informative consideration. Ideally, such hybrids would mimic the more desirable characteristics of

each component, although studies of MMCs have shown that there are frequently trade-offs when combining these materials [72]. Tensile testing of the material is a reliable way to extract mechanical properties of a sample. Tensile testing may be carried out in a TA Q800 DMA with a maximum applied force of 18 N and a resolution of 10 μN, or an Instron 5944 Mechanical Analyzer with a load cell maximum of 2 kN and a resolution of 1 μN. This equipment allows for engineering stress-strain measurement of a large variety of sample geometries. The ultimate tensile strength σ_{UTS} of a sample is defined as the maximum amount of stress that can be measured from an engineering stress-stain plot, where the stress is defined as:

$$\sigma = \frac{F}{A}$$

where F is the applied force and A is the cross-sectional area of the sample (which varies with the strain). As this measurement again depends on a sample's cross sectional area, an alternate metric is the specific strength or tenacity (a term derived from the textile industry). The tenacity may be found by dividing the breaking force of a fiber by its linear density. Similar to the relationship between conductivity and specific conductivity, this is equivalent to dividing the yield strength by the sample's density.

CHAPTER 3: DEMONSTRATION OF THE SITE-SPECIFIC CVD TECHNIQUE

3.1. Development of the Chemical Vapor Deposition (CVD) Process

The first focal area of this dissertation is the development of the Joule heating driven CVD technique. In this chapter, the combination of a one-hour, permeating chemical vapor deposition (CVD) technique followed by conventional electroplating is explored.[93] In the first step, a Joule-heated carbon nanotube conductor is exposed to a bis(t-butylacetoacetato) copper(II) ($Cu(tBAOAC)_2$) CVD precursor. The higher temperature regions in the conductor cause the preferential decomposition of the copper-containing organometallic precursor to deposit nanoscale copper seeds, representing a "continuous filament heating CVD" (CFH-CVD) approach. This $Cu(tBAOAC)_2$ precursor is chosen due to its relatively low decomposition temperature and propensity for depositing small particles [94], which is ideal for targeting junctions within the CNT network. Thermal imaging is utilized to evaluate the heating of the roving towards the determination of proper temperature for deposition to occur. An electrodeposition step was employed to provide a cohesive overcoat, connecting the various areas of preferentially deposited copper seeds within the sample. The electrical properties (specific conductivity [19,20,30] and conductivity) of the Cu-CNT hybrid conductors are measured and compared to the literature on the basis of efficient metal utilization.

The chemical vapor deposition setup was assembled using a three-neck flask for the site-specific deposition of nanometal onto the CNT conductor. This setup is outlined in Figure 6a. The conductor chosen was an unspun CNT Miralon® roving material from

Nanocomp Technologies Inc., an image of which is presented at the top of Figure 6b. The roving is ribbon-like in form, with approximate dimensions of 30 µm × 1.8 mm and an average mass per length of 8.66 mg/m. It consists of a loose network of CNT bundles with an average density of 0.12 g/cm^3. The CNT roving is vacuum dried in an oven at 100°C for at least one hour prior to CVD or characterization.

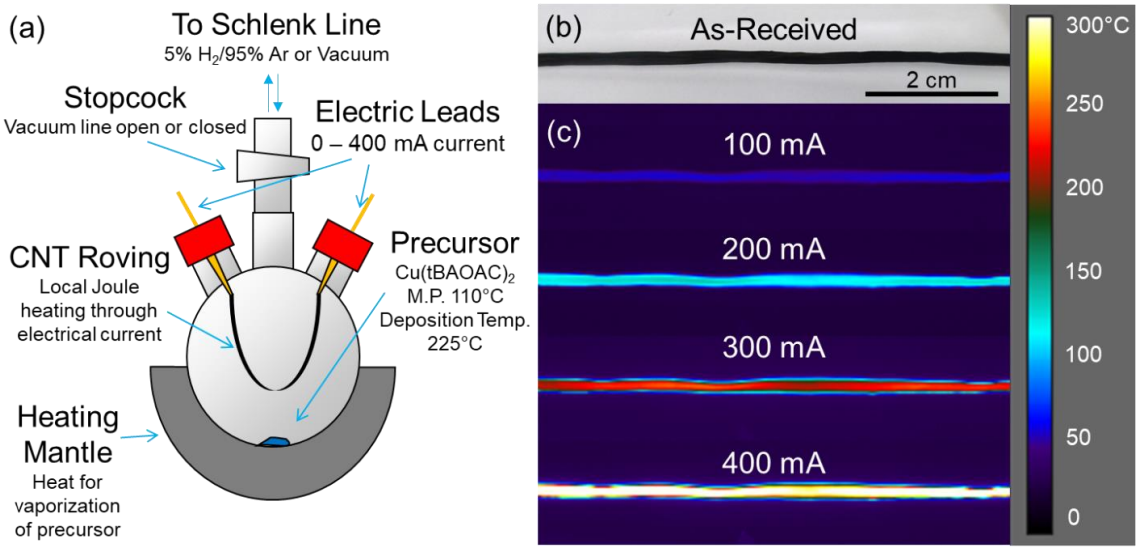

Figure 6**.** (a) The experimental setup utilized for chemical vapor deposition, illustrating the various process controls that may be modified. (b) Optical image of CNT roving. (c) Thermal images of CNT roving biased under various currents in air, exhibiting a direct relationship between temperature and current.

Thermogravimetric analysis and a Raman spectrum of this starting material are presented in Figure 7. The TGA establishes decomposition temperatures higher than 600°C in air and 15.4% residual ash at 1000°C. Raman data demonstrates a D/G ratio of 0.059, a G'/G ratio of 0.230, and a G'/D ratio of 3.89, indicating high purity CNTs in accordance with previous work [95].

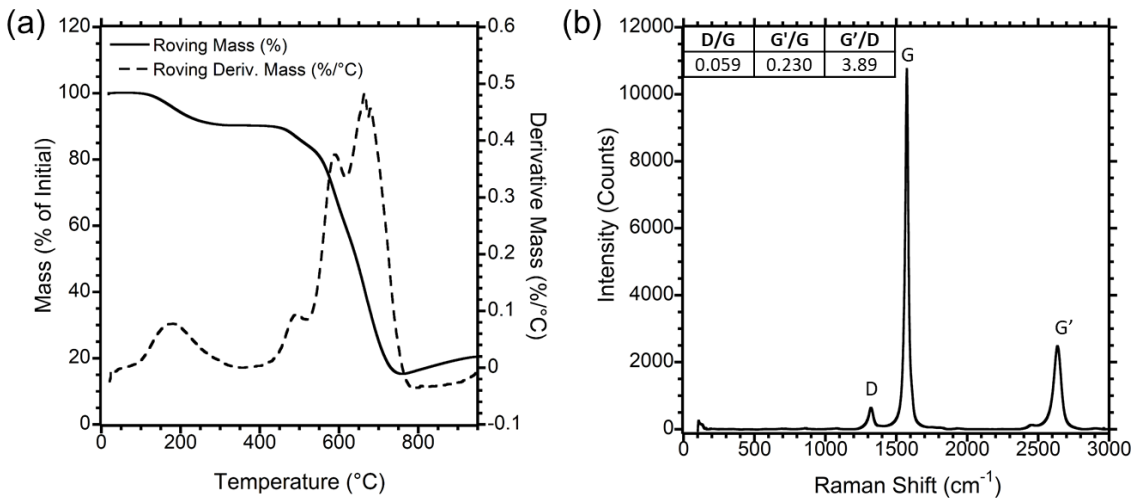

Figure 7. (a) TGA Curve of CNT roving from a TA Q5000. Sample heated using a ramp rate of 10°C/min to 1000°C in dry air. 15.4% residual ash at 1000°C. (b) Raman spectrum of CNT roving with peak ratios listed.

The CNT roving material was chosen due to its high porosity, which allows for greater penetration by the CVD precursor. The CNT roving is connected between two copper clips acting as electrical leads and suspended across the center of the flask above the CVD precursor. A 10-12 cm length of roving is chosen so that it remains suspended and does not contact any of the walls of the flask. The $Cu(tBAOAC)_2$ precursor (CAS #23670-45-3, 99%, Strem) is heated to a vapor by a mantle at the bottom of the flask. The entire flask is wrapped in glass wool to encourage more even heating. An electrical bias applied to the CNT roving promotes current flow which induces Joule heating, providing the thermal energy necessary to locally decompose the vapor precursor for deposition. The attachment of the flask to a Schlenk line allows for control over the local deposition environment within the flask, allowing for the application of vacuum or a reducing gas (5 mol% H_2/95 mol% Ar).

Initial tests were carried out to measure the effect of applied current on the CNT roving temperature. An electrical bias was applied to the roving in air, and temperature

measurements were determined with a FLIR A35 thermal camera (see Figure 6c), corrected for the measured CNT emissivity of 0.825 determined through ASTM E1933. The average temperature of the roving was determined from a line scan along the centerline of the roving. Average temperatures of 50°C at 100 mA, 130°C at 200 mA, 223°C at 300 mA, and 330°C at 400 mA are observed. At an applied current above 400 mA (a current density of ~7.4×10^6 A/m^2), samples were not consistently stable and could undergo failure over time. Under vacuum, it is expected that the roving reaches somewhat higher temperature than those measured here, due to the lack of convective cooling. The decomposition of the $Cu(tBAOAC)_2$ precursor is reported at 225°C [94], therefore, electrical bias conditions between 200 - 300 mA are expected to provide peak temperatures sufficient to cause deposition of the precursor to copper metal.

3.2. Parametric Studies

The effects of the electrical bias applied to the CNT roving during CVD are evaluated based upon the mass deposited and the nanoscale morphology analyzed via scanning electron microscopy (SEM). A scanning electron micrograph of the as-received CNT roving, prior to exposure to precursor is shown in Figure 8a. CNT bundles of various sizes (with diameters up to 100nm) are present, typically oriented along the axis of the CNT roving. An initial control sample with a heated mantle to evaporate the precursor, but no electrical bias through the roving during precursor exposure was prepared. The linear mass density of the roving increased by an average of 68.4%, indicating the condensation of the $Cu(tBAOAC)_2$ precursor onto the cooler roving. The electron micrograph for the sample without bias, Figure 8b, exhibits unreacted precursor

as a film on its surface, however, no nanoparticle formation. Strands of roving were subsequently biased at currents of 100 mA, 200 mA, 300 mA, and 400mA over the course of a one-hour CFH-CVD. In the standard continuous filament heating CVD (CFH-CVD) process, the flask is sequentially evacuated under vacuum then purged with 5% H_2/95% Ar four times. The flask is then evacuated for at least ten minutes prior to the deposition to reach a pressure of 166 mBar, after which the stopcock is closed. A constant electrical bias of 100, 200, 300 or 400 mA is applied to the roving to induce Joule heating, and the flask is heated using a heating mantle to a set temperature of 155°C over the period of 10 minutes to begin the evaporation of the $Cu(tBAOAC)_2$. As the flask heats, vacuum is applied every 20°C to ensure the low pressure is maintained within the flask until the deposition starts. The $Cu(tBAOAC)_2$ precursor typically evaporates from a liquid phase (melting at a mantle temperature of ~150°C) rather than sublimating from its solid state. The CVD setup is maintained at the set temperature for a period of one hour to allow the deposition to occur. After the deposition has occurred, the heating mantle is removed, and the flask is purged with 5% H_2/95% Ar. After allowing the flask to cool for five minutes, the electrical bias is removed and the vapor-deposited roving is removed for characterization. Sample surface morphology was evaluated via a Hitachi S900 SEM equipped with an immersion lens and backscatter electron detector. Secondary electron images were taken at 2 keV and backscatter electron images were taken at 10 keV. At 100 mA, Figure 8c, irregularly-shaped nodules of incompletely decomposed precursor are observed at various locations across the surface of the roving. At 200 mA, sparse nanoscale spherules are evident at various locations across the surface of the sample, as seen in Figure 8d. At 300 mA (see Figure 8e), an increase in the number of particles is

noted at locations in which they were observed. As Figure 8f shows, at 400 mA spherules are observed across the majority of the segments analyzed. Overall, between 200 mA and 400 mA for a one-hour deposition, the evolution from sparse collections of particles to more dense and uniform deposition of 10 – 40 nm particles is observed as the CNT roving's temperature exceeds the threshold current, with an average increase in linear density of 1.58 mg/m (14.85% of the hybrid mass).

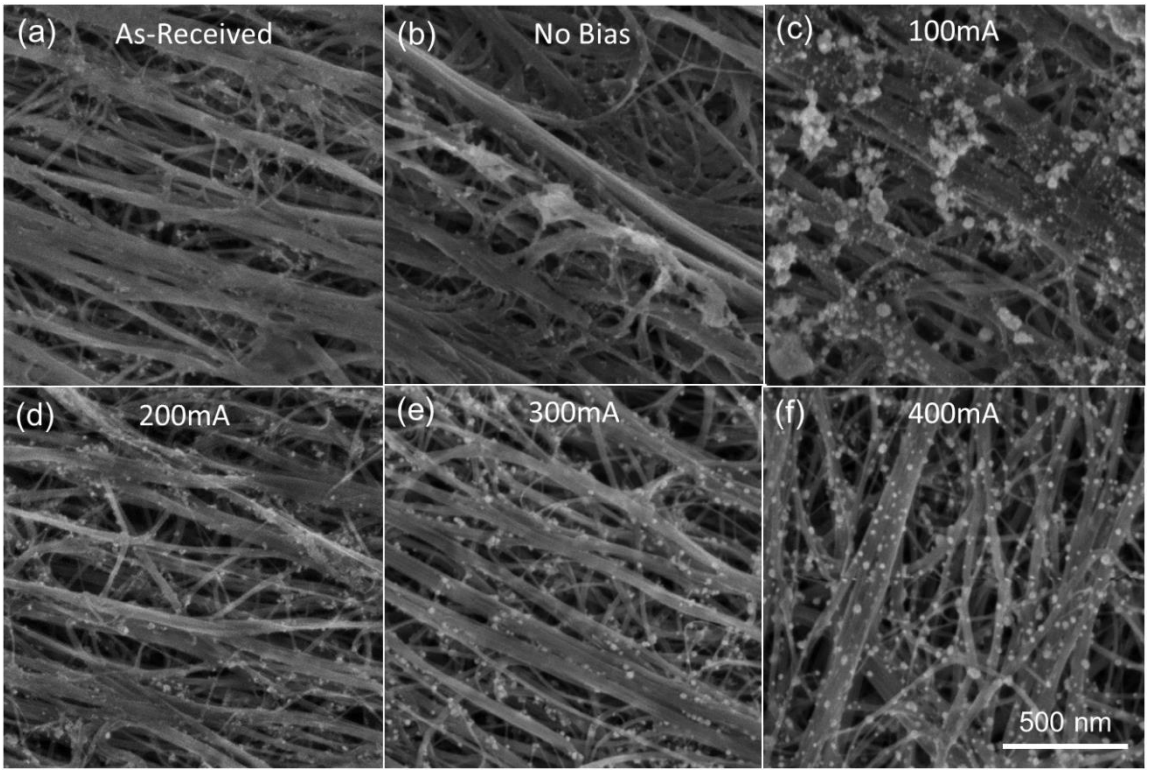

Figure 8. Secondary electron images of (a) as-received roving and roving after CFH-CVD (b) with no electrical bias, and at (c) 100 mA, (d) 200 mA, (e) 300 mA, and (f) 400 mA bias. Segments were taken for SEM analysis at least 1 cm from the end of the roving to minimize effects from conductive cooling through the electrical leads.

Studies into deposition time at a constant current of 300 mA reveal a saturation-type effect on the deposited mass in this CFH-CVD setup. In a half-hour deposition at 300 mA, an average mass increase of 8.42% is measured. Beyond this, all deposition times from 1 to 2 hours lead to comparable average deposited masses of 14-15% of the

composite mass, as is evident from Figure 9. The saturation of the vapor in the reaction vessel may be self-limiting the deposition due to the gaseous decomposition byproducts[94] of $Cu(tBAOAC)_2$, preventing further evaporation of the precursor.

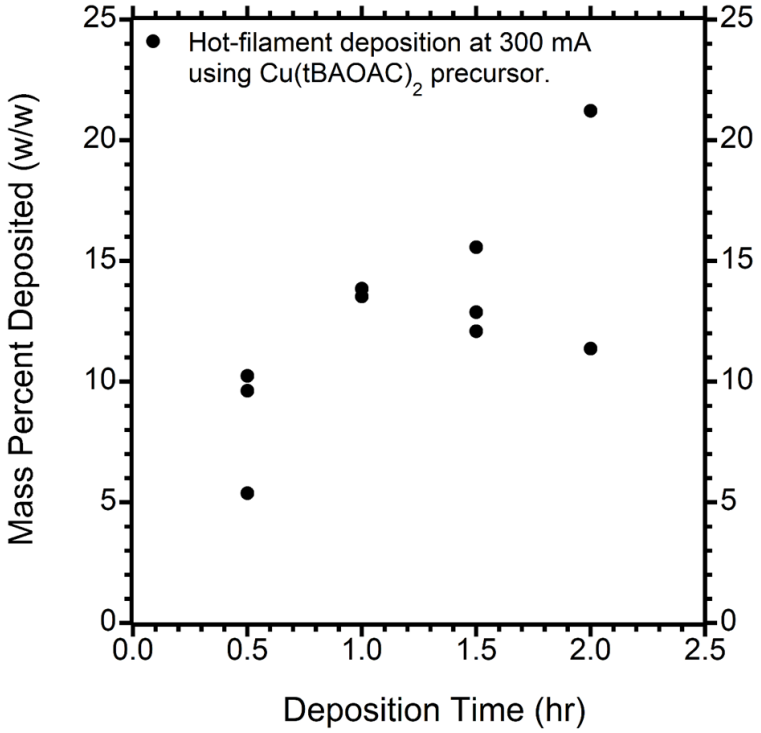

Figure 9. Added mass percent from CFH-CVD process. At 0.5 hr, the deposition does not appear to have reached a saturation point. For depositions between 1-2 hours, an average deposited mass of 14.41% of the hybrid mass is deposited.

A sample biased at 400 mA with a one-hour CFH-CVD was used as an archetypal example for further chemical and physical analysis. Under backscatter electron (BSE) imaging (Figure 10), high contrast was observed between the deposited spherules and the underlying CNT matrix, indicating a much higher Z element is present in the spherules.

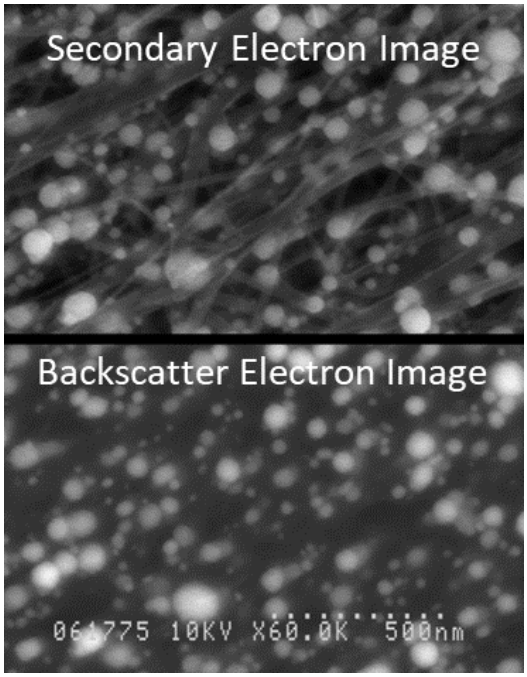

Figure 10. Backscatter electron imaging of a 400 mA CFH-CVD reveals that the deposited spherules are high-Z, and therefore likely metallic in nature. Due to the translucent nature of the CNTs in this image, it is possible to see spherules in the spaces between CNT bundles and below the surface of the CNT roving.

A Tescan Mira3 SEM equipped with a Bruker energy dispersive x-ray spectrometer (EDS) was used for elemental analysis of the sample surfaces. EDS confirms that the deposited spherules are copper, as is highlighted in Figure 11 (and in Figure 12 from a 300 mA deposition). Notably, the deposition yields a seeded roving with similar resistance (375 Ω/m) to a control roving sample exposed to similarly high current (386 Ω/m). This is attributed to the fact that the deposited Cu metal exists as discretized spherules rather than a continuous film, as has been observed in other studies of Cu-CNT composites [56,57].

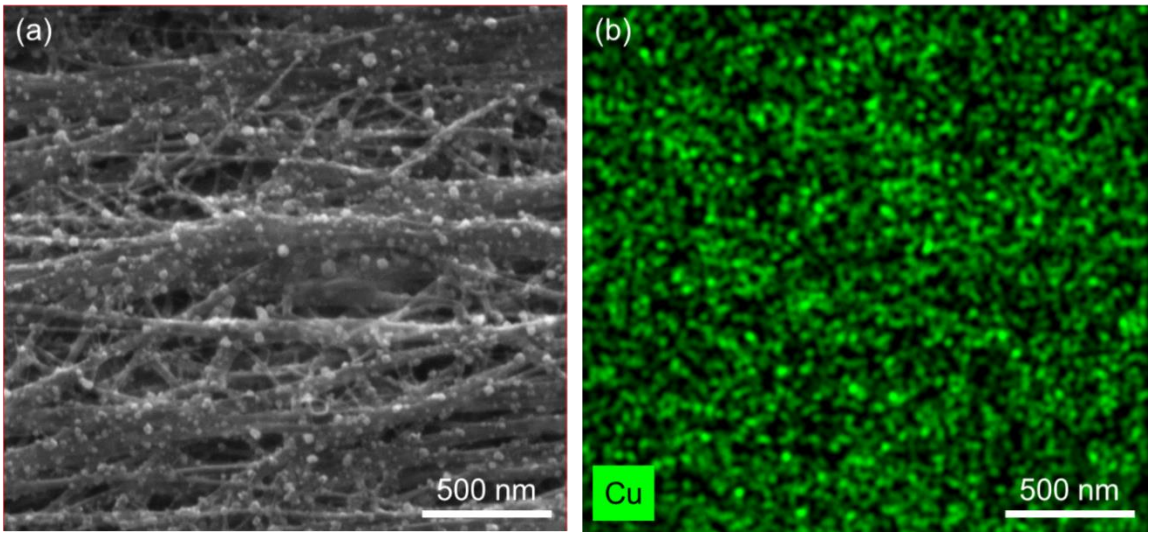

Figure 11. EDS imaging of a 400mA CFH-CVD sample. (a) Secondary electron map with area of analysis bordered by red box. (b) EDS spatial map of copper signal, with copper in green.

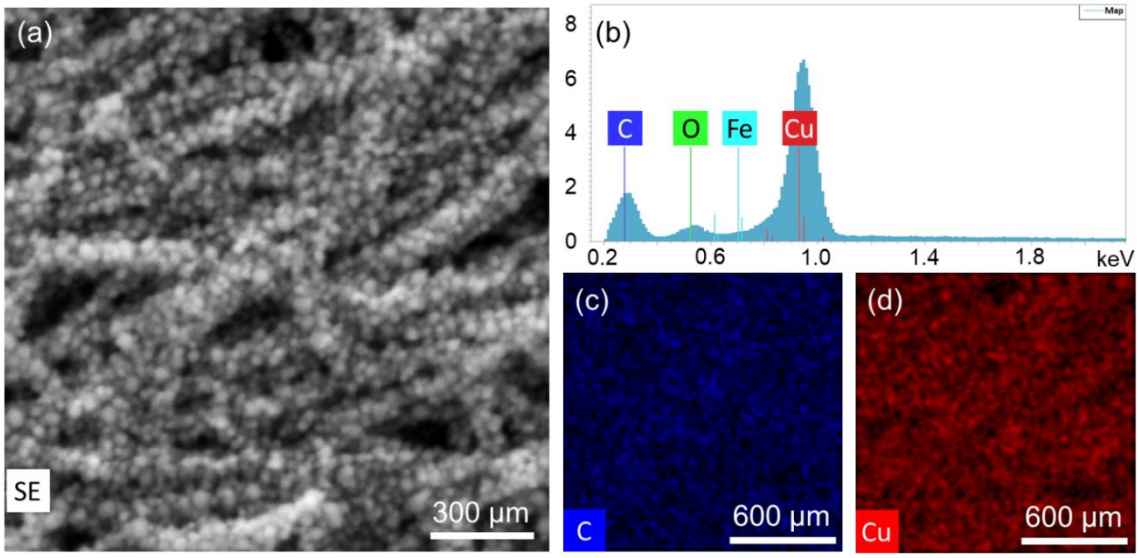

Figure 12. (a) Secondary electron map of a 300mA CFH-CVD sample. (b) Histogram of EDS signal frequency from the analyzed region (c) Spatial map of carbon signal. (d) Spatial map of copper signal.

For cross-sectional imaging, the focused ion beam (FIB) milling, imaging and EDS were performed in a FEI scanning electron microscope (SEM)/Ga liquid metal ion source (LMIS) dual-beam tool, equipped with an Oxford Instruments X-Max 80 mm EDS x-ray detector. A CNT wire, mounted on a 45° Al stub and tilted 7° to align its

surface normal with the FIB axis, was FIB cross-sectioned in three steps. A 30 keV Ga ion beam at 19 nA was used for the initial cut. Clean-up cuts were performed with an 8 keV Ga ion beam at 2.8 nA. The lower energy and ion beam current of the clean-up cuts helped to reduce damage of adjacent features and reduced the concentration of Ga near the surface. EDS mapping was performed using a 20 keV electron beam rastered over a region 2µm × 12 µm region at a tilt angle of 30° yielding an incident angle of 75°. The FIB cross-section of this sample (Figure 13) confirms that the deposition is present throughout the thickness of the low-density roving. Combined with a copper overcoat, this may prove useful for connecting interior areas of the sample, providing additional conductive pathways beyond those that may be achieved through a metal overcoat alone.

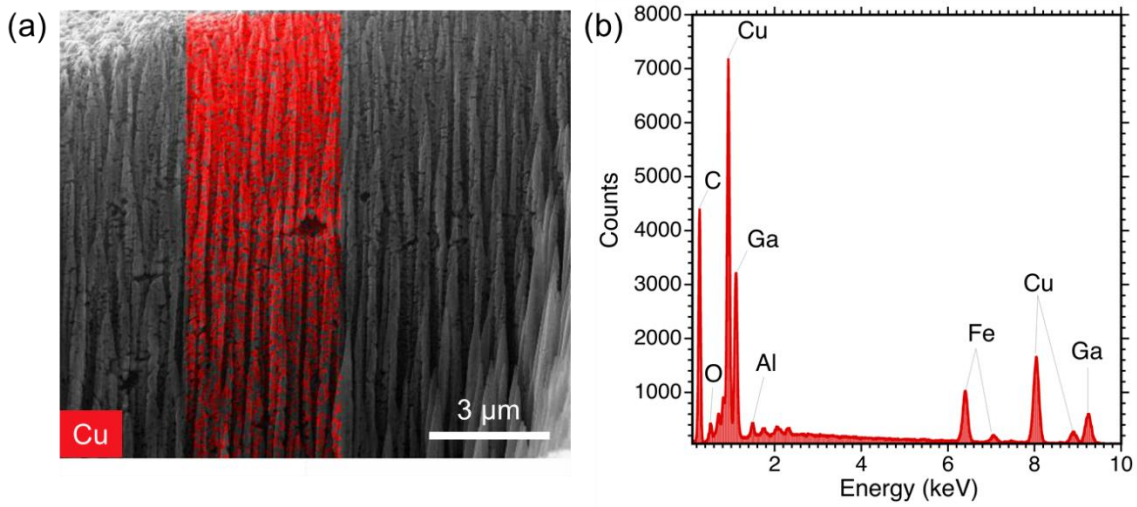

Figure 13. (a) EDS scan of the cross-section of the composite revealed by gallium FIB milling. Sample surface is visible at the top left of the image. Copper signal strength overlaid in red, demonstrating penetration of deposited copper towards the center of the 30 µm thick roving. (b) Histogram of signal frequency counts, demonstrating the prominence of the copper signal in the analyzed region.

For comparison with the standard CFH-CVD setup, an alternate approach in a "delayed filament heating CVD" (DFH-CVD) setup. For the DFH-CVD method, no electrical bias is applied to the CNT roving during the one-hour deposition process. However, the precursor is still heated to 155°C. Due to the lack of gaseous thermal decomposition byproducts, an increased mass of $Cu(tBAOAC)_2$ is expected to condense upon the roving conductor, since the pressure within the flask should not rise above the threshold of $Cu(tBAOAC)_2$ vaporization during the deposition. After the condensation has occurred, the flask is purged with 5% H_2/95% Ar. A current of 400 mA is then applied to the roving to induce Joule heating and cause the decomposition of the precursor. Slightly higher deposited masses of 16.11% were obtained through the DFH-CVD method after the one-hour deposition followed by a 400 mA bias applied under 5% H_2/95% Ar. However, examinations of particle morphology reveal the nanoscale copper spherules noted under CFH-CVD (Figure 14a,b) have been replaced by larger microscale spheres of copper (Figure 14c,d) The change in particle size could be caused by the adhesion of the $Cu(tBAOAC)_2$ film to itself during decomposition. Since there is limited adhesion between CNTs and metallic copper [58,96], the precursor may ripen into larger spheres rather than locally depositing as nanoparticles. Thus, it would appear advantageous to have consistent electrical bias applied throughout the deposition process, to ensure that hot spots on the CNT roving decompose the precursor locally.

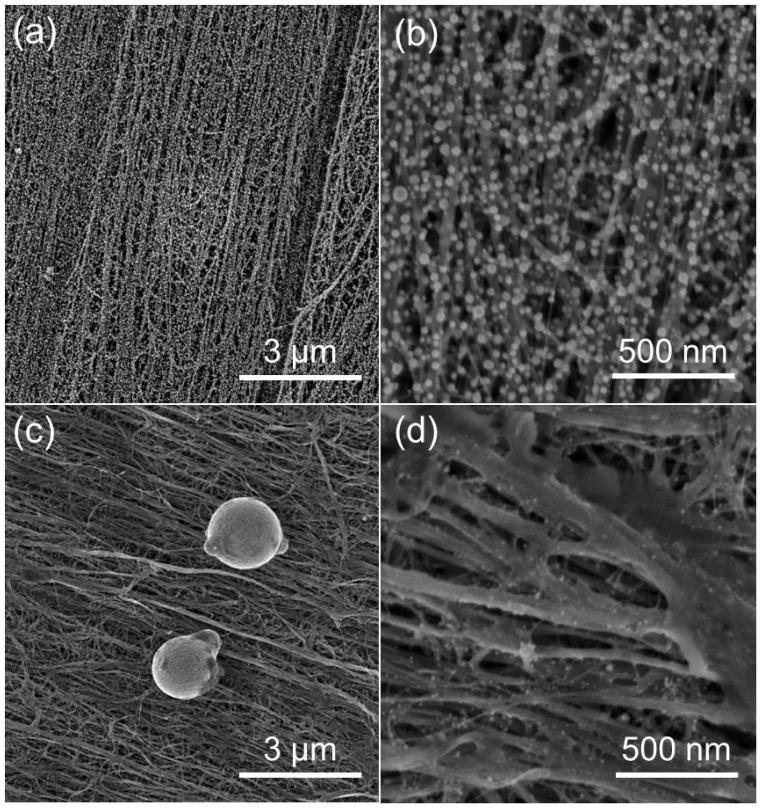

Figure 14. (a) Low and (b) high magnification images of a 400 mA CFH-CVD. (c) Low and (d) high magnification images of a DFH-CVD with 400 mA bias at the end of the test.

3.3. Achieving Site-Specific Deposition

While 400 mA was able to produce a uniform deposition along the roving, 300 mA is a more stable condition to evaluate whether site selectivity is possible during deposition. Thus, CFH-CVD was also performed with a 300 mA bias on a length of roving into which a knot had been tied (Figure 15a) to evaluate whether location-specific heating is a cause of preferential copper deposition from the vapor phase precursor. Thermal imaging in air demonstrates that the presence of a knot in the CNT roving can generate a localized hot spot under bias, as shown in Figure 15b.

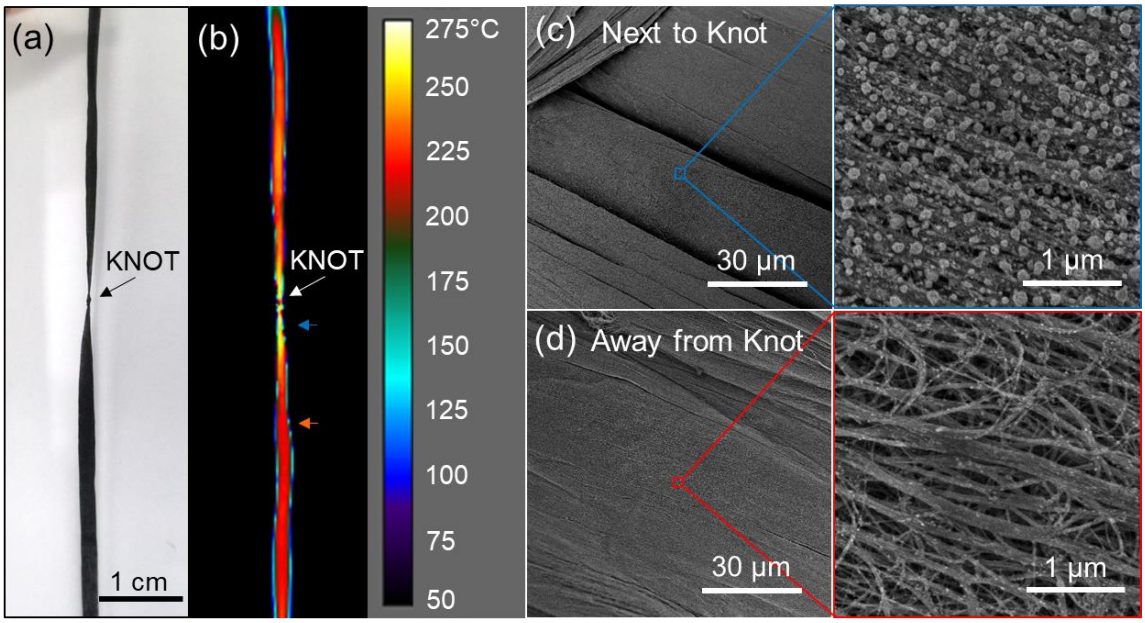

Figure 15. (a) A knot tied in the roving is able to generate a hot spot in neighboring regions, here demonstrated through (b) thermal images of a 300 mA bias in air. (c) SEM images of the region next to a knot after a 300 mA deposition. The knot is visible in the upper left of the image. (d) SEM images of a region ~1 cm away from the knot.

Figure 16 establishes that the presence of hot spots can also be verified through incandescence at higher applied currents (≥450 mA) under vacuum. After the one-hour, 300 mA CFH-CVD, segments from a knotted piece of roving were characterized by SEM. Heavy amounts of deposited copper are observed at and immediately around the knots, as in Figure 15c. At the distance of ~1 cm away from the knots, the deposition appears much lighter, as in Figure 15d. Thus, the results indicate that metal is preferentially deposited with higher local temperature – a key potential advantage of this technology over nonspecific deposition methods such as electrodeposition or sputtering. Although the present focus demonstrates macro- to milli-scale control over depositions, closer modulation of the current may allow for the tuning of the deposition towards the nanoscale if individual CNT to CNT junctions are able to be selectively heated.

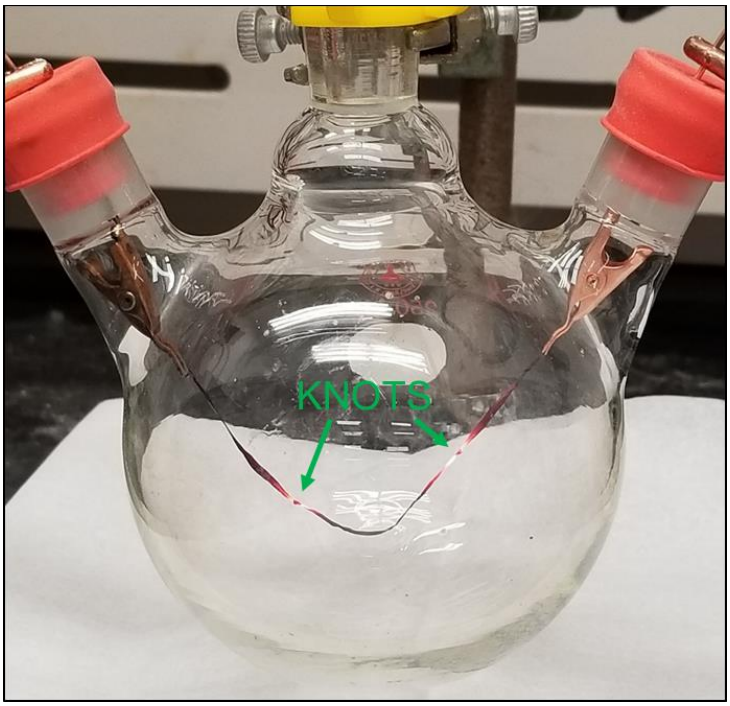

Figure 16. Image of CNT roving under 450 mA electrical bias in vacuum with two knotted regions, exhibiting two separate localized zones of incandescence around the knots.

3.4. Electrodeposition of Copper Overcoat and Finishing

A copper overcoat was electrodeposited onto samples which had undergone CFH-CVD seeding pretreatment with a bias of 300 mA to produce finished electrical conductors. In recent literature, metallic fractions of over 90% of the composite mass are common [53,55,56,58,64]. This is primarily due to the drastic difference between the densities of copper (8.96 g/cm^3) and carbon nanotubes (0.12 g/cm^3 for roving, towards 1 g/cm^3 or higher in compressed wires [47,52,70,97]), which leads to composites that are around 50% copper by volume. In the present work, a variety of copper mass loadings were evaluated to provide a more complete understanding of the impact of the CVD pretreatment. All electroplating was carried out against copper anodes in a sandwich-cell configuration with a plating current of 12 A/g_{roving} for pre-determined times between one

minute and one hour (Figure 17). In the sandwich-cell configuration, the sample was inserted within a folded piece of Whatman 42 filter paper to act as a separator. A piece of copper foil was wrapped around the filter paper to act as a counter electrode. This entire setup was sandwiched between two glass slides and secured with Kapton tape to provide compression and ensure constant distance between the CNT roving working electrode and copper counter electrode. The electrochemical cell was then submerged into a bath of acid copper electroplating solution (Transene). Electroplating was carried out under constant supplied current from an Arbin BT2000 battery tester. A constant cathodic current of 12 A/g_{roving} was applied over deposition times ranging from one minute to one hour (depending on the mass loading targeted). After electroplating, samples were rinsed with deionized water, and allowed to dry for 1 hour at 100°C under vacuum.

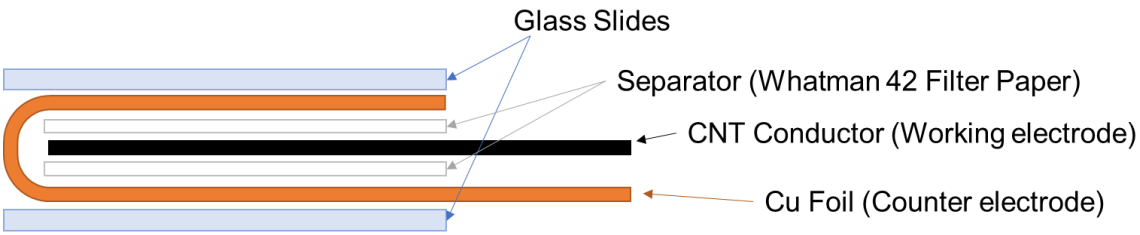

Figure 17. Schematic of the sandwich cell configuration for electroplating

Here, current is presented proportionally to the mass of the CNT roving (as A/g_{roving}) due to the porous, nanoscale network of the CNTs, which may lead to variation in local surface area along the length of the roving. Densification of the electroplated CNT wires was carried out in a rolling mill [97] to produce a ribbon-like conductor. Twenty passes were made through the rolling mill, reducing the gap by 1 μm every other pass. Finally, samples were annealed under 5% H_2/95% Ar gas at 300°C for 3 hours to reduce any remaining copper oxides and ensure good electrical contact between copper particles.

Figure 18a plots the specific conductivity of samples with and without $Cu(tBAOAC)_2$ CFH-CVD as a pretreatment for electroplated CNT roving. The specific conductivity is defined as the bulk electrical conductivity normalized to sample density and provides a direct comparison of the gains made through metal incorporation and finishing [19,30]. The specific conductivity value relies on measurements of resistance per length and mass per length, thus avoiding the need to measure the cross-sectional area of each sample. The equation is given by:

$$\sigma_{sp} = \frac{\sigma}{D} = \frac{\frac{L}{RA}}{\frac{M}{LA}} = \frac{L^2}{RM}$$

where σ_{sp} is the specific conductivity, σ is the conductivity, D is the sample density, L is the length of the conductor, R is the resistance, A is the cross-sectional area, and M is the mass [19]. The independence from cross-sectional area accounts for any variations in density between lengths of roving, and gains made through densification and annealing can be attributed to decreases in the linear resistance of the sample. The samples were massed before and after the CVD and electroplating depositions using a Mettler Toledo XP-2U microbalance, and their lengths were measured using high-precision calipers. Electrical resistance was measured using a four-point probe connected to a National Instruments NI PXI-5652 source/measure unit and an NI PXI-4071 digital multimeter at room temperature (~20°C) through a current-potential sweep. Room temperature specific conductivity values in Figure 18a are presented after electroplating, after densification through calendaring, and after annealing. Below 60% mass loading, decreases in the samples' resistance were offset by increases in sample mass, leading to neutral (for CVD seeded) or negative (for non-seeded) changes in specific conductivity. While decreases in

resistance per length are observed (156 Ω/m at 54.9% Cu after annealing for CVD seeded compared to 368 Ω/m for 61.2% Cu after annealing with no CVD seeding), the small volume fraction of the copper overcoat is likely unable to produce a strong electrical percolation network throughout the CNT roving. Between 54.9% w/w Cu and 78.9% w/w Cu, substantial increases are observed in the specific conductivity of the CVD pretreated samples. Specific conductivity values as high as 5632 S·m²/kg (with resistance per length of 1.14 Ω/m) are attained for a sample with 94.2% copper mass. However, without CVD pretreatment, there is no substantial change in the specific conductivity of the electroplated samples. At 94.1% Cu, electroplated CNT roving has resistance per length reduced to 26.0 Ω/m, yet only reaches a specific conductivity of 218 S·m²/kg, substantially lower than the 407 S·m²/kg starting specific conductivity of the roving. This indicates much improved utilization of the electrodeposited copper mass through the selective deposition of Cu from the $Cu(tBAOAC)_2$ precursor.

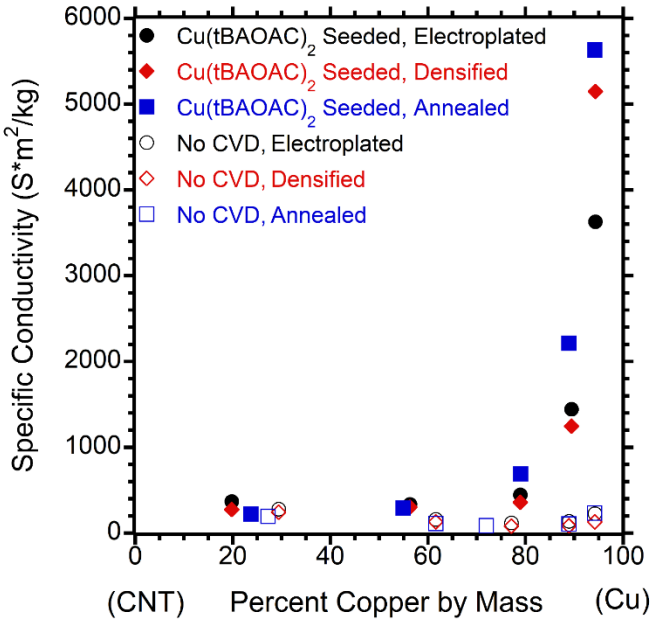

Figure 18. Specific conductivity of electroplated Cu-CNT hybrids with and without Cu seeding from $Cu(tBAOAC)_2$ plotted against total deposited Cu mass.

3.5. Benefits of Hybrid Conductors

A measurement of the temperature coefficient of resistance (TCR) of the $Cu(tBAOAC)_2$ seeded Cu-CNT hybrid conductors were taken under vacuum over the range of 300 K to 600 K. The temperature coefficient of resistance (TCR) was measured using a four-point probe setup within a Janis cryostat connected to a National Instruments NI PXI-4110 Programmable Power Supply and an NI PXI-4072 digital multimeter through a current-potential sweep. Resistance was measured at 10^{-6} mBar every 5 K over the range of 300 K to 600 K. Two cycles of temperature were measured and data from the second cycle is presented to minimize effects of temperature annealing through the first cycle. The TCR was determined from the average slope of the resistance relative to 300 K. As the mass fraction of Cu increases, the TCR for the Cu-CNT hybrid conductors, measured with respect to 300K, appears to follow a much more positive (metal-like) trend than the as-received CNT roving (which has a TCR of 2.18×10^{-4} K^{-1}), as displayed in Figure 19. However, even at 94.2% w/w Cu the $Cu(tBAOAC)_2$ seeded and electroplated sample's average measured TCR_{300K} of 3.53×10^{-3} K^{-1} is still lower than the standard 3.83×10^{-3} K^{-1} for annealed copper [25]. This lower TCR leads to less relative loss in conductivity at elevated temperatures.

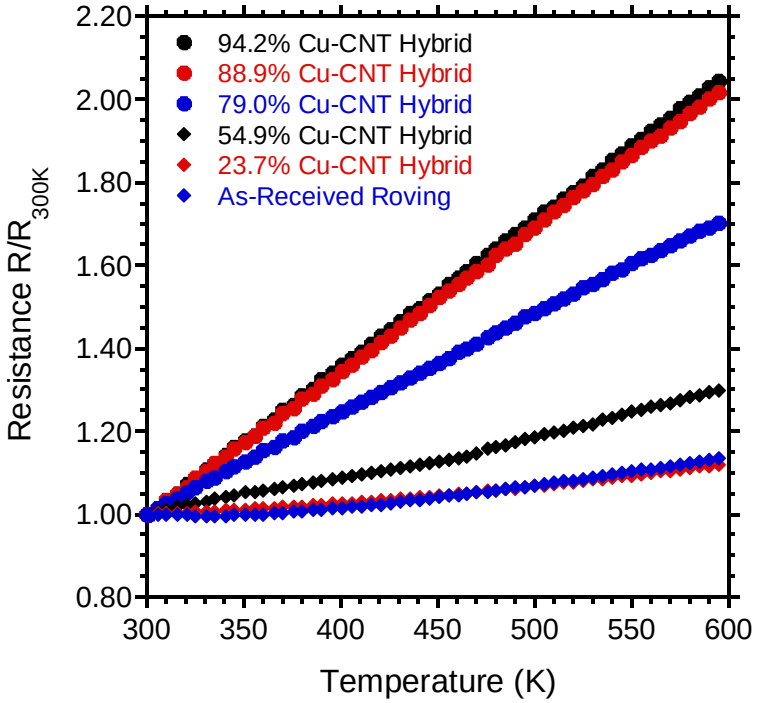

Figure 19. Temperature dependent electrical resistance measurements (relative to 300 K) under vacuum for each of the finished Cu-CNT hybrid conductors and the as-received CNT roving. The temperature coefficient of resistance (TCR) is determined from the average slope of resistance relative to 300 K.

One proposed advantage of the Cu-CNT hybrid conductor for applications at elevated temperatures is the beneficial combination of high specific conductivity at a lower TCR. Consider a limiting case in which the Cu and CNT fractions of a conductor operate as discrete, non-interacting layers. Each layer could be envisioned as carrying a portion of the current, and thus on the bulk scale the system could be modeled as parallel resistors. In such a case, the expected specific conductivity and TCR may be determined based on the mass fraction of Cu and CNTs in such a layered structure with the intrinsic values for the pure materials (as shown below):

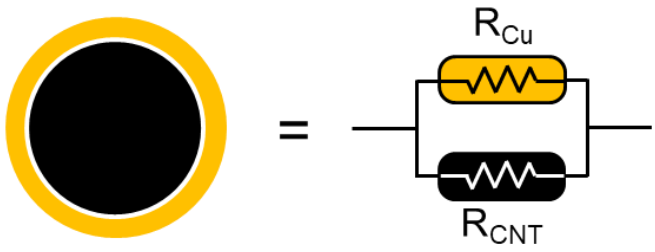

Discrete Layers Parallel Resistors

Specific Conductivity

The resistance may be determined from the equation for specific conductivity as:

(1) $$R_x = \frac{l_x^2}{\sigma_{sp,x} * m_x} \quad (1)$$

Given the parallel resistors equation:

(2) $$\frac{1}{R_{tot}} = \frac{1}{R_{Cu}} + \frac{1}{R_{CNT}}$$

Substituting (1) into (2):

(3) $$\frac{\sigma_{sp,tot} * m_{tot}}{l_{tot}^2} = \frac{\sigma_{sp,Cu} * m_{Cu}}{l_{Cu}^2} + \frac{\sigma_{sp,CNT} * m_{CNT}}{l_{CNT}^2}$$

Since the conductors are assumed to be similar length:

(4) $$l_{tot}^2 = l_{Cu}^2 = l_{CNT}^2:$$

Equation (3) simplifies to:

(5) $$\sigma_{sp,tot} * m_{tot} = \sigma_{sp,Cu} * m_{Cu} + \sigma_{sp,CNT} * m_{CNT}$$

An equation for specific conductivity is then found:

(6) $$\sigma_{sp,tot} = \frac{\sigma_{sp,Cu} * m_{Cu}}{m_{tot}} + \frac{\sigma_{sp,CNT} * m_{CNT}}{m_{tot}}$$

Temperature Coefficient of Resistance

As above, the resistance at a given reference temperature T_0 can be shown to be:

(7) $$R_{0,tot} = l^2 * \left(\sigma_{sp,\ Cu} * m_{Cu} + \sigma_{sp,\ CNT} * m_{CNT}\right)^{-1}$$

Using the equation for linear (metallic) TCR measurements:

(8) $$\alpha = \frac{\left(\frac{R}{R_0} - 1\right)}{(T - T_0)}$$

Reorganizing (8), and substituting (1) for R_0, the resistance of one resistor, R_x, at temperature T is:

(9) $$R_x = \frac{l_x^2}{\sigma_{sp,x} * m_x} \beta_x$$

where $\beta_x = [1 + \alpha_x(T - T_0)])$

Substituting (9) for R_{Cu} and R_{CNT} into (2), we get an equation for the total resistance R_{tot} at temperature T:

(10) $$R_{tot} = l^2 * \left(\frac{\sigma_{sp,\ Cu} * m_{Cu}}{\beta_{Cu}} + \frac{\sigma_{sp,\ CNT} * m_{CNT}}{\beta_{CNT}}\right)^{-1}$$

Substituting (7) and (10) into (8), we obtain an equation for the total TCR, a_{tot}:

$$\alpha_{tot} = \frac{\left(\frac{R_{tot}}{R_{0,\ tot}} - 1\right)}{(T - T_0))}$$

The predicted value relationship for TCR vs. room temperature specific conductivity over the continuum from 100% Cu conductor to 100% CNT roving conductor is shown in Figure 20. The measured values obtained for the finished $Cu(tBAOAC)_2$ seeded and electroplated samples are also shown on this graph. Between 88.9% and 94.2% w/w Cu, the $Cu(tBAOAC)_2$ seeded and electroplated hybrids "cross-over" the threshold line representing the parallel resistors model. Therefore, the 94.2% w/w CNT-Cu hybrid represents a better combination of TCR and specific conductivity than would be expected from a simple combination of its constituent materials. Thus, there is evidence that the combination of CNTs and Cu in the material presented exhibit properties of a true hybrid rather than a layered composite.

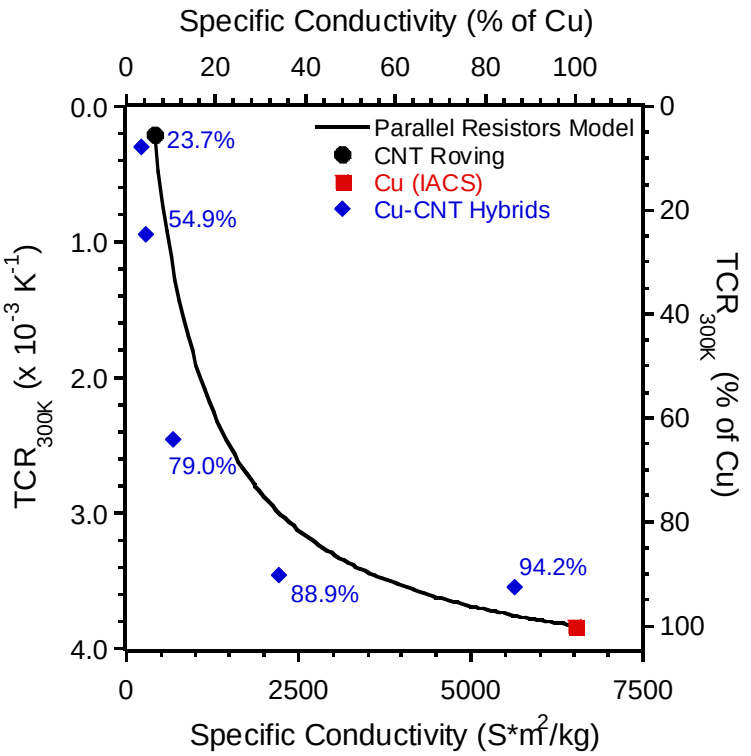

Figure 20. Plot of the TCR and specific conductivity of Cu-CNT hybrid conductors compared to copper, CNT roving, and calculated combinations of the two materials based on the parallel resistors model.

Mechanical properties for a 94.2% w/w Cu-CNT hybrid are presented in Figure 21. The tensile strength of 92 MPa and Young's modulus of 11.6 GPa fall in between values obtained from the as-received roving (58 MPa tensile strength, 2.75 GPa Young's modulus) and a 12 µm copper foil with similar linear mass density and width to the sample (225 MPa tensile strength, 40.9 GPa Young's modulus).

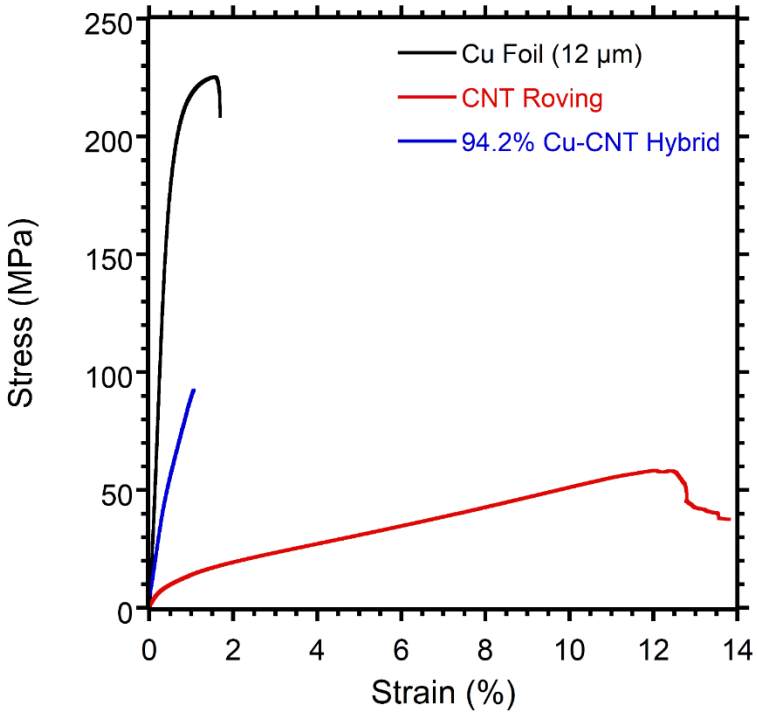

Figure 21. Engineering stress-strain curve for Cu, CNT roving, and a 94.2% Cu-CNT Hybrid. The Cu foil was 12 µm thick battery-grade foil with similar mass per length (~160 mg/m) and width (1.71 mm) to the Cu-CNT hybrid.

A cyclic bending test was carried out by wrapping the samples around a 4.5 mm diameter glass rod mounted at an angle ~12° from the perpendicular to the sample. Each end of the sample was attached to a movable stage with adhesive tape. By translating the stage along the sample's length, the entire length of the sample was made to bend around the glass rod and then re-straighten. Figure 22 demonstrates that the annealed 94.2% w/w Cu-CNT hybrid exhibits less than 3% increase in resistance over 1000 bend cycles,

consistent with properties for 12 µm Cu foil. Results from a 12 µm thick piece of copper foil with similar mass per length (~160 mg/m) and width (1.71 mm) to the Cu-CNT hybrid is presented for comparison.

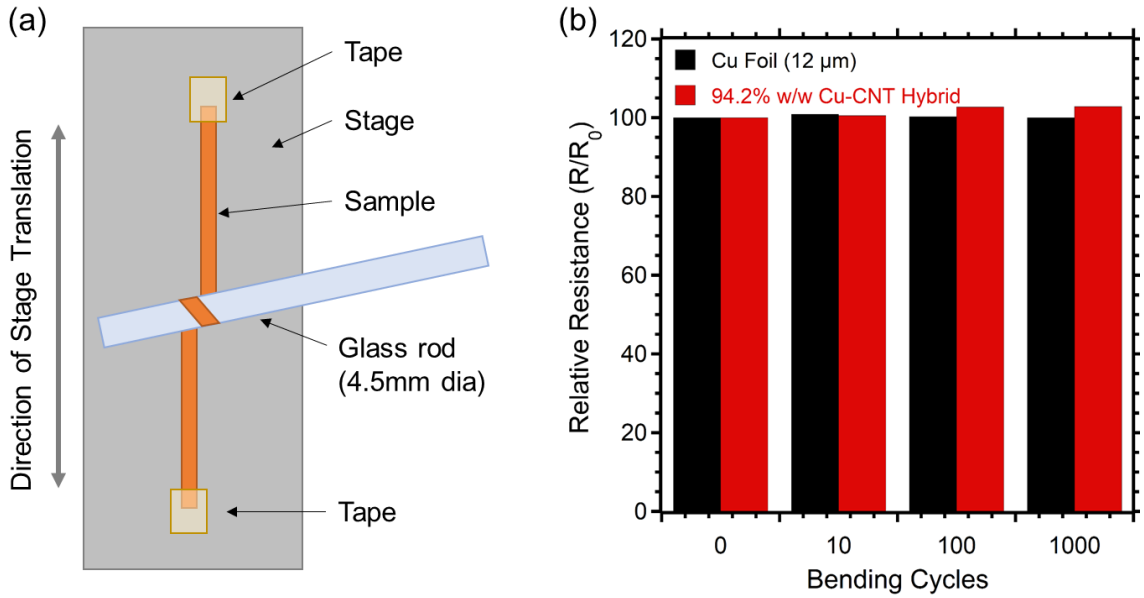

Figure 22. (a)The cyclic bending test setup. (b) Change in resistance with increasing number of bending cycles around the 4.5 mm diameter glass rod.

The conductivity of the 94.2% w/w Cu-CNT hybrid sample was determined by measuring the width of the sample via optical microscopy and thickness via SEM (Figure 23). The cross sectional area was determined to be $3.04 \times 10^{-8}\,m^2$ at the cut section of the Cu-CNT hybrid, resulting in a room temperature electrical conductivity of 2.81×10^{7} S/m.

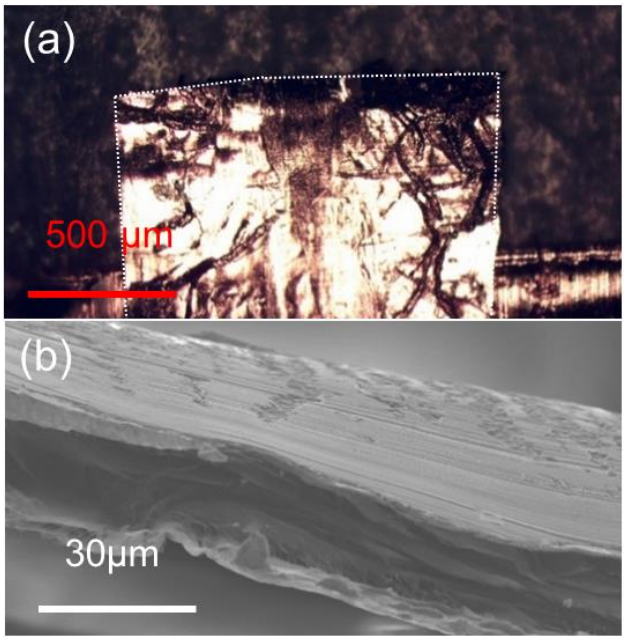

Figure 23. (a) Optical image used to assess width of the 94.2% Cu hybrid conductor (outlined in white). (b) SEM image of cross-section used to determine thickness of the same.

Figure 24 compares the present work to other recently published Cu-CNT hybrid conductors, where the electrical conductivity result from the combination of CFH-CVD with aqueous electrodeposition is among the highest reported at this mass loading of copper. This is particularly notable in that a low density (0.12 g/cm^3) (and high void space) starting material with an electrical conductivity at room temperature of only 4.94×10^4 S/m was enhanced by 569 times the original electrical conductivity. Thus, the CVD and electroplating technique is expected to be adaptable to various quality CNT conductor starting materials. Furthermore, the measured composite density of 5.14 g/cm^3 is only 61.4% of the calculated value for a sample consisting of 5.8% CNT roving and 94.2% Cu by mass based on a rule-of-mixtures. Optimizing this conductor density through improved densification techniques may yield further gains even without major process modifications. Overall, the CVD process is a demonstrated technique to

selectively deposit nanometal Cu seeds onto CNT roving for enhanced electroplating utilization leading to hybrid structures with high electrical conductivity.

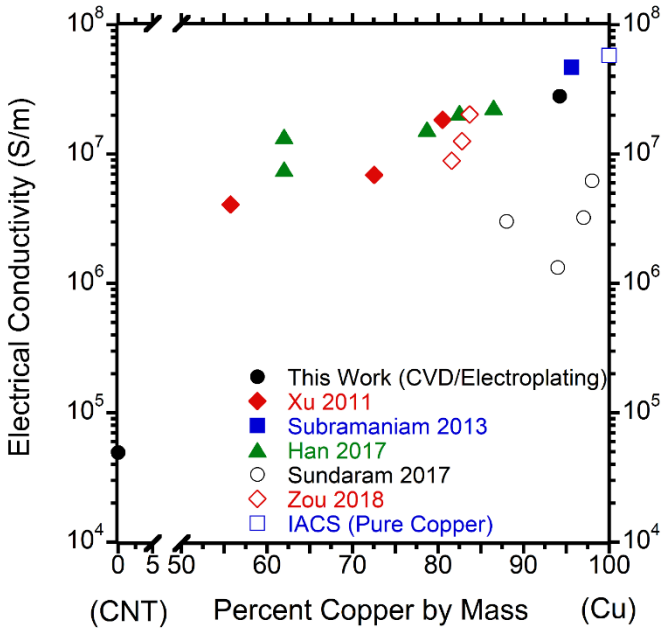

Figure 24. Room temperature conductivity of a 94.2% Cu composite produced through nanometal deposition of $Cu(tBAOAC)_2$ followed by copper electrodeposition, compared with other recent literature results: Xu 2011 [79], Subramaniam 2013 [53], Han 2017[58], Sundaram 2017 [56], Zou 2018 [55]. It is important to note that while some of the literature samples contain small mass fractions of other metals (e.g. Ni) [58], Cu is the majority metal within every composite.

3.6. Conclusions

The site-selective CVD of nanometal copper from $Cu(tBAOAC)_2$ has been demonstrated as an effective pretreatment method for the production of high conductivity copper-CNT hybrid conductors. Using Joule heating of a CNT conductor to drive the CVD process is a robust, tunable, and scalable method towards more efficient use of metal mass within hybrid bulk conductors. The combination of CVD with conventional electroplating techniques outperforms standard electroplating over a wide range of mass

loadings. Copper-CNT hybrids with room temperature specific conductivities of 5632 $S \cdot m^2/kg$ and electrical conductivities of 2.81×10^7 S/m have been demonstrated with this approach. These results represent increases of 13.8× and 569× the as-received CNT roving's specific conductivity (407 $S \cdot m^2/kg$) and conductivity (4.94×10^4 S/m), respectively. Further tuning of the nanometal seed mass and distribution through adjustment of the deposition parameters may produce even better utilization of added Cu mass. The CVD process also can be adapted to a wide variety of precursors using various metals and presents a significant opportunity for advancing the field of metal-CNT hybrid conductors. Certain metals, such as platinum, palladium, or nickel that have improved bonding interactions towards carbon nanotubes may prove to be even better candidates for such vapor deposited seeds. The utility of this method lies in the fact that the CVD-produced seeds are uniquely deposited in localized regions due to the temperature differences (from the localized resistance) which contrasts with previous electroplating work where seed deposition is non-specific. While this paper has demonstrated macro- to micro-scale control over depositions, further selectivity towards the nanoscale could potentially be obtained through the application of a pulsed current through the CNT substrate that would modify the localized heating. Additionally, the process timescale for CVD seeding can be minutes to hours rather than hours to days for previous electroplating seed procedures. Thus, the described approach represents an emerging strategy to fabricate various metal-CNT hybrid conductors with enhanced temperate-dependent electrical properties for applications like rotating machinery and electric motors.

CHAPTER 4: CONTROL OF CVD SEED MASS AND MORPHOLOGY

4.1. Introduction

While the initial development of the Joule heating driven CVD technique demonstrated the ability to produce uniform or site-specific depositions, a constant seed mass of 14-15% w/w was deposited in each of the final samples. However, this is not necessarily the ideal seed density in an optimized conductor. Depending on the target conductor properties and metals utilized, it is important to be able to control the deposited mass and morphology of the nanometal seeds. Fortunately, there are a number of CVD parameters that can be adjusted to potentially modify the resultant depositions. These parameters include the deposition time, precursor temperature (adjusted via the heating mantle temperature), system pressure, precursor mass utilized, the amount of applied current, and the interval of applied current.

The first three parameters (deposition time, precursor temperature, and system pressure) deal with the sublimation rate and kinetics of the precursor. Increased deposition time allows for more of the precursor to sublimate before the end of the CVD run. Higher precursor temperatures increase the sublimation rate of precursors, allowing for faster depositions. However, the temperatures are limited by decomposition temperature of the precursors. Similarly, lower pressure increases the kinetic rate of sublimation [94,98–100]. The effect of the fourth parameter, precursor mass, is straightforward. Higher precursor mass allows for the higher total deposited mass, in configurations where the precursor is allowed to sublimate completely. The effects of the

final two parameters dealing with the applied current are more nuanced. As shown in the initial study [93], lower applied currents lead to site-specific depositions, when localized hot-spots are of sufficiently high temperature to decompose the precursor, while higher applied currents lead to more generalized depositions. In such situations where the deposited seeds do not lower the resistance of the conductor, this does not necessarily impact the total deposited mass. However, if the density of deposited seeds is sufficient to decrease the resistance of the conductor, the conductor will experience less Joule heating. Less Joule heating results in lower temperatures, which may halt the deposition process. In such situations, lower currents resulting in localized hot spots would experience lighter depositions than higher currents with a larger proportion of high temperature surface area. A similarly complex effect is likely with changing the interval of applied current. In situations like the initial study [93] where it seems that decomposition byproducts prevent further precursor sublimation, the deposited mass from a DFH-CVD is higher than that of the CFH-CVD. However, under conditions where the precursor sublimates completely, the DFH-CVD would deposit lower masses that the CFH-CVD since only the vapor that recondenses upon the cool CNT roving would be available for decomposition at the end of the run.

4.2. Modifications to the CVD Setup

Where indicated, the CVD experimental setup may be modified to deposit onto three roving in parallel to allow for the collection of more data. All depositions from this and the following chapters on are carried out onto a commercial CNT roving from Nanocomp Technologies Inc. (a Huntsman Company) (Miralon® lot 954738) with average cross-sectional dimensions of 30 μm × 1.53 mm (with 20 % deviation possible in

either dimension) [101], an average density of 0.12 g/cm^3 [93], and linear density of 9.24 ± 0.35 mg/m when vacuum dried. Optical and scanning electron microscopy (SEM) images of the material are presented in Figure 25. The surface clearly displays the CNT bundle structure, with no visible particles or impurities. A backscatter electron (BSE) image of the region shown in Figure 37b has very low contrast, indicating a generally homogenous atomic composition. Energy dispersive x-ray spectroscopy (EDS) presented Figure 37g shows a strong carbon signal with a smaller peaks for iron (from the residual synthesis catalyst), as well as minor sulfur, silicon, and aluminum impurity peaks. The average resistance per length (R/L) of the dried material is 354 ± 12 Ω/m. A mechanical analysis of this material can be found in previously published work [93,101].

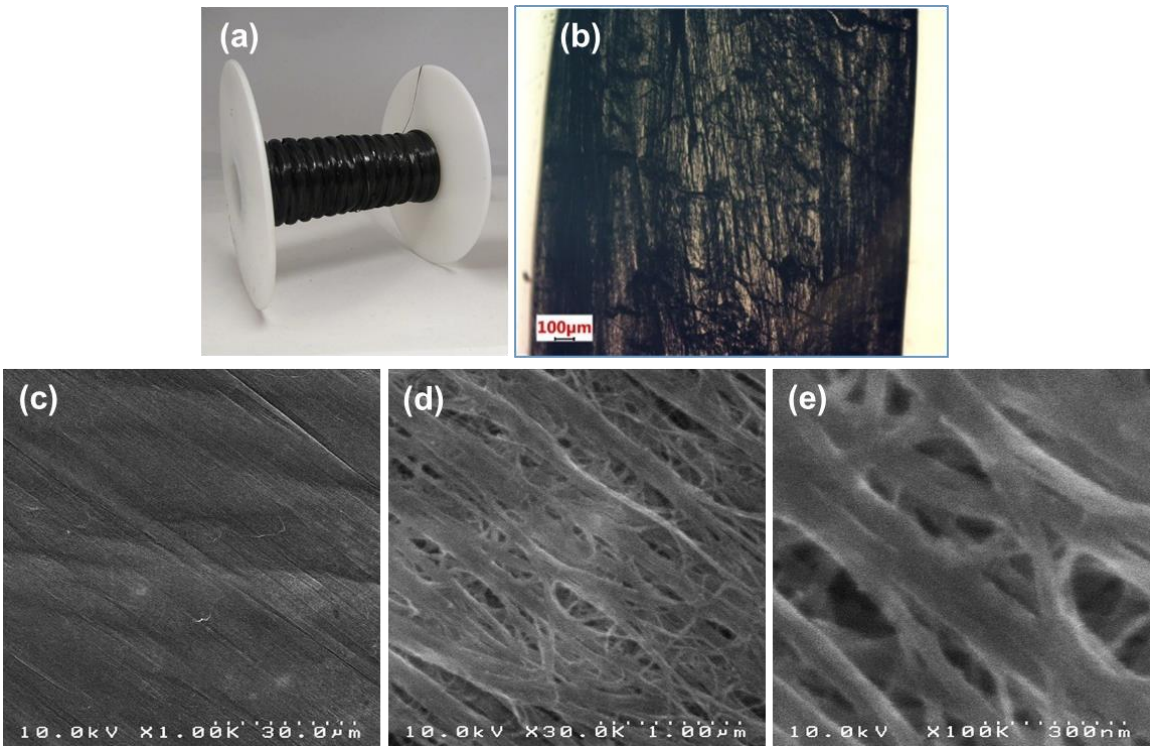

Figure 25. (a) Picture of a spool of CNT roving. (b) Optical micrograph of the CNT roving surface. SEM images of the vacuum dried CNT roving surface at (c) 1k, (d) 30k, and (e) 100k magnification.

Joule heating driven CVD was carried out in a three-neck flask, outlined in Figure 26 and described in our previous study [93]. In this setup, copper electrical leads crimped to flat copper clips are passed through rubber septa on opposite ends of the flask. Three 12 cm strands of roving are suspended in parallel between the flat copper clips. The strands of roving shared a common point of contact at the clips but otherwise hang free from one another within the flask. Under an inert argon atmosphere within a glovebox, masses of 5 mg to 100 mg precursor are added to the bottom of the flask. A hose-barb adapter with a stopcock is used to seal the center neck of the flask. After removing the flask from the glovebox the center neck is connected to a Schlenk line, which may provide either vacuum or 5 % H_2/95 % Ar (mol/mol) gas. The flask is cycled between vacuum and the reducing gas three times before pumping down to a target pressure of 166 Torr, 0.300 Torr, or 0.175 Torr. A heating mantle is used to sublimate the precursor from the bottom of the flask, and the flask is wrapped in insulating glass wool for more even heating. Precursor temperature is modified by regulating the temperature of the heating mantle to set points between 130°C to 210°C.

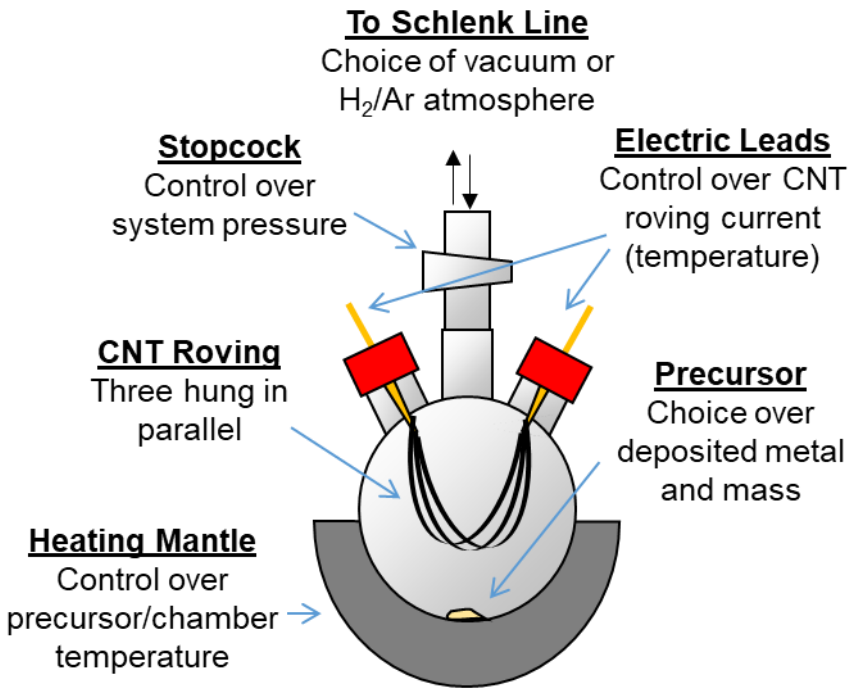

Figure 26. Diagram of the experimental setup with the various experimental parameter controls outlined. The flask is wrapped in glass wool (not shown) to produce more even heating during deposition.

As described in previous work [93], deposition is carried out through the application of current to the CNT roving to induce Joule heating. This Joule heating produces the thermal energy required to decompose the metal-organic precursor into metal on contact with the CNTs. Two variations of the deposition process are presented in this text. In the continuous filament heating CVD (CFH-CVD) process, current is applied to the CNT roving continuously throughout the entire one hour deposition process. The vapor phase precursor decomposes immediately upon contact with the hot CNT roving. In the delayed filament heating CVD (DFH-CVD) process, no electrical bias is initially applied to the CNT roving, and the vapor precursor is allowed to condense onto the cool (unheated) CNT surface for a one hour period. After the one hour condensation of the precursor, 5 % H_2/95 % Ar gas is introduced into the flask to return it

to atmospheric pressure and then current is applied for a period of five minutes to decompose the condensed metal-organic precursor. In either process, the total current applied to the three roving strands was set to values between 0.45 A to 1.2 A (between 150 mA/roving and 400 mA/roving). Thermal image of each of the currents are shown in Figure 27, acquired using a FLIR A35 IR camera with an emissivity correction of 0.825 (determined through ASTM E1933). In the parallel setup at applied currents of 400 mA/roving and above, samples of the CNT roving are not consistently stable and sometimes fail due to excessive current induced heating [102] over the deposition period.

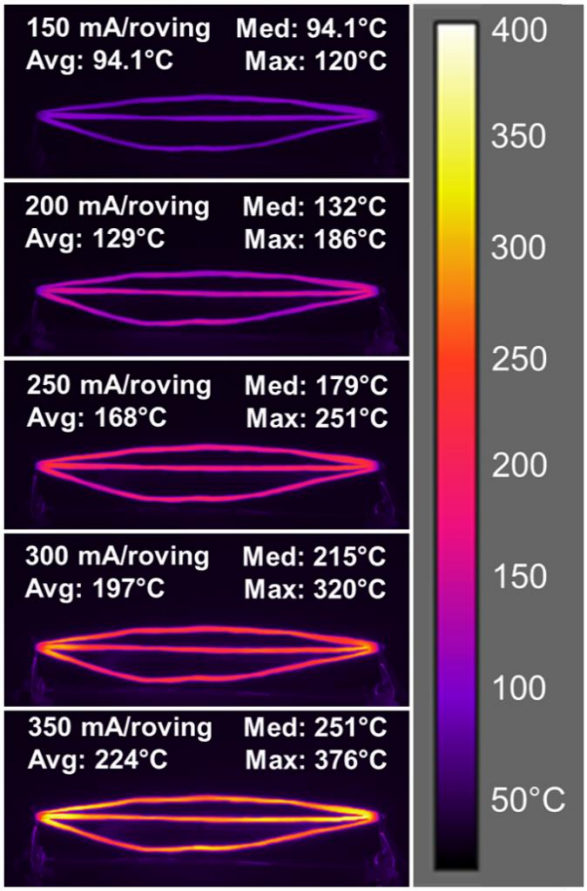

Figure 27. Thermal images of three 12 cm CNT roving suspended in parallel between two copper clips showing temperature as a function of applied current in air. The total current applied is three times the current listed per roving. The average, median, and max temperatures were calculated from the pixels with temperatures >75°C (~55°C over ambient), which were taken to be the heated CNTs.

4.3. Deposition Time

To determine whether higher seed masses may be deposited, an “active-vacuum” setup was evaluated (Figure 28). In this modification to the deposition process the vacuum line was left open in the system, instead of closed as in the previous “static-vacuum” technique. This will allow any reaction byproduct gasses to be removed from the system, thereby lowering the pressure and allowing for further vaporization and decomposition of the precursor. This “active vacuum” setup led an increase in the deposited mass to 33.38% from the previous 14.78% in the “static vacuum” setup with a one-hour deposition time from 50mg of $Cu(tBAOAC)_2$ precursor.

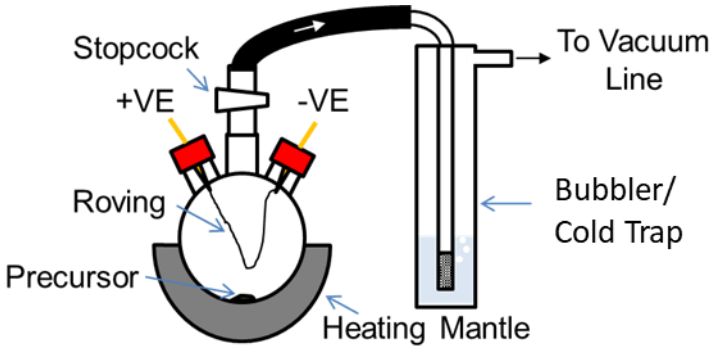

Figure 28. The active vacuum CVD setup with a bubbler or cold trap to catch decomposition byproducts prior to entering the vacuum pump.

In this setup, higher masses are also obtainable from increased deposition time, as shown in Figure 29a. Going from a one-hour deposition (Figure 29b) to a two-hour deposition (Figure 29c), the deposited nanoparticles can be seen to completely cover the surface of the CNT roving.

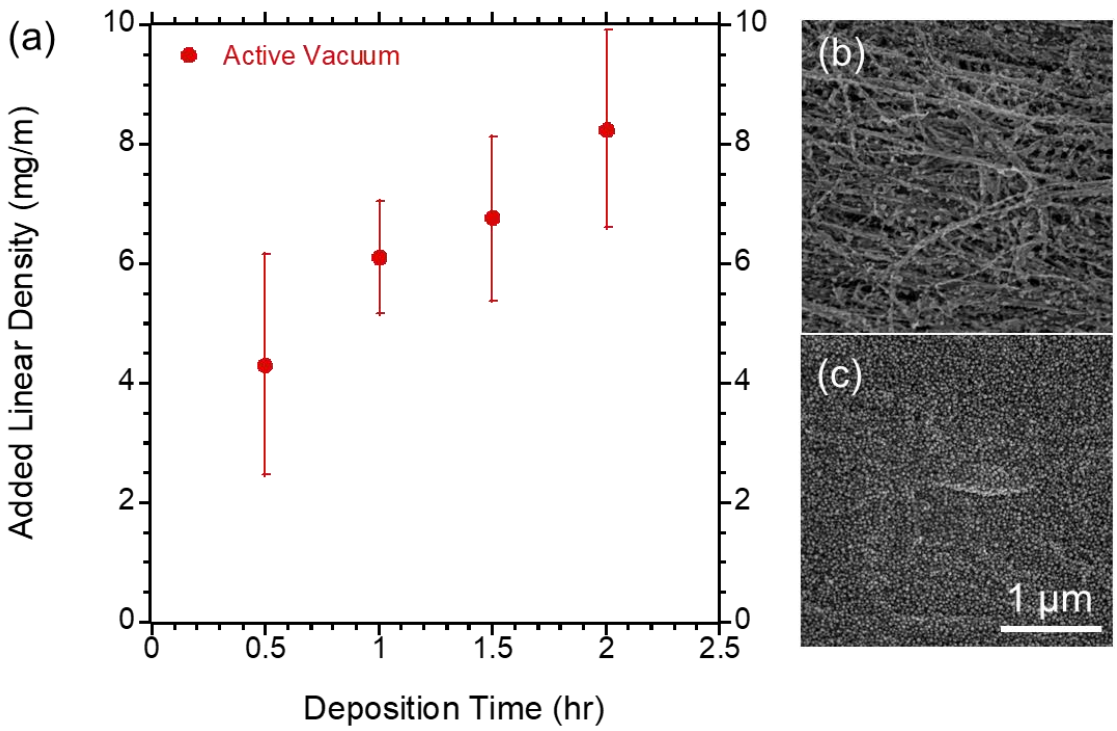

Figure 29. (a) Added mass/length from active vacuum CFH-CVD processes. Images of the depositions at time of (b) 1.0 hr and (e) 2.0 hr. The 2.0 hr deposition has completely coated the underlying roving with copper.

4.4. Precursor Temperature

While $Cu(tBAOAC)_2$ is a good choice for the seeding metal due to the small seed size deposited, it is not the only precursor available. Recent studies with a copper (II) acetylacetonate [$Cu(acac)_2$] precursor (CAS #13395-16-9, Sigma-Aldrich 99.9%) have demonstrated the ability for the precursor to deposit heavier masses than the $Cu(tBAOAC)_2$ precursor through a one-hour active vacuum CFH-CVD process. The acetylacetonate (acac) version of this precursor is utilized to produce the deposition, since the thermal decomposition of this family of precursors have been extensively studied [98,100,103]. The acetylacetonate precursors decompose at elevated temperatures with

the typical evolution of acetylacetone and related decomposition products [100], leaving behind metal films.

The impact of precursor temperature on deposited mass was investigated by systematically varying the mantle temperature from 130°C to 210°C for a deposition of 50 mg $Cu(acac)_2$ in a one hour CFH-CVD at 166 Torr with 350 mA/roving current. The percent deposited metal mass is determined by dividing the mass added from the deposition by the mass of the seeded CNT conductor after the deposition. For example, a seeded CNT conductor that doubles in mass during the deposition would be calculated to be 50 % w/w metal. Figure 30a demonstrates an increase in deposited mass with increasing precursor temperature. At 130°C, composites of approximately 20 % w/w Cu are produced, with a coating of Cu seeds visible across the surface of the roving (Figure 30c). A temperature of 130°C is the lowest value that can be reliably obtained in this CVD setup due to radiative or convective heating of the reaction vessel by the electrically biased CNTs. Representative images from depositions at 155°C (Figure 30d), 175°C (Figure 30e), and 210°C (Figure 30f) show increasingly higher densities of seeds across the surface of the hybrid conductor, eventually completely obscuring sight of the underlying CNT roving. Likewise, the depositions at 155°C, 175°C, and 210°C led to progressively heavier mass loadings of 45 % w/w, 60 % w/w, and 65 % w/w copper, respectively. Thus, the increase in precursor temperature increases the rate of sublimation and partial pressure of the precursor within the flask, allowing for higher deposited masses within the given deposition time. The deposition density begins to plateau due to exhaustion of the precursor around 200°C. Above 210°C, dark patches were observed on the bottom half of the flask from decomposition of the $Cu(acac)_2$ precursor, as expected

above that temperature [99]. Heavier surface depositions lead to a general decrease in the R/L of the samples, as shown in Figure 30b, due to the eventual coalescence of the surface particles as a film. Thus, control over precursor temperature is one mechanism that allows for control over deposited mass due to modification of precursor's vapor pressure within the reaction chamber.

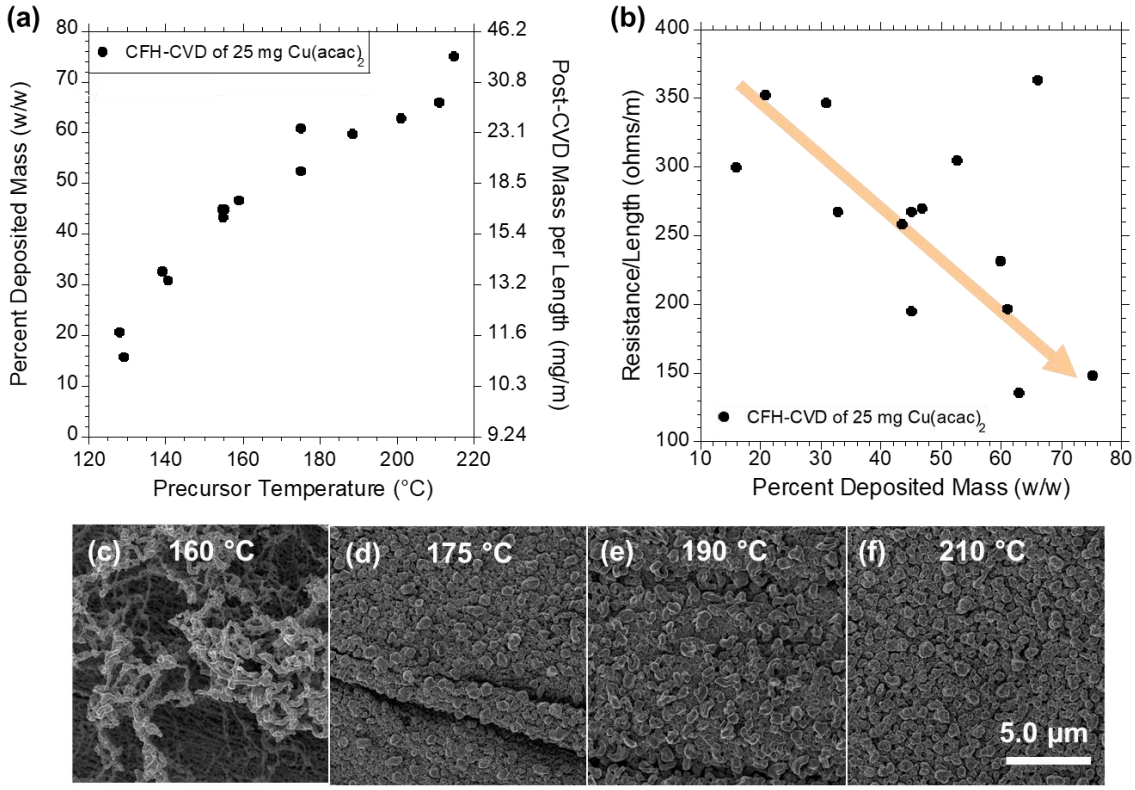

Figure 30. (a) Relationship between precursor temperature and the percent deposited seed mass for CFH-CVD of $Cu(acac)_2$, 166 Torr, 1 hour deposition with 350 mA/roving current. (b) Relationship between deposited seed mass and resistance/length of $Cu(acac)_2$ seeded roving. Secondary electron images of depositions with mantle temperatures of (c) 160°C, (d) 175°C (e) 190°C (f) 210°C. Samples prepared via a 1 hour CFH-CVD with 350 mA/roving, with 25 mg $Cu(acac)_2$ precursor.

4.5. System Pressure

Complementary to precursor temperature, the effect of the CVD system pressure onto deposited mass and nanoscale morphology is evaluated in depositions from the $Cu(acac)_2$ precursor. Decreasing the system pressure from 166 Torr to 0.300 Torr to 0.175 Torr at 200°C results in a lower density of surface particles at similar mass loading as shown in Figure 31. In contrast to samples produced at 166 Torr with heavier surface deposition, the resistance/length of the samples produced at 0.300 Torr remains nearly unchanged (380 Ω/m). Thus, lower system pressure increases the mean free path of the vapor phase precursor and its mass fraction within the gaseous phase leading to an improved infiltration of the vapor into the CNT network and subsequent deposition. Therefore, while the overall distribution of the nanometal particles is maintained at different mass loadings with modification of the precursor temperature, adjustment of the chamber pressure allows for different nanometal distributions with similar mass loadings by altering the mean free path of the vapor phase precursor through the heated CNT roving.

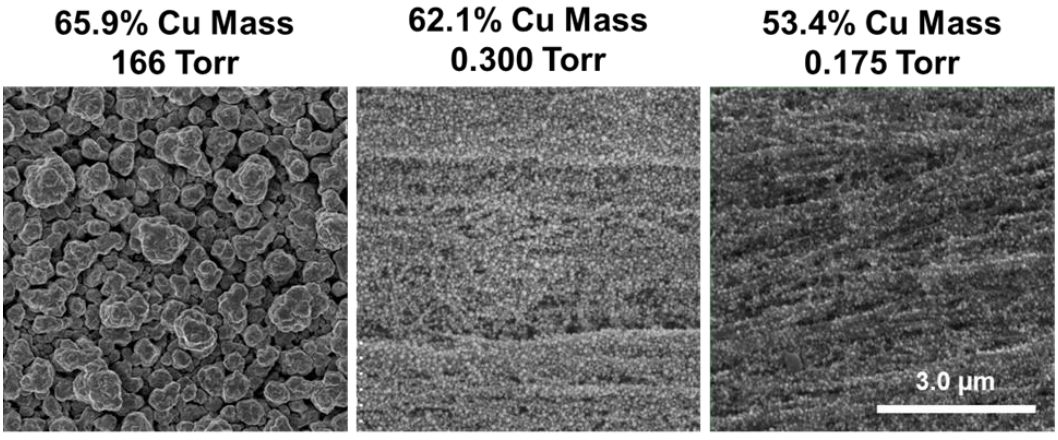

Figure 31. A comparison of the surface morphology of samples produced from a 1 hour CFH-CVD of 25 mg $Cu(acac)_2$ at 200°C with 350 mA/roving at the indicated pressures. The samples exhibit similar deposited masses but differing concentrations of particles on the surface.

4.6. Precursor Mass

The effects of precursor mass on deposited mass were investigated using similar deposition conditions of a one hour CFH-CVD of various masses of $Cu(acac)_2$ at 200°C on three roving in parallel at 350 mA/roving current at 0.300 Torr. Depositions were carried out with 5 mg, 10 mg, 25 mg, 40 mg, and 50 mg of $Cu(acac)_2$. Under the given precursor temperature and pressure, the entire amount of precursor was sublimated from the bottom of the flask, meaning that the amount of metal that can be deposited from the vapor should be proportional to the precursor mass. As expected, the results demonstrate increasing deposited mass with increasing precursor mass, as shown in Figure 32a. Secondary electron images show that the spherical particle morphology is preserved up to 50 mg, with sparse particles at the lighter depositions from 5 mg (Figure 32b) and 10 mg $Cu(acac)_2$ (Figure 33e) and higher densities of surface particles from the heavier depositions at 25 mg (Figure 32c) and 50 mg $Cu(acac)_2$ (Figure 32d). In the 100 mg $Cu(acac)_2$ deposition, Figure 32e shows that the seeds have begun to coalesce into larger particles on the surface. From CFH-CVD of 25 mg $Cu(acac)_2$ and lower masses, none of the samples exhibited decreases in R/L. The average change in R/L for the lighter precursor mass depositions was 10.8 ± 5.1 %. With CFH-CVD of 40 mg $Cu(acac)_2$ and heavier masses, certain samples from each deposition exhibited decreases in R/L. The heavier 40 mg to 100 mg depositions led to an average change in R/L was 4.37 ± 9.51 %. One sample from each the 40 mg and 50 mg depositions had heavy enough coatings to experience decreases in their R/L by 7.85 % and 7.66 %, respectively. Two depositions from the 100 mg deposition exhibited decreases in R/L of 4.88% and 4.24%. This indicates that deposited masses of greater than 65 % w/w copper (as in the 40 mg

deposition) approach the critical particle densities required to see improvements to R/L under the presented deposition conditions. Overall, by modifying the precursor mass, the depositions can be tuned from sparse deposition at around 10 % w/w to thicker coatings of 85 % w/w.

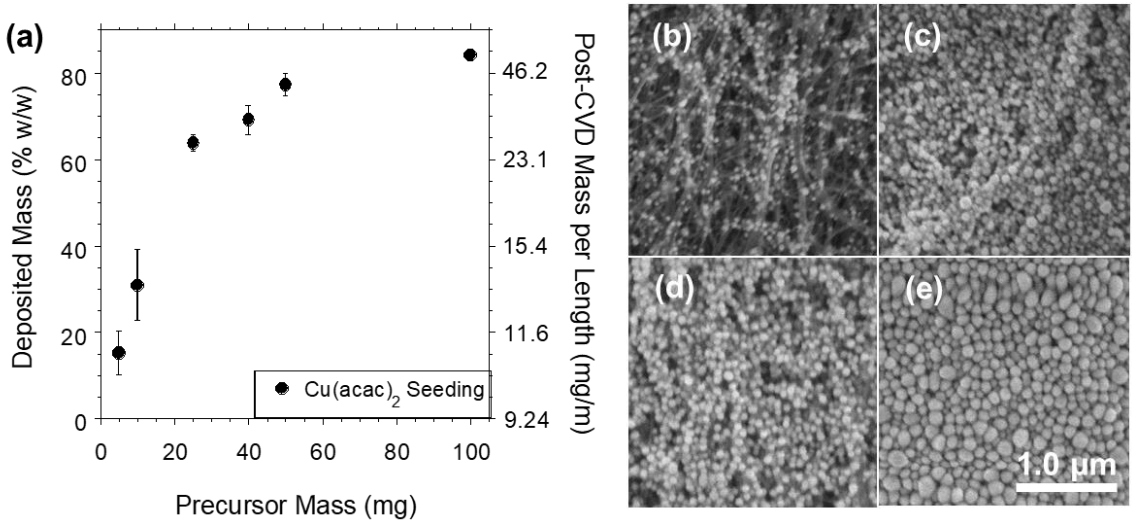

Figure 32. (a) Deposited mass from a 1 hour CFH-CVD of various masses of $Cu(acac)_2$ at 200°C on three roving in parallel at 350 mA/roving current at 0.300 Torr. Deposited particle morphology from (b) 5 mg $Cu(acac)_2$, (c) 25 mg $Cu(acac)_2$, (d) 50 mg $Cu(acac)_2$, and (e) 100 mg $Cu(acac)_2$.

4.7. Amount of Applied Current

In the study of applied deposition currents, conditions were constant with one hour CFH-CVD using 10 mg $Cu(acac)_2$ precursor at 200°C and 0.300 Torr with three CNT roving in parallel. Increases in mass, indicating depositions from each of the precursors, are observed at all currents from 200 mA to 350 mA, as shown in Figure 33a. This indicates temperatures in excess of the 225–250°C required for decomposition of the metal-organic precursor is reached [99]. Across the entire 200–350 mA/roving current range, the deposited masses from copper were relatively invariant between 20–30 % w/w.

The SEM results for the $Cu(acac)_2$ depositions given in Figure 33b-e show spherical copper particles at all applied roving currents, indicative of the limited interaction between the deposited copper and the CNT roving. Previous work demonstrated that at lower currents, only certain localized hot-spots reach temperatures sufficient for deposition [93]. The invariance of the copper mass and particle morphology could be attributed to its limited physical and electrical interaction with the CNT substrate. Since the copper forms disconnected spheres at a relatively low density on the CNT roving network, it is expected that such hot-spots remain hot, leading to continual deposition from the $Cu(acac)_2$ precursor. In fact, the resistance measured from the two electrical leads during the depositions was only seen to decrease by an average of 2.5 % for the $Cu(acac)_2$ CFH-CVD. Consequently, while at lower currents there may be a higher proportion of the total copper deposited at the high temperature hot-spot locations (i.e. a site-specific deposition [93]), the total mass of deposited copper does not change. Thus, while it is possible for copper to be able to deposit site-specifically at higher temperature locations as shown in the previous work [93], heavier precursor masses and metal depositions are required to interconnect the CNT roving substrate.

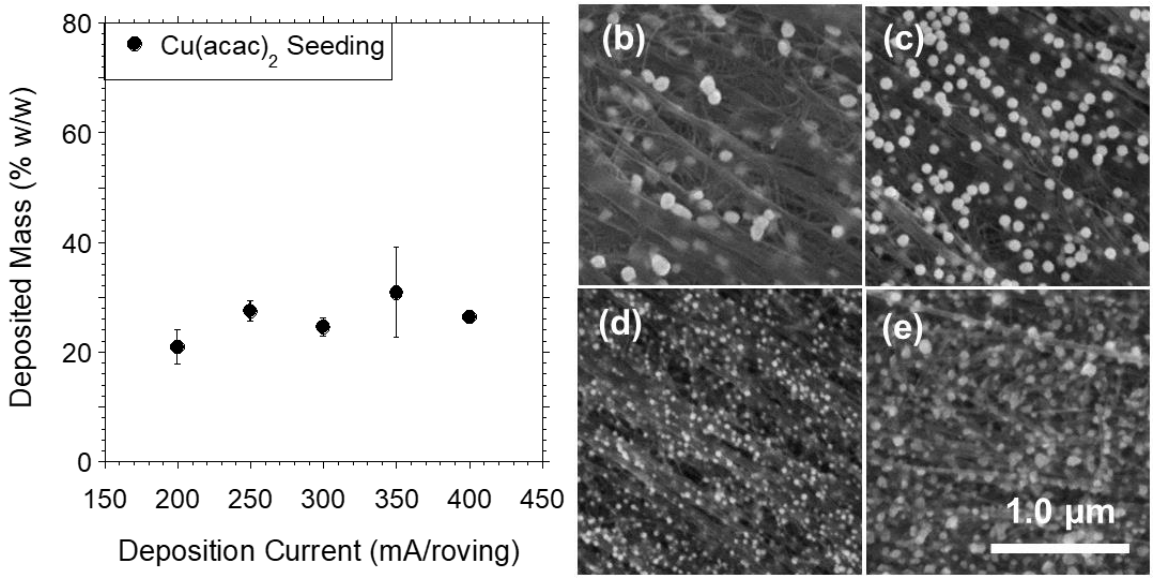

Figure 33. (a) Deposited mass from a 1 hour CFH-CVD of 10 mg of $Cu(acac)_2$ at 200°C on three roving in parallel at the indicated currents at 0.300 Torr. Deposited particle morphology from (b) 200 mA/roving, (b) 250 mA/roving, (c) 300 mA/roving, and (d) 350 mA/roving.

4.8. Interval of Applied Current

In the initial study with $Cu(tBAOAC)_2$ at 150°C and 166 Torr, modifying the interval of the applied current by transitioning from continuous application of current (CFH-CVD) to delayed application of current (DFH-CVD) led to slightly higher deposited masses [93]. This was thought to be a result of the incomplete sublimation of the $Cu(tBAOAC)_2$ precursor due to a low vapor pressure. With the $Cu(acac)_2$ precursor, complete sublimation is obtained at a mantle temperature of 200°C. Thus, while the CFH-CVD of 25 mg precursor described in Figure 32 leads to deposited masses of 63.7 ± 1.9 % w/w, DFH-CVD leads to lower deposited masses since only the precursor that has condensed on the surface of the roving is available for decomposition to metal. At 166 Torr, shown in Figure 34a+b, the DFH-CVD leads to deposited masses of 17.1 ± 2.0 % w/w. The masses deposited at 0.300 Torr, shown in in Figure 34c+d, are even lower at 3.6 ± 0.6 % w/w. The lower mass at lower pressure is attributed to a higher

proportion of the precursor remaining in the vapor phase during the decomposition. If the deposited mass is taken to be pure metal, the efficiency of the depositions can be calculated. The $Cu(acac)_2$ precursor contains 24.3 % w/w copper. Thus, a total of mass of 6.075 mg of copper is available from 25 mg of $Cu(acac)_2$. From the deposited masses at 0.300 Torr during CFH-CVD, this equates to a deposition efficiency of 93.0%. The DFH-CVD depositions at 166 Torr and 0.300 Torr had deposition efficiencies of 11.7% and 2.1%, respectively. The remainder of the precursor likely either condensed on the walls of the flask, or been removed through the vacuum pump prior to the application of current through the CNTs. Thus, the CFH-CVD makes more efficient utilization of the available precursor mass than the DFH-CVD approach, while the latter proves useful for producing lightweight depositions.

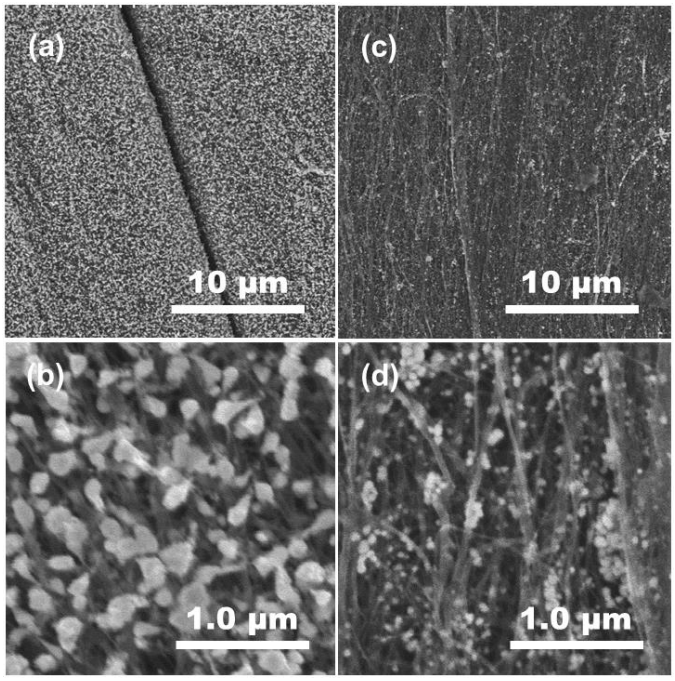

Figure 34. Secondary electron images of 1 hour depositions of 25 mg of $Cu(acac)_2$ at 200°C with 350 mA/roving (a,b) DFH-CVD at 166 Torr, (c,d) DFH-CVD at 0.300 Torr.

One final option for the application of current that bears mention is the use of a pulsed-filament heating CVD (PFH-CVD) process. In this process, the applied heating current is pulsed or modulated throughout the run. This could help to improve both the uniformity of deposition infiltration as well as the site-selectivity towards hot spots. The EDS map of the depositions from $Cu(tBAOAC)_2$ shown in Figure 13a indicated that the density of copper particles is heavier towards the surface of the CNT roving. As the precursor will either decompose upon the first surface that is sufficiently hot or condense upon a surface that is sufficiently cool, the degree of vapor infiltration is likely a factor of the mean free path of the vapor particles. Thus, as shown in Figure 31, lowering the pressure is one method to decrease the density of particles that decompose on the surface before infiltrating into the roving. However, a second option is to heat the roving to a temperature at which the precursor will stay in the vapor phase without condensing or decomposing. Then once the precursor has fully infiltrated the CNT network, periodic pulses of a higher current may be applied to decompose the precursor. In addition, while site selectivity was achieved on a macro- to micro- scale from depositions of $Cu(tBAOAC)_2$, ultimately the best utilization of seed mass would be from deposition at junctions between individual CNTs and between bundles of CNTs. The use of a current pulse to heat the roving could also allow for improved localization of the heating. In an initial study into the effect of current modulation on heat localization, a triangular notch was cut halfway through a strand of roving to create a hot spot defect in the strand. A pulsed current was then applied to the roving, and the resultant heating was measured in air using a FLIR A35 thermal camera. Current pulses with lengths of 20 ms, 100 ms, 500 ms, and 990 ms were applied at 1Hz frequency. As can be seen in Figure 35, the hottest

point in the roving is centered on the defect, particularly in the shorter pulses. However, as the pulse length increases to 500 ms, the peak spread of the heat across the roving increases until the entire roving is hot. Thus, short pulses of current may represent one path towards more efficient utilization of deposited metal mass.

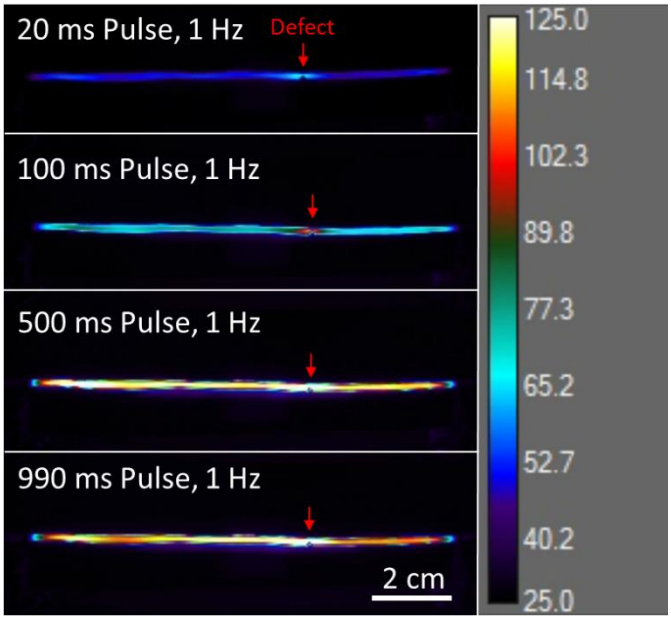

Figure 35. Spread of peak heating across roving for (a) 20ms, (b) 100ms, (c) 500ms, and (d) 990ms pulses with a 1 Hz pulse frequency.

4.9. Conclusions

The effects of the modification of various CVD parameters on the deposited particle mass and morphology have been investigated. With appropriate choice of precursor temperature and pressure, increased deposition times can lead to heavier deposited seed masses. Higher temperatures and lower pressures lead to faster sublimation rates, allowing for faster depositions and more efficient utilization of the precursor mass. Lower pressures also allow for increased infiltration of the vapor precursor. Increasing the available precursor mass provides for a direct method of

increasing deposited masses. Finally, the effects of the amount and interval off applied current allow for control over the site-selectivity or uniformity of the resultant depositions.

CHAPTER 5: DEPOSITIONS OF VARIOUS SEEDING METALS

5.1. Theory and Initial Studies

The work described to this point has focused on copper seeds to form the nanometal interconnects in the Cu-CNT hybrids. Copper seeds have the primary advantage of high conductivity. However, the high contact angle of spherical copper seed particles indicates limited physical and electrical interaction between the metal and CNTs, a phenomenon that has been frequently identified in the literature [55,62,77,96,104–106]. Attempts to improve electrical transport across the copper-CNT interface typically involve the use of functionalization of the CNT surface [55,62,65,79], or the use of an interfacial metal [55,62,66,77,107]. In the latter case, the ideal choice for the interfacial metal deposited through the CVD technique would result in seeds that act both as anchor points for the electroplating of copper and as electrical interconnection sites in their own right. Many metal-organic precursors are available making it possible to use the technique to deposit a wide variety of metals with little to no change in deposition conditions. Computational studies have indicated that metals like titanium, platinum, and palladium should have improved contact resistance [108] and stronger binding energies [109,110] with CNTs compared to copper and other common electrical conductors like gold. Additionally, metals such as titanium [111,112], nickel [55,112], platinum [113,114], and palladium [81,112,115,116] are observed to adhere or bond to CNTs.

Others such as chromium [77], ruthenium [117,118], iron [106], and molybdenum [119] are known to form metal carbides. In some instances, multi-walled CNTs are observed to have a layer of amorphous carbon on their surface [78]. This layer may be energetically favored to form conductive carbides with the aforementioned metals [77]. Improved contact and conduction between the metals and CNTs should allow for an overall more conductive hybrid [62]. A previous study of a titanium adhesion layer deposited through thermal evaporation demonstrated that such metal adhesion layers can also improve the temperature stability of a copper overcoat [101]. Additionally, previous literature demonstrated that platinum and palladium seem to interface well with bulk CNT wires, allowing for the maintenance of a low TCR with improved conductivity in metal plated CNT wires [60]. However, there have not been investigations into the use of platinum, palladium, and related metals as interfacial or seeding layers for copper-CNT composites. The precursors utilized in this and the following chapters are copper (II) acetylacetonate (CAS #13395-16-9, Sigma-Aldrich 99.9%), platinum (II) acetylacetonate (CAS #15170-57-7, STREM 98%), nickel (II) acetylacetonate (CAS #3262-82-2, Sigma-Aldrich 95%), palladium (II) acetylacetonate (CAS #14024-61-4, STREM 99%), ruthenium (III) acetylacetonate (CAS #14284-93-6, STREM 99%), rhodium (III) acetylacetonate (CAS #14284-92-5, STREM 97+%), iridium (III) acetylacetonate (CAS # 15635-87-7, Alfa Aesar Ir 37.5% min), silver (I) acetylacetonate (CAS #15525-64-1, Alfa Aesar 98%), bis(2,2,6,6-tetramethyl-3,5-heptanedionato) copper (II) (CAS#14040-05-2, STREM 99%), tris(2,2,6,6-tetramethyl-3,5-heptanedionato) cobalt (III) (CAS#14877-41-9, STREM 99%), tris(2,2,6,6-tetramethyl-3,5-heptanedionato)

chromium (III) (CAS#14434-47-0, STREM 99%), and bis(cyclopentadienyl)tungsten(IV) dihydride (CAS#1271-33-6, Sigma Aldrich 97%).

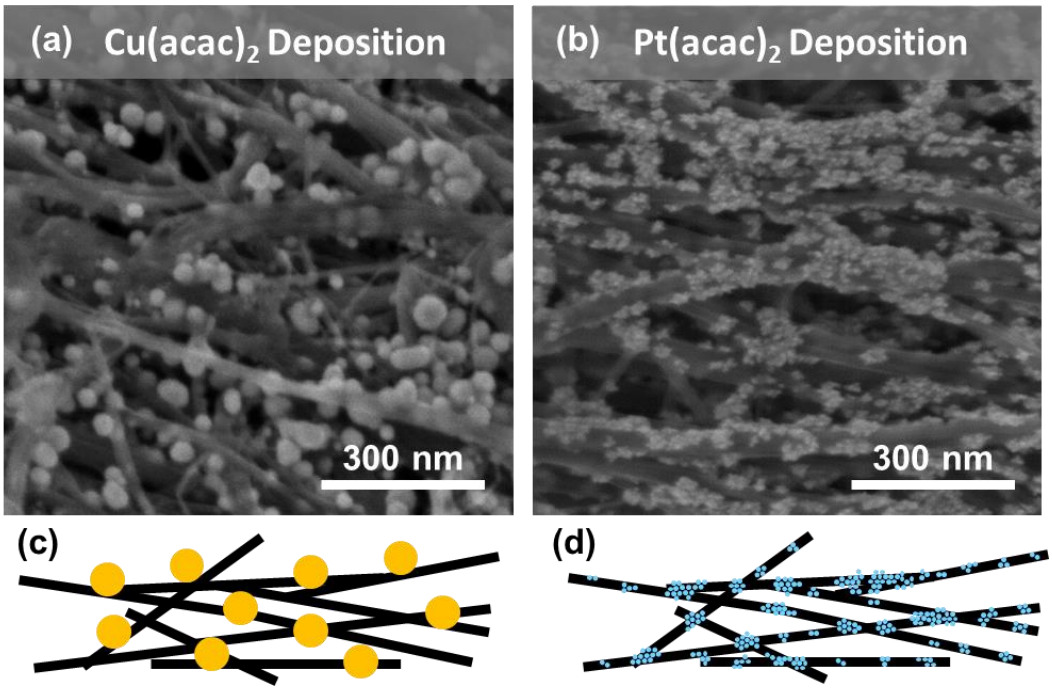

Figure 36. (a) 1 hour DFH-CVD with 350 mA/roving, 25 mg $Cu(acac)_2$ precursor, 166 Torr. (b) Illustration of a loosely bound seeding type deposition, as from the $Cu(acac)_2$ precursor. (c) 1 hour DFH-CVD with 350 mA/roving, 25 mg $Pt(acac)_2$ precursor, 166 Torr. (d) Illustration of a more tightly bound seeding type deposition, as from the $Pt(acac)_2$ precursor.

In a prototypical study to investigate alternative seeding metals, copper and platinum were deposited from 25 mg of their respective acetylacetonate forms in a one hour DFH-CVD at 166 Torr with an applied current of 350 mA/roving and a mantle temperature of 200°C, similar to previous work [93]. $Cu(acac)_2$ and $Pt(acac)_2$ in particular have both been observed to decompose in the range of 225–250°C [99,103]. Under scanning electron microscopy (SEM), shown in Figure 36a, the deposition from $Cu(acac)_2$ exhibits the spherical particle morphology expected of copper seeds on the

CNT roving. Figure 37b shows higher atomic number regions coincident with the spherical particles under BSE imaging that, combined with the emergence of a copper peak in EDS shown in Figure 37e, confirms that these particles are deposited copper seeds. The high contact angles of these spherical copper particles indicate limited adhesion and interaction with the CNT roving, represented in Figure 36b, in line with the previously reported results [93]. In contrast, the prototypical deposition from platinum (II) acetylacetonate $Pt(acac)_2$, shown in Figure 36c, led to tightly bound platinum clusters on the CNT roving substrate. As with the copper seeds, BSE imaging in Figure 37d and EDS data in Figure 37e confirm that the smaller clusters are platinum. Compared to the copper particles with average diameters of ~40 nm, the platinum nodules within each cluster formed by the $Pt(acac)_2$ deposition had nearly an order of magnitude smaller diameter of ~5 nm, represented in Figure 36d. The lack of Ostwald ripening and coalescence in the platinum seeds is likely a result of a more energetically favorable interaction with the CNT roving surface as well as the higher melting point of platinum (1,768°C) compared to copper (1,085°C). The smaller, more closely bound clusters of platinum should act as a much more effective interconnection and seed metal that the large, discrete copper particles.

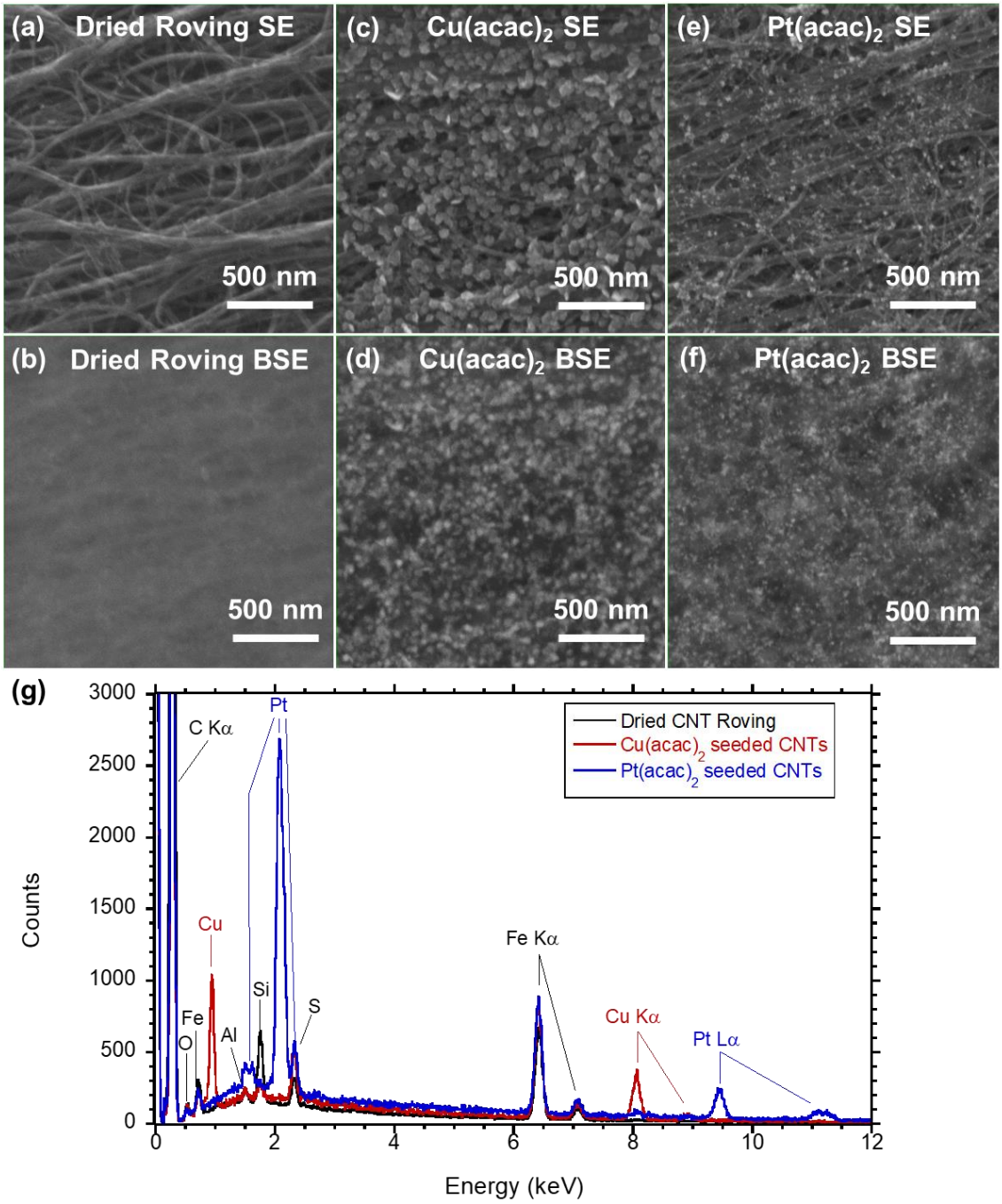

Figure 37. (a) SE and (b) BSE images of CNT roving after vacuum drying. SEM images after a one hour DFH-CVD of 25 mg precursor at 166 Torr with an applied current of 350 mA/roving and a mantle temperature of 200°C. (c) SE and (d) BSE of $Cu(acac)_2$. (e) SE and (f) BSE of $Pt(acac)_2$. (g) EDS spectra of the dried CNT roving and the above regions.

Even without substantial improvement to the contact resistance, the smaller particle size of platinum (and related metals) may allow for mass savings in a hybrid

conductor. This is despite platinum's much higher density (21.45 g/cm^3) compared to copper (8.96 g/cm^3). Suppose that a conductor with the true cross section A_{cond} based on its skeletal density consists of x uniform cylindrical bundles of CNTs. The radius of each CNT bundle is then:

$$r_{bundle} = \sqrt{\frac{A_{cond}}{x * \pi}}$$

Suppose there is a critical density of surface coverage (β) required for proper interconnection or seeding proportional to r_{bundle}. If the metal nanoparticles of diameter d_{np} anneal without ripening to form a coating of the same thickness (d_{np}) over the cylindrical bundle, then the cross sectional area of the metal nanoparticles (A_{np}) required to interconnect a given bundle is:

$$A_{np} = \beta\pi\left[\left(r_{bundle} + d_{np}\right)^2 - r_{bundle}^2\right] = \beta\left[\pi * \left(\sqrt{\frac{A_{cond}}{x * \pi}} + d_{np}\right)^2 - \left(\frac{A_{cond}}{x}\right)\right]$$

The linear mass density (mass per length) of the metal nanoparticle interconnect is then the density of the coating ρ_{np} times the cross sectional area:

$$\frac{m_{np}}{l} = \rho_{np} * A_{np}$$

For a conductor of length l, the ratio of the mass of platinum compared to copper required for interconnection is:

$$\frac{m_{Pt}}{m_{Cu}} = \frac{\rho_{Pt}[(r_{bundle} + d_{Pt})^2 - r_{bundle}^2]}{\rho_{Cu}[(r_{bundle} + d_{Cu})^2 - r_{bundle}^2]} = \frac{\rho_{Pt}[d_{Pt}^2 - 2 * d_{Pt} * r_{bundle}]}{\rho_{Cu}[d_{Cu}^2 - 2 * d_{Cu} * r_{bundle}]}$$

Substituting in the diameter of the particles from Figure 36 and the densities of platinum and copper:

$$\frac{m_{Pt}}{m_{Cu}} = \frac{2.394[25\text{nm}^2 - 10\text{nm} * r_{bundle}]}{[1600\text{nm}^2 - 80\text{nm} * r_{bundle}]}$$

From the above equation, the greatest improvements are seen with smaller bundle sizes. However, the mass of platinum required for interconnection with 5 nm seeds would never be greater than that of the 40 nm Cu seeds. Even approaching the limit as $r_{bundle} \rightarrow \infty$, the mass of platinum is only 29.9 % of the mass of copper required for interconnection. Thus, even metals that are denser than copper or that have similar binding energies may be able to produce more lightweight conductors if they are able to deposit more tightly bound particles or coatings to the CNT bundles.

This chapter presents a survey of a number of metals seed depositions for comparison to the standard copper seed depositions. Nickel, ruthenium, rhodium, palladium, silver, iridium, and platinum are all available as acetylacetonates, allowing for direct comparison to the depositions from copper acetylacetonate. A related ligand, 2,2,6,6-tetramethyl-3,5-heptanedionate (TMHD) is available for chromium and cobalt depositions. The TMHD ligand adds three methyl groups to the terminal carbons of the acetylacetonate ligand. Finally, some metals such as tungsten are not available in either of the above forms. In this chapter, bis(cyclopentadienyl) tungsten (IV) dihydride [$WH_2(cpy)_2$] is utilized due its lack of oxygen functionalities and relative safety compared to carbonyl and halogenated precursors.

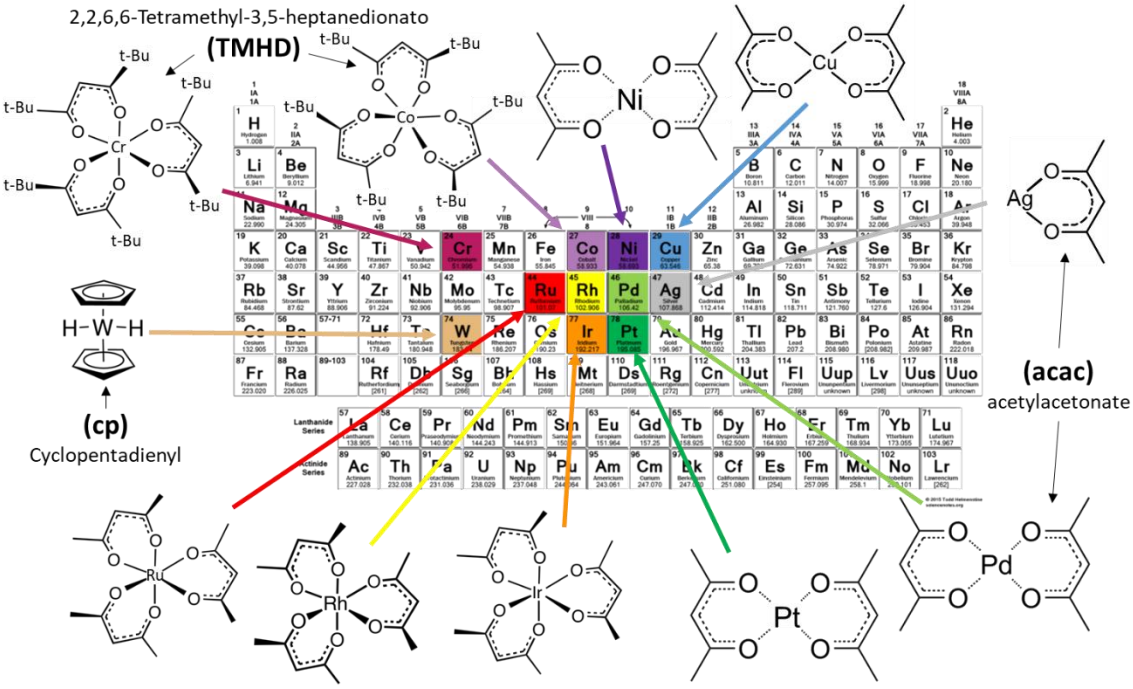

Figure 38. An illustration of the various metals and precursors surveyed in this chapter.

5.2. Acetylacetoantes of the Platinum Group Metals and Nickel

To demonstrate the versatility of the Joule heating driven CVD technique and provide a thorough comparison to copper and platinum, other periodic group 10 (Ni, Pd) and platinum group (Pd, Ru, Rh, Ir) metals are deposited. For each metal, a lighter (from 5 mg precursor) and heavier (from 25 mg precursor) CFH-CVD are carried out with three roving in parallel electrically biased to 350 mA/roving with a 200°C mantle temperature at 0.300 Torr pressure. Along with the results from platinum shown previously in Figure 37d, the EDS results in Figure 39 demonstrate the advent of the corresponding metal peaks from each deposition, indicating that the depositions were successful.

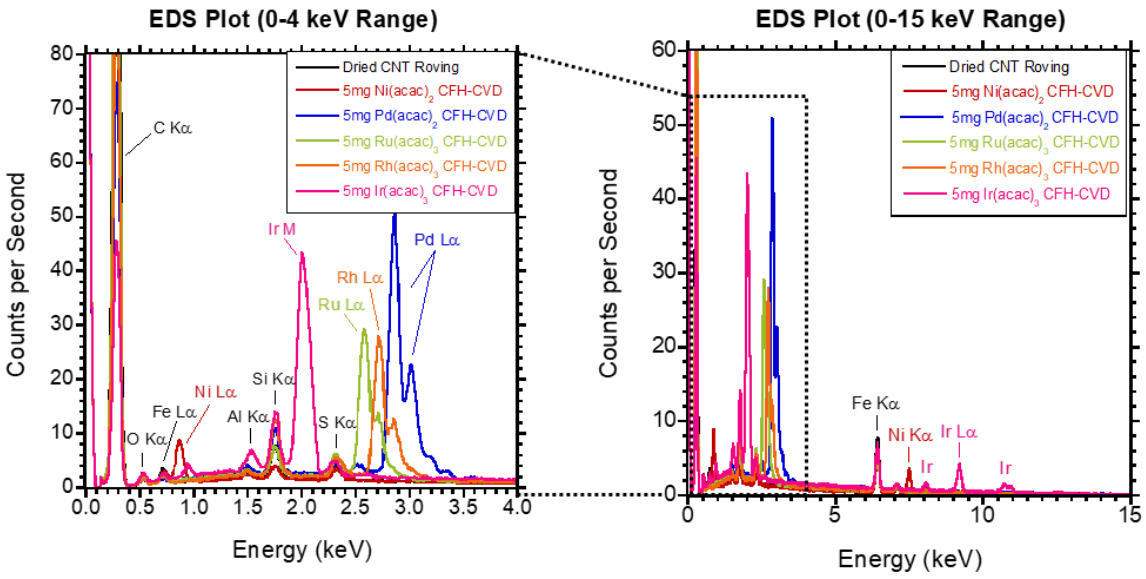

Figure 39. The EDS spectra from one hour CFH-CVD of 5 mg precursor at 200°C with three roving in parallel at 350 mA/roving. Precursors used for the depositions presented in this chart are $Ni(acac)_2$, $Pd(acac)_2$, $Ru(acac)_3$, $Rh(acac)_3$, and $Ir(acac)_3$. In each spectrum, the new peaks correlate only with the metal deposited.

Secondary electon images of each deposition are presented in Figure 40 and Figure 41. BSE images for each of these precursors and an additional magnification and are available in Figure 43 at the end of the section. The 5 mg $Ni(acac)_2$ deposition produces irregular nodules along the surface of the roving at 30.2 ± 8.9 % w/w, shown in Figure 40a. The deposition transitions to an uneven nodular coating over the entire CNT roving surface at 68.0 ± 8.5 % w/w from 25 mg $Ni(acac)_2$, shown in Figure 40b. The irregularity of these large nodules and their inconsistent contrast in BSE imaging could indicate carbon contamination from the precursor in the deposited nickel, a phenomenon which has been observed in water-free depositions from $Ni(acac)_2$ [120]. Figure 40c demonstrates that the 5 mg $Pd(acac)_2$ deposition produces a very rough, although consistent coating over the CNT roving surface at 27.3 ± 4.1 %. With the heavier 25 mg $Pd(acac)_2$ deposition shown in Figure 40d, the rough coating begins to fill in the gaps

between the CNT bundles with an increase in deposited mass to 61.3 ± 0.9 %. Figure 40e shows that CFH-CVD of 5 mg $Pt(acac)_2$ results in discrete regions of deposited nanoparticles, similar to the DFH-CVD shown in Figure 36c. The deposited mass is 35.3 ± 5.7 % w/w. Increasing the precursor mass to 25 mg $Pt(acac)_2$ results in platinum coatings of 69.5 ± 5.0 % w/w that uniformly cover the surface of the CNTs, shown in Figure 40f. Overall, a decrease in the particles size, and increase in the degree of conformity to the CNT surface is noted going down period 10 from nickel to platinum.

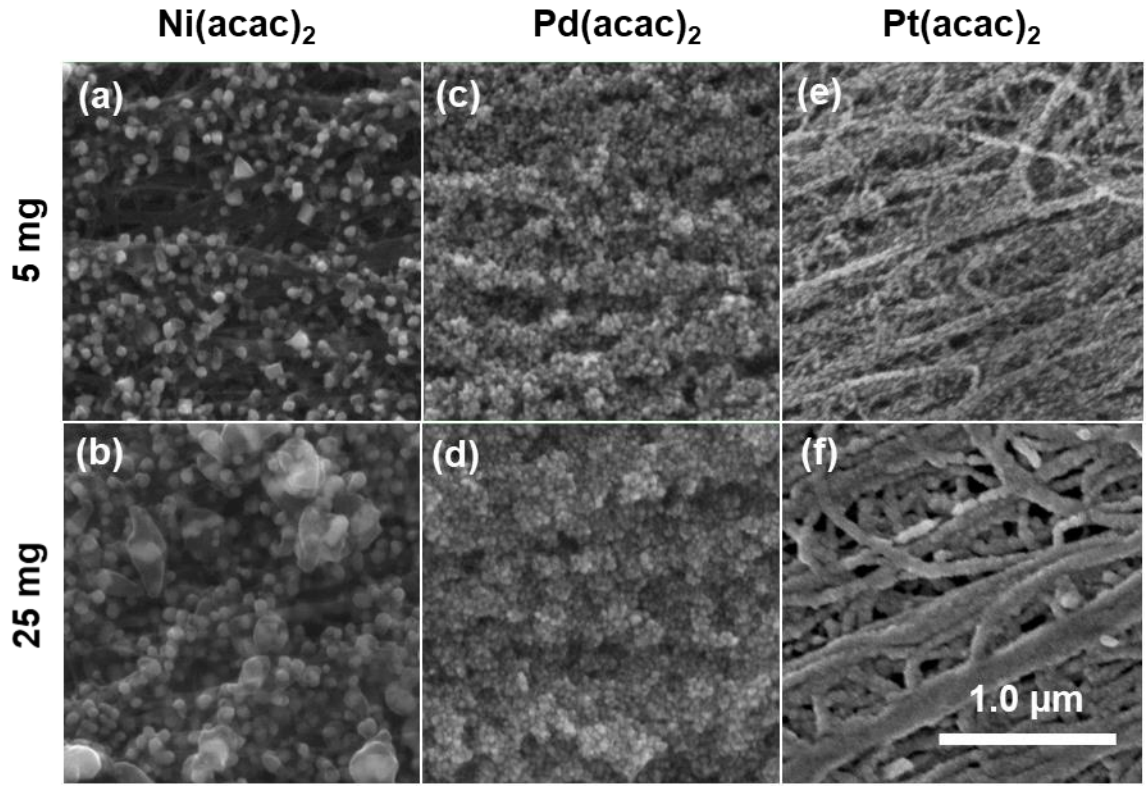

Figure 40. Secondary electron images for one hour CFH-CVD with a precursor temperature of 200°C with three roving in parallel at 350 mA/roving at 0.300 Torr for (a) 5 mg $Ni(acac)_2$, (b) 25 mg $Ni(acac)_2$, (c) 5 mg $Pd(acac)_2$, (d) 25 mg $Pd(acac)_2$, (e) 5 mg $Pt(acac)_2$, (f) 25 mg $Pt(acac)_2$.

From CFH-CVD of 5 mg $Ru(acac)_3$, clusters and small nodules are visible in Figure 41a at 10.5 ± 2.9 % w/w. The 25 mg $Ru(acac)_3$ deposition produces a mass

loading of 32.9 ± 2.5 % w/w, with the particles transitioning to a tight, irregular coating shown in Figure 41b. The $Rh(acac)_3$ deposited small nanoparticles from 5 mg of precursor, as shown in Figure 41c, transitioning to uniform coatings from 25 mg of precursor, as shown in Figure 41d. The deposited masses from the 5 mg and 25 mg $Rh(acac)_3$ depositions were 13.3 ± 3.0 % w/w and 57.0 ± 5.1 % w/w, respectively. CFH-CVD of 5 mg $Ir(acac)_3$, shown in Figure 41e, produced a mixture of nodules and an irregular coating at 17.6 ± 4.3 % w/w. The 25 mg $Ir(acac)_3$ deposition produced a uniform coating of variable thickness with a deposited mass of 63.8 ± 3.2 % w/w, as can be seen in Figure 41f. Each of the remaining platinum group precursors produced deposited smoother deposited particle morphologies closer to that of platinum than nickel or palladium.

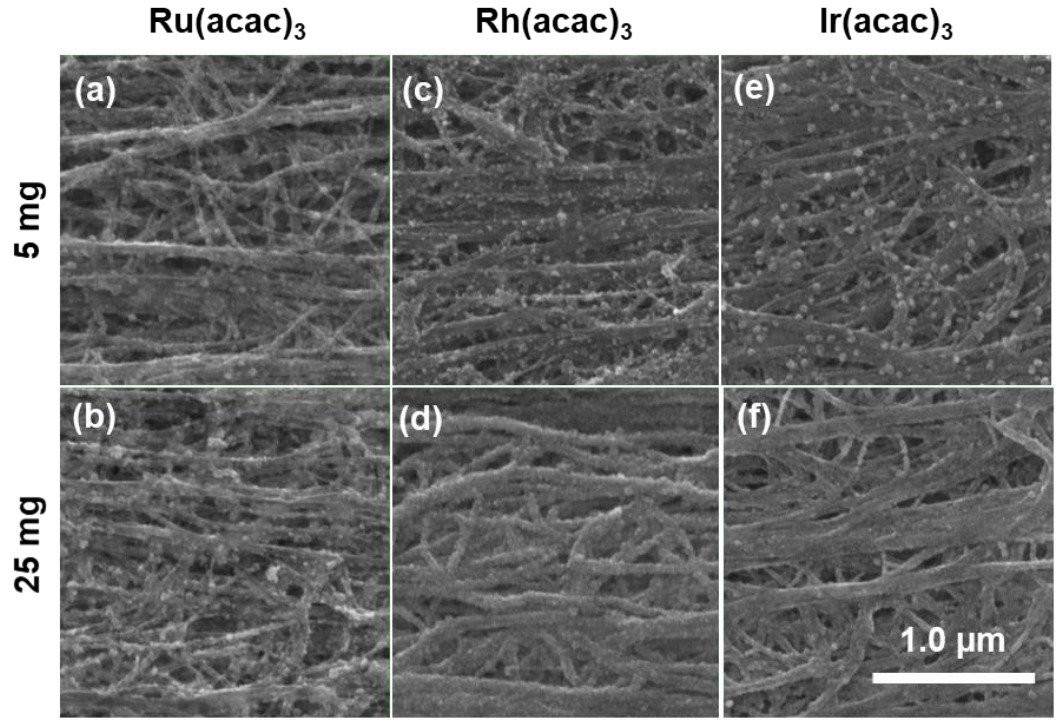

Figure 41. Secondary electron images for one hour CFH-CVD with a precursor temperature of 200°C with three roving in parallel at 350 mA/roving at 0.300 Torr for (a) 5 mg $Ru(acac)_3$, (b) 25 mg $Ru(acac)_3$, (c) 5 mg $Rh(acac)_3$, (d) 25 mg $Rh(acac)_3$, (e) 5 mg $Ir(acac)_3$, (f) 25 mg $Ir(acac)_3$.

The electrical performance of the conductors is summarized in Figure 42. Nickel produced similar increases in R/L to copper. The 25 mg $Ni(acac)_2$ deposition lead to a greater increase in R/L of 13.2 ± 5.9 % than the 5 mg $Ni(acac)_2$ deposition's increase of 8.9 ± 4.4 %. Palladium, ruthenium, rhodium, and iridium all exhibited lower R/L at higher mass loadings than at low mass loadings. This may indicate a critical particle density necessary for improvements in conductivity to become apparent. Palladium's resultant increases in R/L were second highest after the nickel, with an increase of 7.1 ± 3.6 % from 5 mg and 4.8 ± 0.3 % from 25 mg $Pd(acac)_2$. Rhodium's performance was comparable to the nickel and palladium from 5 mg precursor, with an R/L increase of 8.2 ± 4.4 %. There was a neutral effect on the R/L from 25 mg $Rh(acac)_3$, with a change of 0.3 ± 0.9 %. Ruthenium exhibited an increase in R/L of 3.3 ± 0.3 % from 5 mg, but a decrease in R/L of 5.2 ± 3.1 % from 25 mg precursor. Platinum interestingly exhibits larger decreases in R/L from the lower 5 mg deposition of 20.1 ± 18.9 % than the 25 mg deposition's decrease in R/L of 15.0 ± 4.9 %. However, the 5 mg $Pt(acac)_2$ deposition had a significantly larger range of measured R/L than the 25 mg deposition. Decreases in R/L were observed from both mass loadings of iridium: 1.1 ± 6.5 % from 5 mg $Ir(acac)_3$ and 14.2 ± 4.2 % from 25 mg $Ir(acac)_3$. The R/L results from the iridium deposition are the closest to and second best after its neighbor on the periodic table, platinum. This suggests that, like platinum, the smoother coatings and smaller particles indicate better electrical interaction with the underlying CNTs, which leads to improved interconnection of the CNT substrate. Overall however, the decreases in R/L exhibited by platinum, particularly at low mass loadings, indicate that platinum is the preferred candidate for nanometal interconnection and seeding.

Precursor	Precursor Mass (mg)	Deposited Mass Percent (w/w)	Change in R/L (%)
$Cu(acac)_2$	5	15.2 ± 5.0 %	8.9 ± 4.4 %
	25	63.7 ± 1.9 %	13.2 ± 5.9 %
$Ni(acac)_2$	5	30.2 ± 8.9 %	7.3 ± 1.0 %
	25	68.0 ± 8.5 %	8.5 ± 2.4 %
$Pd(acac)_2$	5	27.3 ± 4.1 %	7.1 ± 3.6 %
	25	61.3 ± 0.9 %	4.8 ± 0.3 %
$Pt(acac)_2$	5	35.3 ± 5.7 %	-20.1 ± 18.9 %
	25	69.5 ± 5.0 %	-15.0 ± 4.9 %
$Ru(acac)_3$	5	10.5 ± 2.9 %	3.3 ± 0.3 %
	25	32.9 ± 2.5 %	-5.2 ± 3.1 %
$Rh(acac)_3$	5	13.3 ± 3.0 %	8.2 ± 4.4 %
	25	56.9 ± 5.1 %	0.3 ± 0.9 %
$Ir(acac)_3$	5	17.6 ± 4.3 %	-1.1 ± 6.5 %
	25	63.8 ± 3.2 %	-14.2 ± 4.2 %

Figure 42. Summary of deposited masses and resistance per lengths from one hour CFH-CVD at 200°C with three roving in parallel at 350 mA/roving of 5 mg and 25 mg of $Ni(acac)_2$, $Pd(acac)_2$, $Ru(acac)_3$, $Rh(acac)_3$, and $Ir(acac)_3$.

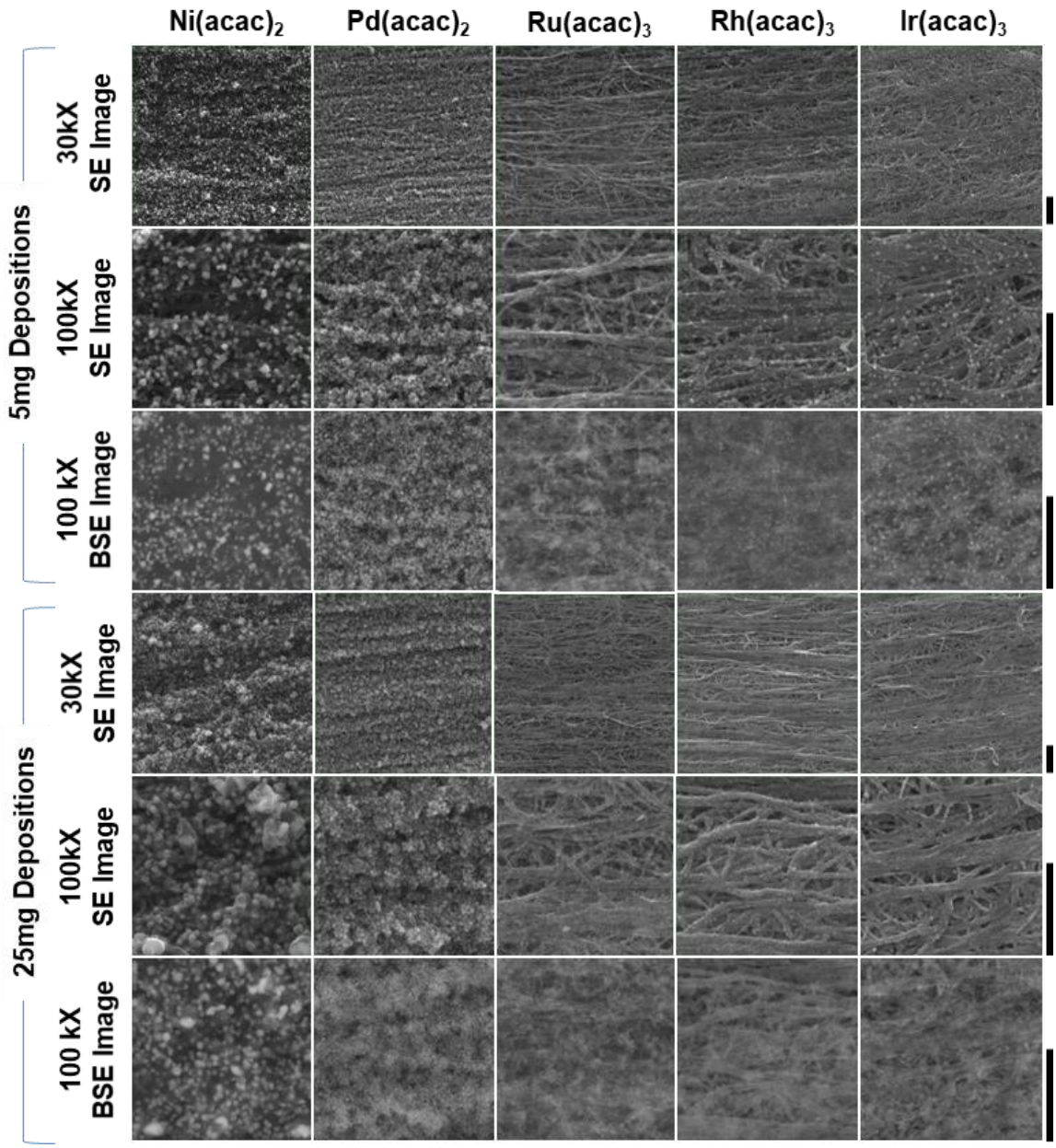

Figure 43. SE and BSE images of the precursors presented in this section. The scale bars to the right of each row represent 1 μm.

5.3. TMHD Precursors: Copper, Chromium, and Cobalt

Chromium and cobalt were deposited from $Cr(TMHD)_3$ and $Co(TMHD)_3$ precursors. To ensure a more direct comparison with copper, CFH-CVD was also performed with $Cu(TMHD)_2$. CFH-CVD of $Cu(THMD)_2$ produced generally larger

particles from both the 5 mg and 25 mg depositions. In the imaged regions, 5 mg $Cu(THMD)_2$ (Figure 44a) appears to deposit larger particle than 25 mg $Cu(THMD)_2$ (Figure 44b). However, this is within the normal particle size range of each sample depending on the local deposition density. The deposited masses were 9.46 ± 3.32 % w/w from the 5 mg and 53.7 ± 3.4 % w/w from the 25 mg $Cu(TMHD)_2$ deposition. As expected, the deposited masses are lower than the deposited masses from the equivalent weight of $Cu(acac)_2$ precursor due to the higher mass of the TMHD ligand (183.2 g/mol) compared to the acetylacetonate ligand (99.04 g/mol). The measured R/L increased from both $Cu(TMHD)_2$ depositions, similar to the $Cu(acac)_2$ depositions. The 5 mg $Cu(TMHD)_2$ deposition leads to an increase in R/L of 19.4 ± 3.4 % while the 25 mg $Cu(TMHD)_2$ deposition leads to an increase in R/L of 13.8 ± 1.7 %. CFH-CVD of $Cr(THMD)_3$ produced very light depositions of 3.41 ± 1.90 % w/w from 5 mg precursor and 9.33 ± 1.61 % w/w from 25 mg precursor. In the SEM data, no visible particles are noted from 5 mg precursor (Figure 44c), while a few sparse smaller particles are noted from 25 mg precursor (Figure 44d). Increases in R/L comparable to those of $Cu(TMHD)_2$ are observed from the $Cr(acac)_3$, with an increase of 16.2 ± 3.6 % from 5 mg $Cr(acac)_3$ and an increase of 14.9 ± 0.5 % from 25 mg $Cr(acac)_3$. After CFH-CVD of 5 mg $Co(acac)_3$, some damage in the form of small notches was observed in the CNT roving. This could be due to electrical arcing between inadequately separated CNT template strands or an unexpected reaction with the precursor. As a result, there was a *decrease* of 2.13 ± 1.00 % w/w in the mass. However, small nanoparticles are still visible in the SEM shown in Figure 44e. The 5 mg $Co(acac)_3$ deposition led to an increase in the R/L of 25.3 ± 3.3 %. The 25 mg $Co(acac)_3$ deposition led to more typical results, with

34.2 ± 3.2 % w/w deposited mass leading to an increase of 12.5 ± 5.1 % in R/L. The spherical nanoparticles deposited from 25 mg $Co(acac)_3$ visible in Figure 44f were larger than those deposited from the 5 mg deposition. As none of these samples decreased in R/L, the results indicate that the platinum group metals outperform the cobalt and chromium. A summary of the deposited masses and electrical data is presented in Figure 45. With the change in precursor ligand, future work could improve the understanding of the deposition dynamics from these precursors.

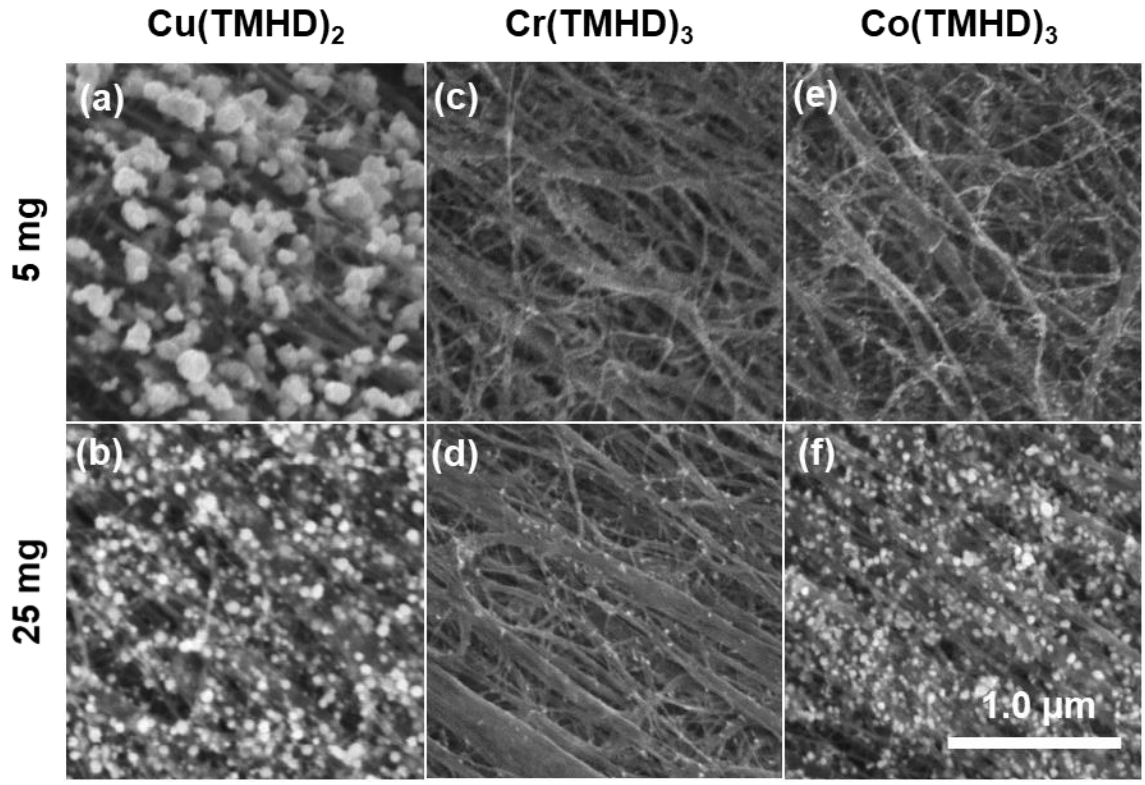

Figure 44. Secondary electron images for one hour CFH-CVD with a precursor temperature of 200°C with three roving in parallel at 350 mA/roving at 0.300 Torr for (a) 5 mg $Cu(TMHD)_2$, (b) 25 mg $Cu(TMHD)_2$, (c) 5 mg $Cr(TMHD)_3$, (d) 25 mg $Cr(TMHD)_3$, (e) 5 mg $Co(TMHD)_3$, (f) 25 mg $Co(TMHD)_3$.

Precursor	Precursor Mass (mg)	Deposited Mass Percent (w/w)	Change in R/L (%)
$Cu(TMHD)_2$	5.00	9.5 ± 3.3 %	19.4 ± 3.4 %
	25.00	53.7 ± 3.4 %	13.7 ± 1.6 %
$Cr(TMHD)_3$	5.00	3.4 ± 1.9 %	16.2 ± 3.6 %
	25.00	9.3 ± 1.6 %	14.9 ± 0.5 %
$Co(TMHD)_3$	5.00	-2.1 ± 1.0 %	25.3 ± 3.3 %
	25.00	34.2 ± 3.2 %	12.5 ± 5.1 %

Figure 45. Summary of deposited masses and resistance per lengths from one hour CFH-CVD at 200°C with three roving in parallel at 350 mA/roving of 5 mg and 25 mg of $Cu(TMHD)_2$, $Cr(TMHD)_3$, and $Co(TMHD)_3$.

5.4. Other Precursors

A few other precursors were investigated in early studies. While these precursors were not investigated in depth, the work is presented here for the sake of completeness. Silver was deposited in a one hour DFH-CVD from 100 mg Ag(acac) (CAS #15525-64-1, Alfa-Aesar 98%) at 200°C and 166 Torr onto three roving in parallel biased to 400 mA/roving. The percent deposition mass was 10.1 ± 4.3 % w/w. The SEM images in Figure 46a reveal the presence of very sparse nanoscale seeds. The R/L after deposition was 287 ± 5 Ω/m, yielding a specific conductivity of 363 ± 11 $S \cdot m^2/kg$. This is notably an improvement over the dried CNT roving's value of 305 ± 17 Ω/m. However, the deposition only utilized 0.57% of the available silver mass. Furthermore, the precursor has very specific storage conditions requiring a dark, inert environment with a temperature of 2-8°C for storage. Tungsten was deposited from 40 mg $WH_2(cpy)_2$ (CAS # 1271-33-6, Sigma Aldrich 97%) at 150°C and 0.300 Torr onto three roving in parallel

biased to 350 mA/roving. The deposition resulted in an acicular morphology shown in Figure 46b at 82.1 ± 0.9 % w/w. There was no change in the resultant R/L of 355 ± 2 Ω/m, leading to a low specific conductivity of 52.7 ± 3.6 $S \cdot m^2/kg$.

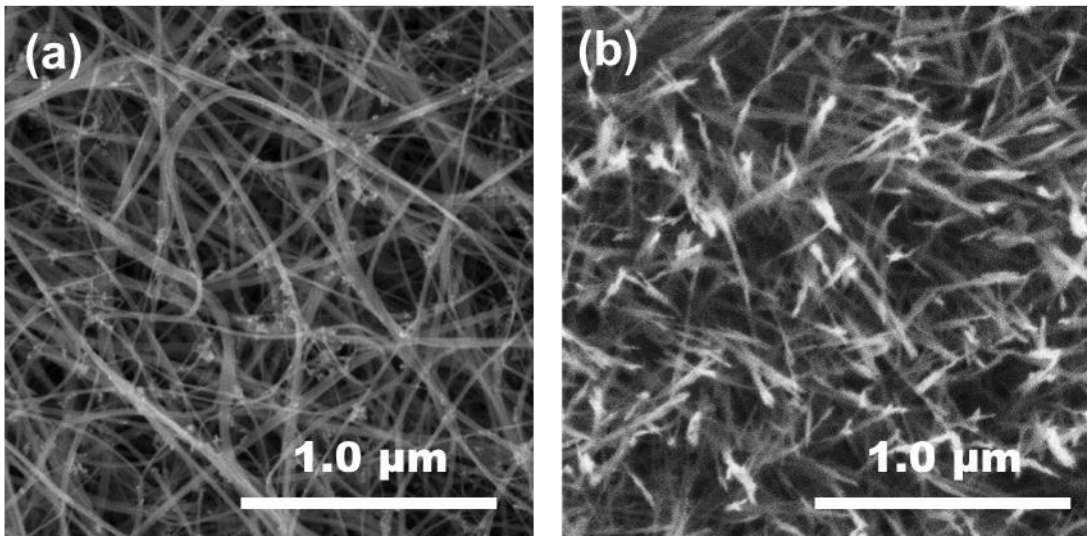

Figure 46. Secondary electron images of (a) a one hour DFH-CVD of a one hour DFH-CVD from 100 mg Ag(acac) at 200°C and 166 Torr onto three roving in parallel biased to 400 mA/roving and (b) a one hour CFH-CVD of 40 mg $WH_2(cpy)_2$ at 150°C and 0.300 Torr onto three roving in parallel biased to 350 mA/roving

5.5. Conclusions

The Joule heating driven CVD technique has proven amenable to the deposition of a wide variety of metals including nickel, palladium, platinum, ruthenium, rhodium, iridium, chromium, cobalt, silver and tungsten. As seen in Figure 47, depositions of platinum group metals, especially those with higher densities and melting points (e.g. ruthenium, rhodium, iridium, and platinum) which show smaller particle sizes from light depositions and uniform coatings from heavier depositions led to the greatest improvements in the R/L. Even in the absence of enhanced electrical transport, the smaller particle sizes exhibited by the alternative seeding metals could lead to mass

savings in the interconnection of metal-CNT hybrids, as described in section 5.1. Depositions of platinum from $Pt(acac)_2$ produced the largest improvements to the R/L of seeded conductors. Particularly of interest is the 20.1 ± 18.9 % decrease in R/L from depositions of 5 mg $Pt(acac)_2$ with deposited masses of 35.3 ± 5.7 % w/w platinum. Due to its inherit advantages over the other seeding metals, platinum is chosen for a more comprehensive study in Chapter 6.

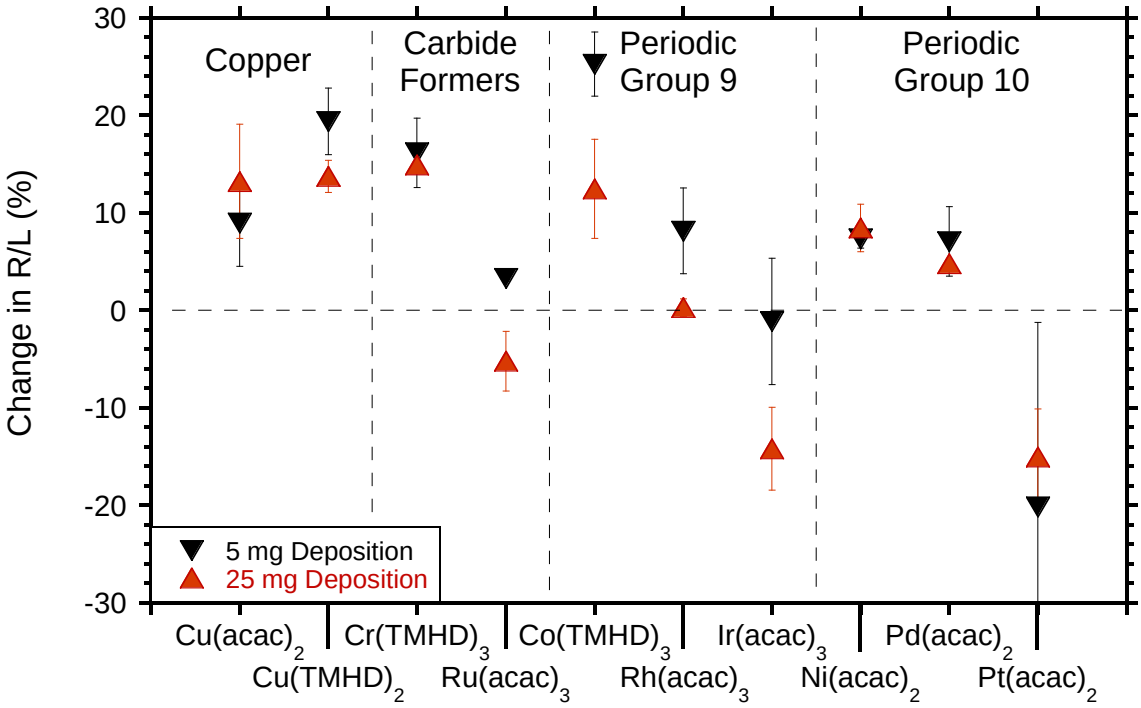

Figure 47. Summary of change in R/L from one hour CFH-CVD at 200°C with three roving in parallel at 350 mA/roving of 5 mg and 25 mg of selected compounds

CHAPTER 6: OPTIMIZATION OF SEEDED CONDUCTORS

6.1. Introduction

In this chapter, an in depth study of the Joule heating driven CVD of platinum nanometal seeds is carried out in comparison to the baseline copper seeds. To produce the highest quality hybrid electrical conductors, the impact of the mass and morphology of

the seeds deposited via CVD must are thoroughly investigated. In this work, the effects of deposition pressure, the interval and intensity of the applied heating current, and precursor mass on the deposited nanometal mass and morphology are explored in depth. Platinum nanometal seeds deposited from platinum acetylacetonate [$Pt(acac)_2$] are shown to fulfill the criteria of an effective interfacial interconnection metal, lowering the resistance while increasing specific conductivity of nanometal seeded composites. After electrodeposition of a copper overcoat, densification, and annealing, the $Pt(acac)_2$ seeded Cu-CNT hybrids are measured to produce combinations of high specific conductivity and low TCR that indicate good electrical interconnection of the conductors, with conductivities approaching those of traditional metals.

6.2. Control Over Deposited Particle Mass and Morphology

A study was carried out in which the system pressure was lowered from 0.300 Torr to 0.175 Torr at 200°C for depositions of 5 mg and 25 mg $Pt(acac)_2$. As with the $Cu(acac)_2$ depositions at various pressures, the $Pt(acac)_2$ depositions exhibited a higher density of surface particles at the higher pressure of 0.300 Torr (Figure 48a,c) and a decreased density of surface particles from the depositions at 0.170 Torr (Figure 48b,d). The deposited masses were similar for both depositions, as shown in Figure 48e, indicating that the lower pressure likely lead to improved infiltration of the vapor phase precursor. However, the change in R/L was the greatest for the 5 mg $Pt(acac)_2$ deposition at 0.300 Torr. Therefore, the moderate pressure is preferred.

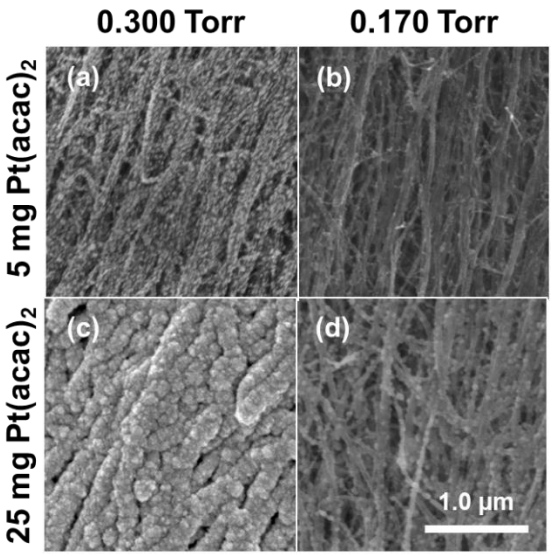

(e) $Pt(acac)_2$ Depositions

Pressure (Torr)	Precursor Mass (mg)	Deposited Mass Percent (w/w)	Change in R/L (%)
0.300	5.00	35.3 ± 5.7 %	-20.1 ± 18.9 %
	25.00	69.5 ± 5.0 %	-15.0 ± 4.9 %
0.170	5.00	27.9 ± 6.0 %	-3.50 ± 2.42 %
	25.00	66.37 ± 2.0 %	-12.6 ± 1.6 %

Figure 48. A comparison of the surface morphology of samples produced from 1 hour CFH-CVD of $Pt(acac)_2$ at 200°C with three roving in paralel at 350 mA/roving current (a) 5 mg at 0.300 Torr, (b) 5 mg at 0.170 Torr, (c) 25 mg at 0.300 Torr, (d) 25 mg at 0.170 Torr. (e) Deposited masses and change in R/L for each of the depositions.

An additional factor that can influence the deposition mass and morphology when performing Joule heating driven CVD is the time interval over which the current for deposition is applied to the CNT roving. Here, a comparison is made between a continuously applied current in the CFH-CVD process and the delayed application of current in the DFH-CVD process. The comparison of the CFH-CVD and DFH-CVD procedures was carried out with one hour depositions of 25 mg of either $Cu(acac)_2$ or $Pt(acac)_2$ precursor at 200°C, applied current of 350 mA/roving, and a pressure of 0.300 Torr. SEM images show that the $Cu(acac)_2$ precursor deposits nanoscale spherules under both DFH-CVD (Figure 49a) and CFH-CVD conditions (Figure 49b). However, the DFH-CVD conditions with $Cu(acac)_2$ lead to substantially lighter depositions of 3.62 ± 0.63 % w/w compared to the CFH-CVD deposited masses of 63.7 ± 1.9 % w/w. In comparison, while the $Pt(acac)_2$ precursor leads to tightly bound deposited particles under

the DFH-CVD condition (shown in Figure 49c), the SEM images indicate that under the CFH-CVD condition the platinum particles merged during deposition into more uniform coatings along the CNT bundles (shown in Figure 49d). Similar to the copper precursor, DFH-CVD of 25 mg $Pt(acac)_2$ leads to much lighter deposited masses of 19.1 ± 6.0 % w/w than the 69.5 ± 5.0 % w/w deposited via CFH-CVD. The lower masses obtained by DFH-CVD are attributed to the fact that only the precursor that initially condenses onto the surface of the CNT roving is available for decomposition when the current is applied at the end of the one hour period. Thus, as with the $Cu(acac)_2$ deposition, the CFH-CVD of $Pt(acac)_2$ makes more efficient utilization of the available precursor mass than the DFH-CVD approach, while the latter proves useful for producing lightweight depositions.

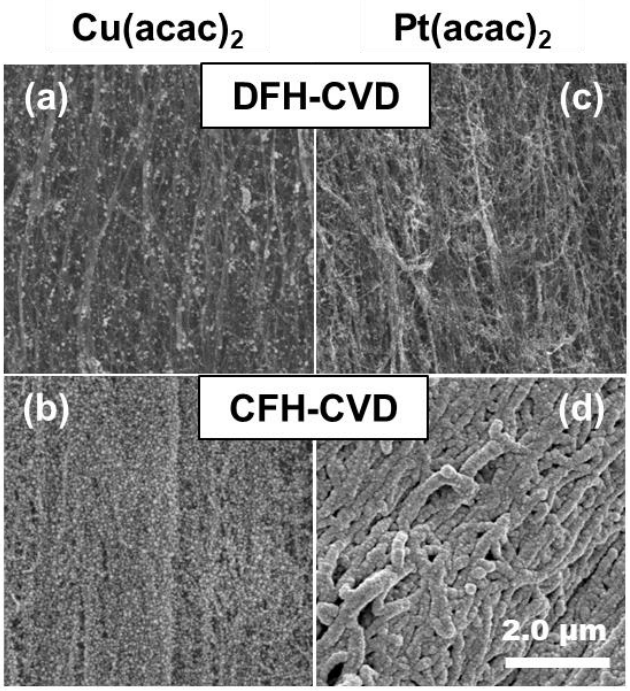

Figure 49. Deposited particle morphology from DFH-CVD of (a) $Cu(acac)_2$ and (c) $Pt(acac)_2$ precursors compared to particle morphology from CFH-CVD of (b) $Cu(acac)_2$ and (d) $Pt(acac)_2$ precursors. Samples were prepared via 1 hour CVD with 350 mA/roving, 25 mg precursor at 200°C, and 0.300 Torr.

Previous work [93] demonstrated that the temperature of the CNT roving, controlled by the applied current, can impact the mass, morphology, and distribution of deposited particles. A similar study is carried out in the present work through modification of the applied current. A control experiment is carried out outside of the reaction flask in air where currents of 150–350 mA/roving (0.45–1.05 A total) are applied to three CNT roving in parallel, and the resultant temperatures are measured. While temperatures within the flask under vacuum are undoubtedly higher, this provides a baseline understanding of the temperatures reached by the CNT roving. From the results shown in Figure 27, average temperatures of 94.1°C at 150 mA/roving, 129°C at 200 mA/roving, 168°C at 250 mA/roving, 197°C at 300 mA/roving, and 224°C at 350 mA/roving are observed. While the average temperature is relatively low, the maximum measured temperature at 200 mA/roving of 186°C approaches the decomposition onset temperature range of 225–250°C for the $Cu(acac)_2$ [99] and $Pt(acac)_2$ [103] precursors. Therefore, 200 mA/roving is chosen as the lower limit for the applied deposition current study. The upper limit of 350 mA/roving represents the highest current the roving can consistently handle in this setup without undergoing failure. In the study of applied deposition currents, conditions were constant with one hour CFH depositions using 10 mg $Cu(acac)_2$ or $Pt(acac)_2$ precursor at 200°C and 0.300 Torr with three CNT roving in parallel. Increases in mass, indicating depositions from each of the precursors, are observed at all currents from 200 mA to 350 mA, as shown in Figure 50a. This indicates temperatures in excess of the 225–250°C required for decomposition of the metal-organic precursors are reached [99,103]. Across the entire 200–350 mA/roving

current range, the deposited masses from copper were relatively invariant between 20–30 % w/w. In comparison, deposited mass from $Pt(acac)_2$ was observed to increase with increasing current from an average of 16.1 % w/w at 200 mA/roving to 58.1 % w/w at 350 mA/roving. The SEM results for the $Pt(acac)_2$ depositions demonstrate the tightly bound platinum clusters between 200–250 mA/roving (Figure 50f-g), transitioning to more uniform coatings from 300–350 mA/roving (Figure 50h-i). In contrast to the copper, the more tightly adhered platinum should form coatings and interconnections with less metal volume, as theorized in section 5.1. The $Pt(acac)_2$ CFH-CVD shows an average decrease of 10.4 % in the resistance measured from the two electrical leads during the depositions, 4X the magnitude of the decrease from the $Cu(acac)_2$ CFH-CVD. Thus, it is possible that these interconnections can lower the local resistance at the hot-spots and cools those locations below the decomposition temperature, thereby preventing further deposition from the $Pt(acac)_2$ precursor. Therefore, until the entire CNT roving exceeds the decomposition temperature of the $Pt(acac)_2$ precursor the deposited mass of platinum would be expected to increase proportionally to the applied current, as more metal is required to electrically interconnect the increasing proportion of high temperature sites on the CNT roving. The platinum appears to be able to electrically interconnect the CNT network to cool such high temperature locations.

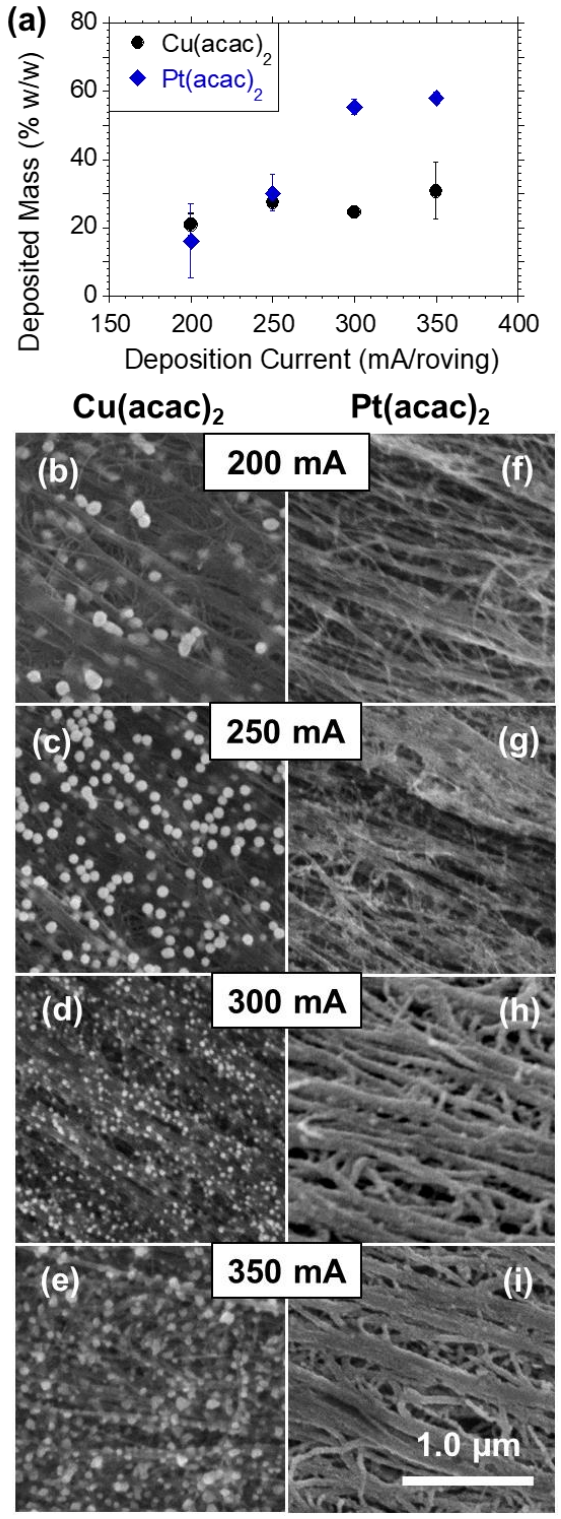

Figure 50**.** (a) Impact of current per roving on deposited particle mass. Secondary electron micrographs from (b-e) $Cu(acac)_2$ and (f-i) $Pt(acac)_2$ precursors. Samples were prepared via a 1 hour CFH-CVD, 10 mg precursor at 200°C, and 0.300 Torr.

The influence of precursor mass to drive reaction dynamics was also evaluated. As the entire mass of precursor is sublimated within the deposition time, increases in precursor mass in the flask leads to increased availability of vapor for deposition. The results of one hour depositions of precursor masses of 5, 10, 25, and 50 mg at 200°C and 0.300 Torr onto three CNT roving in parallel electrically biased to 350 mA/roving are presented in Figure 51a. As expected, deposited masses from both $Cu(acac)_2$ and $Pt(acac)_2$ are observed to increase with increasing precursor mass. The depositions from $Pt(acac)_2$ are slightly heavier at each precursor mass due to the higher mass percentage of platinum in $Pt(acac)_2$ (49.6 % w/w) compared to copper in $Cu(acac)_2$ (24.3 % w/w). However, the volume of metal available in each gram of precursor is similar, with 2.3×10^{-2} cm^3/g of platinum in $Pt(acac)_2$ and 2.7×10^{-2} cm^3/g of copper in $Cu(acac)_2$. Thus, the deposited volume of copper is actually greater than that of the platinum in the 25 mg and 50 mg depositions (as plotted in Figure 52). In the $Cu(acac)_2$ depositions, particle morphology is maintained regardless of the deposited mass (Figure 51b-e), with heavier deposited masses exhibiting increasingly dense clusters of spherical nanoparticles. In the $Pt(acac)_2$ deposition, a transition is noted between the 5 mg precursor deposition (Figure 51f) and the 10 mg precursor deposition (Figure 51g), where tightly bound nanoparticles give way to uniform coatings over the surface of the nanotubes. The platinum coatings become more dense and rough as the starting precursor mass increases to 25 mg (Figure 51h) and 50 mg (Figure 51i), as platinum fills in the interstitial space between CNT bundles. Overall, copper exhibits similar spherical morphology at all masses measured, while platinum exhibits small tightly bound particles at lighter mass loadings giving way to cohesive films at heavier mass loadings.

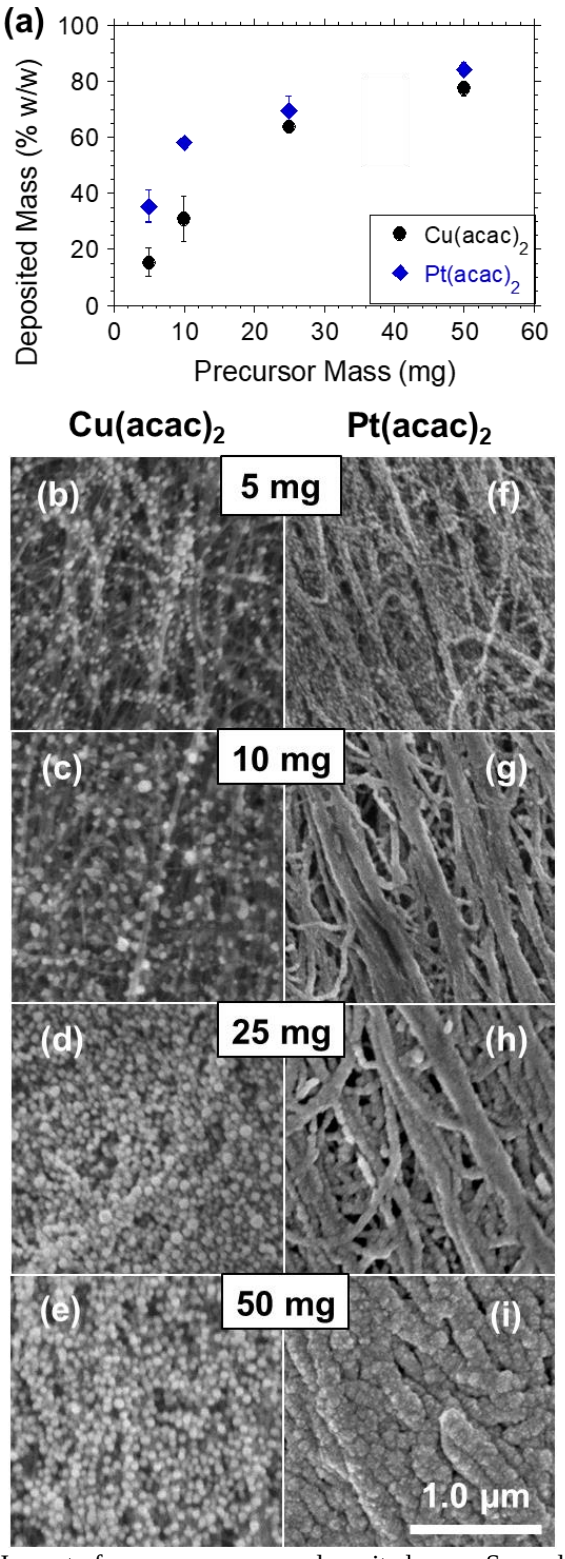

Figure 51. (a) Impact of precursor mass on deposited mass. Secondary electron micrographs from (b-e) $Cu(acac)_2$ and (f-i) $Pt(acac)_2$ precursors. Samples prepared via a 1 hour CFH-CVD with 350 mA/roving, precursor at 200°C, 0.300 Torr.

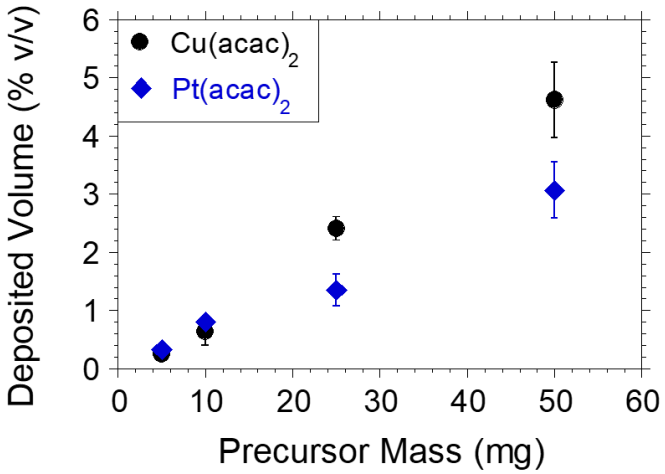

Figure 52. Impact of precursor mass on deposited volume of metal. The volume of the composite is assumed to remain unchanged during deposition due to the infiltration of the deposited metal into the pore volume of the CNT roving.

A final test investigated the impacts of a reducing heat treatment on the underlying CNT roving. Heat treated (HT) of the roving was carried out by heating to 800°C under a 5% H_2/95% Ar atmosphere for 1 hour. The HT roving decreased to an average 8.21 ± 0.37 mg/m in linear density, likely due to vaporization of more volatile carbonaceous impurities from synthesis. The R/L also rose to 399 ± 18 Ω/m. Compared to the dried roving (Figure 53a), there were no noticeable difference in morphology after the heat treatment process (Figure 53b). Importantly, there was no visible ripening of iron catalyst particles, indicating that the iron was well encapsulated within the CNT roving. CFH-CVD was carried out for 1 hour with 350 mA/roving, precursor at 200°C, 0.300 Torr for 5 mg and 10 mg of either $Cu(acac)_2$ or $Pt(acac)_2$. The 5 mg $Cu(acac)_2$ CFH-CVD onto HT roving led to a deposited mass of 21.9 ± 0.5 % w/w with a negligible change in the R/L of 0.01 ± 1.16 %. The 10 mg $Cu(acac)_2$ CFH-CVD onto HT roving led to a deposited mass of 41.0 ± 3.6 %, again with a negligible change to the R/L of 0.91 ± 1.16 %. The spherical particle morphology from 10 mg $Cu(acac)_2$ deposited onto

HT roving shown in Figure 53c is similar to that deposited onto the dried roving (Figure 51c). CFH-CVD of $Pt(acac)_2$ led to deposited masses of 35.5 ± 0.5 % w/w from 5 mg precursor and 50.6 ± 2.1 % w/w from 10 mg precursor. Both depositions led to decreases in the R/L: 14.4 ± 1.0 % from the 5 mg deposition and 34.4 ± 3.8 % lower from the 10 mg deposition. As with the $Cu(acac)_2$ deposition, the 10 mg $Pt(acac)_2$ deposition onto HT roving shown in Figure 53d led to similar coatings on the CNTs as the 10 mg deposition onto the dried roving shown in Figure 51g. For all of the depositions onto HT roving, the deposited masses are similar to the deposited masses onto dried roving, but the mass percentages are higher due to the lower starting linear density. This leads to similar effects on the specific conductivity of the seeded conductors. Overall, the heat treatment appears to have limited effects on the morphology and electrical characteristics of the resulting depositions.

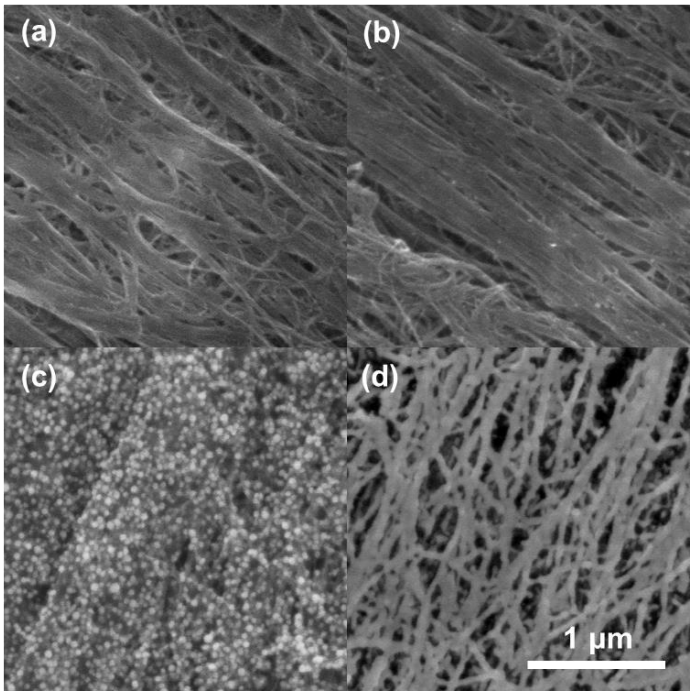

Figure 53. SE Images of (a) dried roving, (b) HT roving, and the results of 1 hour CFH-CVD with 350 mA/roving, precursor at 200°C, 0.300 Torr of 10 mg (c) $Cu(acac)_2$ and (d) $Pt(acac)_2$.

The bulk electrical characterization at room temperature for all the samples described to this point is presented in Figure 54. The R/L of the $Cu(acac)_2$ seeded samples are generally higher than the dried CNT roving, as shown in Figure 54a. In contrast, the $Pt(acac)_2$ seeded samples exhibit lower R/L than the CNT roving over nearly all mass loadings. The greatest decreases in R/L were noted between 20–50 % w/w deposited platinum mass, with some samples exhibiting nearly 40% reduction from the dried CNT roving. The R/L data in Figure 54a demonstrates that the copper depositions are not enhancing electrical transport, but rather acting as electronic scattering sites. In comparison, the lower R/L of the platinum samples indicates improvement to the electronic transport, and the platinum may be acting as electrical interconnections between the CNT bundles [81]. Measurement of the mass per length (M/L) allows for calculation of the specific conductivity, which gives an indication of the improvements to the conductance on a mass specific basis, i.e. whether improvements in R/L are greater than the added mass. The specific conductivity is calculated by multiplying the reciprocal of the R/L by the reciprocal of the M/L, which is equivalent to normalizing the electrical conductivity to the conductor's density [19,30,121]. In this study the specific conductivity can provide a quantification of the degree of utilization of deposited metal mass in the electrical conductor [93]. As can be seen from the resulting data (Figure 54b), the greatest improvements to specific conductivity are observed in the $Pt(acac)_2$ seeded samples with < 50 % w/w platinum mass with top performing samples around 30 % w/w platinum mass. Consistent with the R/L data, the $Pt(acac)_2$ seeded samples outperform the Cu seeded samples across all mass loadings in specific conductivity. This is particularly notable because copper has a specific conductivity over 10× greater than platinum. While

improvements to electrical conductance through site-specific CVD of metals have been noted at the nanoscale [81], the results presented here demonstrate the initial applicability using platinum for this technique to bulk CNT electrical conductors.

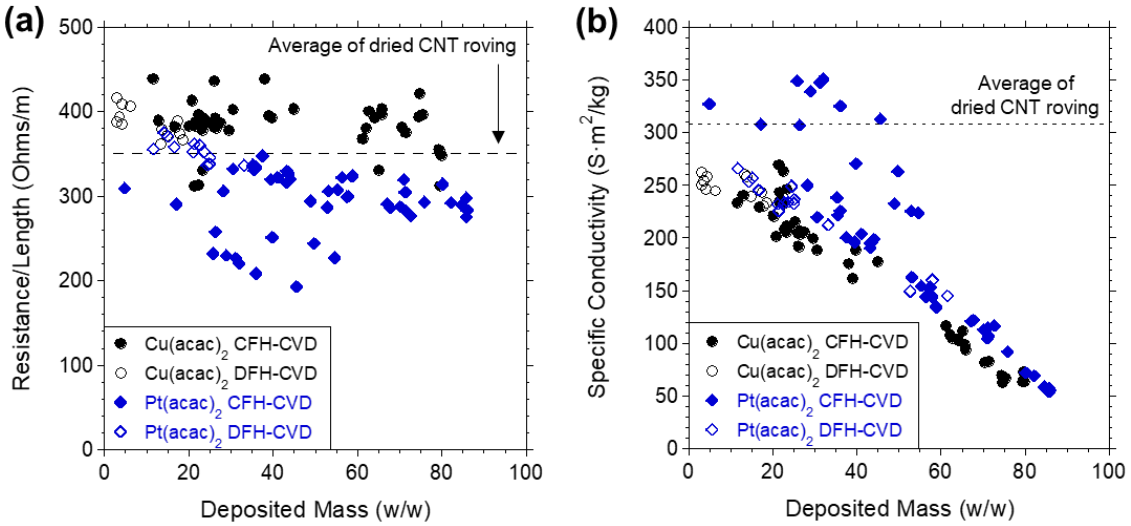

Figure 54. Summary of (a) resistance per length and (b) specific conductivity of varying mass depositions from CFH-CVD of $Pt(acac)_2$ and $Cu(acac)_2$ onto CNT Roving.

Along with the encouraging improvements to R/L and specific conductivity of the $Pt(acac)_2$ seeded samples, the case for interconnection would be enhanced through the measurement of a low TCR. Temperature dependent electrical properties are measured using a Janis VPF-800 cryostat attached to a National Instruments NI PXI-4110 programmable power supply and an NI PXI-4072 digital multimeter. Resistance was measured through an IV sweep up to 100 mA in a four-point probe configuration at a base pressure of 10^{-6} mBar from 300 K to 600 K (26.85°C to 326.85°C) with an interval of 5 K. The data presented is from the second cycle to eliminate the effects of high temperature annealing and atmospheric doping [84,85] from the measurements. Figure 55 plots the change in resistance relative to 300 K of the dried CNT roving, $Pt(acac)_2$ seeded samples with deposited masses from 31 to 86 w/w% platinum (from the series presented

in Figure 51a), and the literature values for platinum [122] with increasing temperature. For linear trends, such as that of the $Pt(acac)_2$ seeded CNTs, the TCR relative to 300 K (TCR_{300K}) can be calculated from the slope of the resistance relative to its value at 300 K over the temperature range [123]. While the dried roving does not exhibit a strictly linear trend in its relative resistance, an approximation of the TCR_{300K} using the linear method was calculated to be 2.18×10^{-4} K^{-1}. The measured series of samples with 31 to 86 w/w% platinum all exhibit similar increases in relative resistance from 300 K to 600 K. For the $Pt(acac)_2$ seeded samples, the TCR_{300K} ranges from 0.57×10^{-3} K^{-1} to 0.71×10^{-3} K^{-1} over this range of masses. These TCR_{300K} values are on the same order of magnitude as the linear approximation for the as-received CNT roving, and approximately an order of magnitude lower than the literature value for platinum (3.47×10^{-3} K^{-1}) [122]. Overall, the relative invariance to platinum metal loading for the temperature dependent electrical properties over this wide range of masses suggests electrical interconnection between the platinum and carbon nanotube fractions, especially when considered in combination with the improvements to specific conductivity.

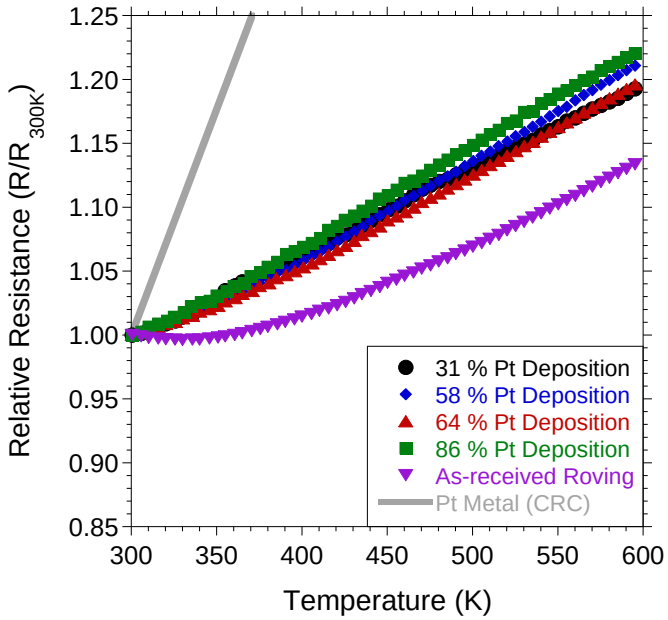

Figure 55. Relative resistance of CFH-CVD seeded samples from various precursors masses compared to platinum and as-received roving. 1 hour CFH-CVD with 350 mA/roving, precursor at 200°C, 0.300 Torr.

To provide further insight into the temperature dependent resistance data, measurements were taken from 80 K – 600 K for dried CNT roving and platinum seeded samples produced from CFH-CVD of either 5 mg (21 % w/w Pt) or 25 mg (68 % w/w Pt) of $Pt(acac)_2$ at 200°C, with 350 mA/roving, 0.175 Torr. The resistivity for each sample was estimated based on the average cross sectional area of roving. The Kaiser model [89] described in section 2.2.1 was fitted using the generalized reduced gradient algorithm to reduce the sum of squares of residuals. As expected from thick networks of CNTs like the CNT roving the variable range hopping component did not contribute to the fit [124], so that term was removed. The data with the fitted model is shown in Figure 56a, with fitting parameters presented in Figure 56b. For each of the samples, an R^2 value of at least 0.99 was obtained. The results from the model show that the ratio of the metallic phonon backscattering resistance component (A) to the fluctuation assisted tunneling

resistance (B) decreased in each of the $Pt(acac)_2$ seeded samples. This indicates that metallic conduction mechanisms are playing a larger role in the conductivity. T_m was observed to decrease with increasing platinum seed mass, indicating that increased metal content potentially reduces the energy for phonon scattering (potentially from metal particles adhered to CNT sidewalls). The T_b parameter was found to decrease with increasing seed mass, which corresponds with a decrease in the tunneling energy barrier: $E_b = T_b * k_B$. This provides further evidence that platinum is leading to nanometal interconnections, rather than acting as a separate parallel conductive medium. The low temperature fitting parameter T_s was also observed to decrease with increasing platinum mass. However, the low T_s at higher metal masses is attributed to a lack of information about the resistivity of the data near absolute zero, rather than representing an actually trend (as evidenced by the proportionally larger error in the T_s value). Overall, the Kaiser model reveals that a decrease in the ratio of the metallic phonon backscattering resistance (A) to the fluctuation assisted tunneling resistance (B) fitting factors along with a substantial decrease in the fluctuation assisted tunneling barrier energy (E_b) indicating more metal-like conduction in the CNTs with smaller barriers due to the platinum nanometal interconnection.

(a)

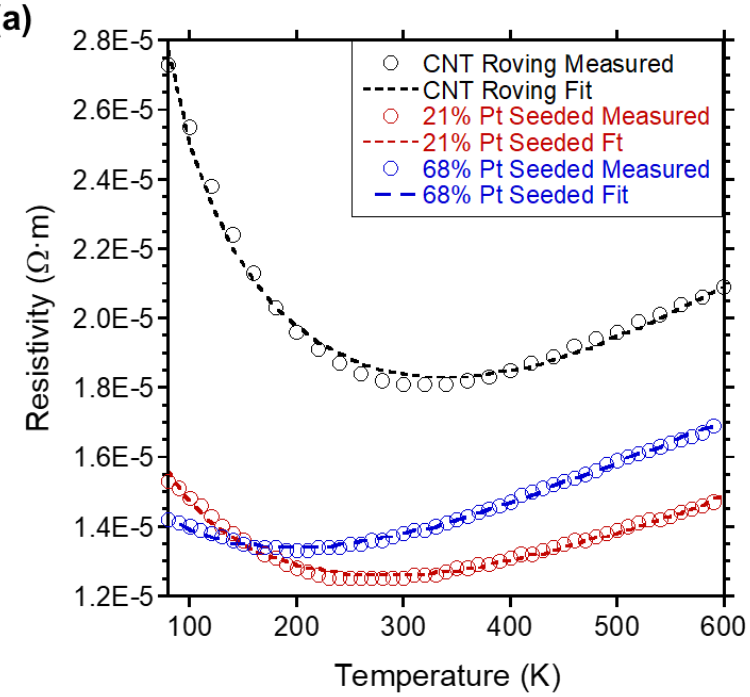

(b)

Model Parameter	Dried Roving		5 mg Pt(acac)$_2$ Seeded		25 mg Pt(acac)$_2$ Seeded	
	R^2 = 0.9926		R^2 = 0.9908		R^2 = 0.9991	
	Value	St. Err	Value	St. Err	Value	St. Err
% Deposited Pt	0	N/A	20.97	N/A	67.56	N/A
A (Ω·μm)	46.07	5.73	24.69	2.05	21.87	0.55
T_m (K)	1335	117	1151	79	980	25
B (Ω·μm)	13.96	0.67	10.34	0.40	12.49	0.14
T_b (K)	84	17	54	14	11	3
T_s (K)	43	17	53	23	0	14
A/B	3.30	0.44	2.39	0.22	1.75	0.05
E_b (meV)	7.23	1.47	4.66	1.23	0.95	0.24

Figure 56. (a) Plot of temperature dependent resistivity from 80 K to 600 K for dried and platinum seeded roving with best fit lines from the Kaiser model [89]. (b) Table of fitted parameters from the model.

The Lekawa-Raus model [23] described in section 2.2.1 was also fitted to the dried and platinum seeded roving using the same method described above. The fit, shown in Figure 57a, of the Lekawa-Raus model exhibited slightly lower R^2 values (~0.97 for the dried roving and 5 mg $Pt(acac)_2$ seeded roving), given in Figure 57b, than the fit of the Kaiser model. This leads to greater uncertainty in the fitted parameters. However, similar conclusions can be drawn from the resulting fit. The temperature of highest conductivity (T_0) was observed to decrease to lower temperature with increasing platinum mass. Similarly, the δ parameter was observed to decrease with increasing platinum mass. The combination indicates a transition to more metal like conduction at lower temperatures. The activation energy parameter, T_A, decreased with increasing platinum mass. This provides a similar trend of decreasing energy required (E_A) for hopping at higher platinum masses. As with the T_s parameter of the Kaiser model, the correlation temperature (T_C) has a large error due to the lack of data near absolute zero. Overall, the shift of the point of maximum conductivity (lowest resistivity) towards lower temperatures coupled with decreasing hopping activation energy at higher platinum masses indicate that the seeding improves metallic type conduction and reduces the barriers between conducting regions. Thus, despite the differences in the derivation of the two models, both the Kaiser and Lekawa-Raus models support the idea of platinum nanometal interconnection.

(a)

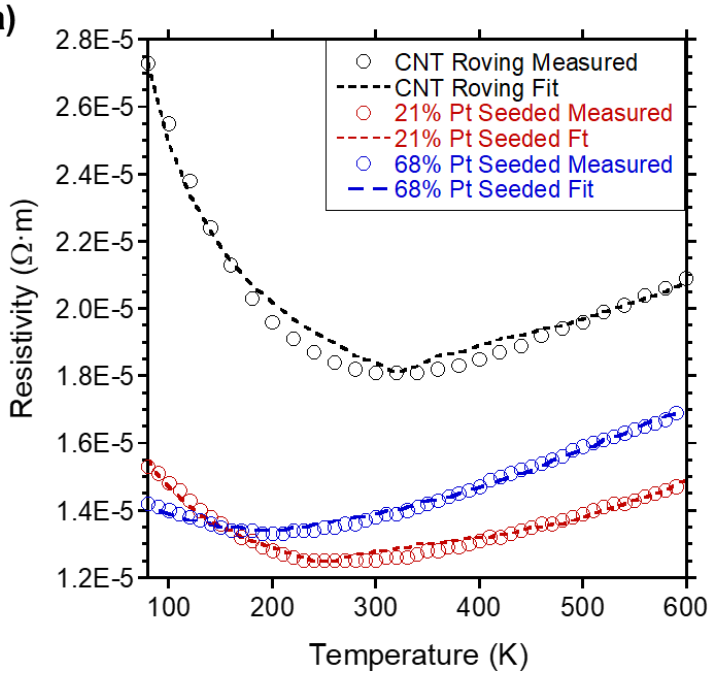

(b)

Model Parameter	Dried Roving		5 mg $Pt(acac)_2$ Seeded Fit		25 mg $Pt(acac)_2$ Seeded Fit	
	R^2 = 0.9793		R^2 = 0.9719		R^2 = 0.9958	
	Value	St. Err	Value	St. Err	Value	St. Err
% Deposited Pt	0	N/A	20.97	N/A	67.56	N/A
T_0 (K)	320	N/A	250	N/A	200	N/A
R_{T0} (K)	1.81E-05	N/A	1.25E-05	N/A	1.33E-05	N/A
T_A (K)	77	39	55	52	19	36
T_C (K)	305	148	342	304	350	695
β	5.34E-04	4.95E-04	2.79E-04	2.76E-04	3.43E-05	2.12E-06
δ (K)	3629	669	3056	676	1376	36
E_A (meV)	6.60	3.35	4.72	4.49	1.62	3.07

Figure 57. (a) Plot of temperature dependent resistivity from 80 K to 600 K for dried and platinum seeded roving with best fit lines from the Lekawa-Raus model [23]. (b) Table of fitted parameters from the model.

6.3. Production of $Pt(acac)_2$ Seeded Cu-CNT Conductors via Electroplating

The collective results from SEM and electrical measurements lead to the conclusion that platinum is an effective interconnection metal over the range of 20–50 % w/w metal. Therefore, CNT roving with ~30 % w/w platinum seeds deposited via DFH-CVD and CFH-CVD were subsequently processed into hybrid electrical conductors via electroplating, densification, and annealing. Electroplating was carried out in the "sandwich" cell configuration described previously [93]. Briefly, the CVD seeded CNT roving is placed between a folded piece of Whatman 42 filter paper to act as a separator. Strips of battery grade copper foil are placed on either side of the filter paper as an anode. The cell stack is then placed between two glass slides and wrapped in Kapton tape to provide even compression. This cell is then submerged in the copper electroplating solution (Transene Acid Copper) and hooked up to a power source (Arbin BT2000).

Here, three constant current electroplating rates of 9.4, 11, and 15 A/g are chosen to study the impact of plating rate on the infiltration of copper in samples produced through DFH-CVD. Plating rates are presented based on the mass of the CNT roving (A/g) rather than its surface area (A/cm^2) due to local variations in the material's surface area. The plating time was adjusted between 50 minutes and 3 hours to achieve a similar average total metal mass of 94.5 ± 0.2 % w/w. The electroplated samples were then finished by densification in a rolling mill and annealing at 300°C for 3 hours in 5 % H_2/95 % Ar gas. As shown in Figure 58a, the slowest plating rate (9.4 A/g) exhibited the smallest increase in resistance with temperature, equating to a TCR_{300K} of 3.12×10^{-3} K^{-1}. The middle plating rate (11 A/g) exhibited an increase in resistance

somewhere between the faster and slower rate, with a TCR_{300K} of 3.33×10^{-3} K^{-1}. Finally, the fastest plating rate (15 A/g) exhibited the greatest increase in resistance with temperature, equating to a TCR_{300K} of 3.50×10^{-3} K^{-1}. Previous literature regarding the production of Cu-CNT conductors indicate that low TCR in a hybrid electrical conductor is a result of good intermixing of the CNT and metal portions of the conductor [53,56,77,125]. In this study, faster plating rates are also correlated with higher specific conductivities. The specific conductivities are 4126 $S \cdot m^2/kg$ for the 9.4 A/g plating rate, 4776 $S \cdot m^2/kg$ for the 11 A/g plating rate, and 5772 $S \cdot m^2/kg$ for the 15 A/g plating rate. These combinations of specific conductivity and TCR agree well with the theory of infiltration: heavier copper surface coatings produced through faster plating rates are more conductive, but less electrically integrated with the underlying seeded CNTs, thus producing higher temperature coefficients. The samples seeded via CFH-CVD of $Pt(acac)_2$ were electroplated at rates of 4.9 A/g and 7.6 A/g. The 4.9 A/g plated sample exhibited a TCR_{300K} of 2.74×10^{-3} K^{-1} with a specific conductivity of 3127 $S \cdot m^2/kg$. The 7.6 A/g plated sample exhibited a TCR_{300K} of 3.33×10^{-3} K^{-1} and specific conductivity 4519 $S \cdot m^2/kg$. The CFH-CVD seeded samples are similar to the DFH-CVD seeded samples, demonstrating that both deposition techniques achieve similar results. Overall, a balance exists at this mass loading between infiltration of the hybrid with copper and maintaining sufficient copper cohesion to achieve high specific conductivity.

A useful approach described previously [93] for probing the interaction between the metal and CNT fraction of a hybrid electrical conductor is to compare the specific conductivity and temperature coefficient of resistance for the conductor to the values expected from a non-interacting system of parallel copper and CNT electrical conductors.

Such a system can be modeled across all mass percentages of copper and CNTs, producing a curve as shown in Figure 58b spanning from 100 % CNTs to 100 % copper. Conductors with a combination of a lower TCR and higher specific conductivity than expected from this parallel-conductors model indicate a favorable interaction between the metal and CNT portions of the conductor. Such conductors are positioned above the curve on Figure 58b. As can be seen from the resulting data, each of the $Pt(acac)_2$ seeded, copper plated CNT conductors reside above the rule of mixtures curve indicating favorable interaction between the metals and CNTs. Additionally, the hybrid conductor produced at the 15 A/g electroplating rate shows an improvement over previously published results [93], with slight improvements to both specific conductivity and TCR. These results demonstrate the utility of platinum as an interconnection metal, as well as serving as an enhanced seed metal for copper electroplating in a hybrid design.

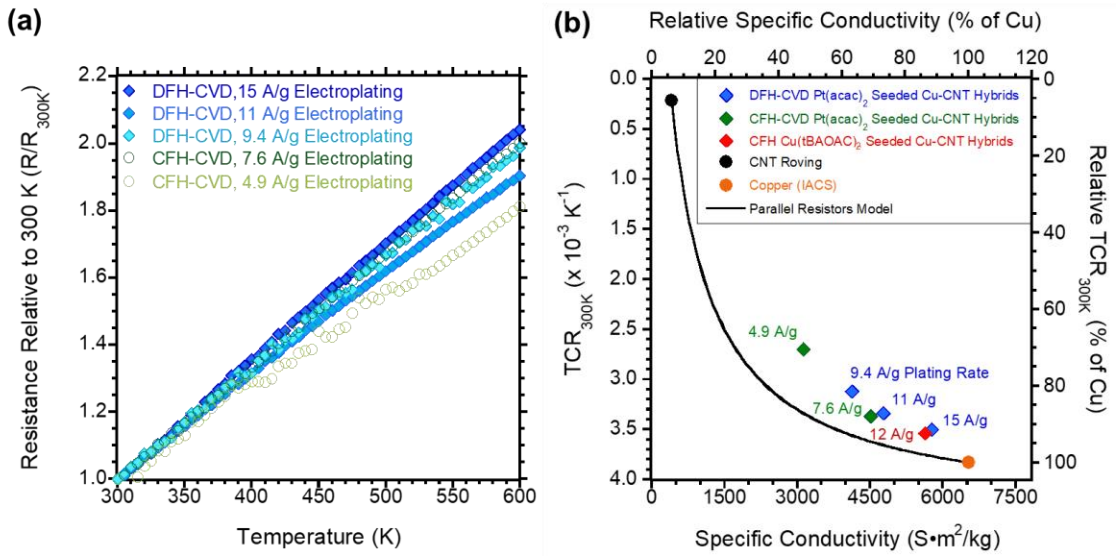

Figure 58. (a) Relative resistance of samples electroplated to 94.5% w/w total metal mass with various plating rates from samples with ~30% w/w platinum seed mass after DFH-CVD or CFH-CVD. (b) TCR and specific conductivity of samples plated with various plating rates compared to the parallel resistors model and previously published data [93]. Note the inverted y-axis (TCR_{300K}) on the plot.

The bulk electrical conductivity represents the electrical transport in a conductor adjusted for the cross-sectional area and can be used to compare with other reported hybrid conductors. SEM cross-sections are acquired for the platinum seeded Cu-CNT hybrids by sectioning the conductor with a razorblade to determine the electrical conductivity and investigate the infiltration of the metal into the CNT roving. A representative SEM cross-section is provided in Figure 59, with false color imaging used to indicate the region of interest.

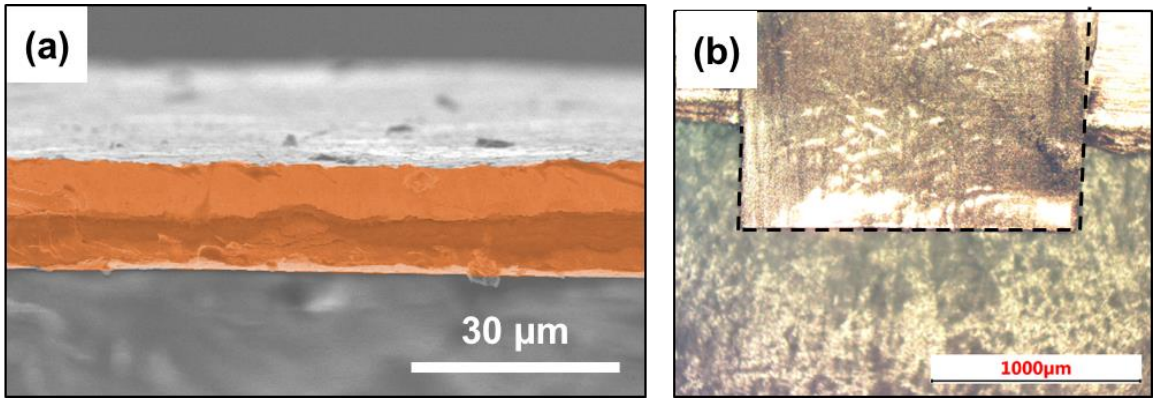

Figure 59. (a) A typical example of an SEM cross-section of the $Pt(acac)_2$ seeded Cu-CNT conductor from the 11 A/g plating rate used to measure thickness for conductivity analysis, with the cross-sectional area highlighted in false color. (b) Optical micrograph of a top view utilized to measure the width of the $Pt(acac)_2$ seeded Cu-CNT conductor from the 11 A/g plating rate, edges outlined in black.

From the measured cross-sectional areas, conductivities for the DFH-CVD samples of 22.1 MS/m for the 9.4 A/g plating rate, 29.8 MS/m for the 11 A/g plating rate, and 29.3 MS/m for the 15 A/g plating rate are calculated. For the CFH-CVD sample with a 7.6 A/g plating rate, a conductivity of 26.9 MS/m is calculated. These values are among the highest reported for Cu-CNT hybrid conductors at or below this mass loading of

copper, as seen in Figure 60a. These values are also on the same order of magnitude as those for traditional metals like copper (58 MS/m) and aluminum (38 MS/m).

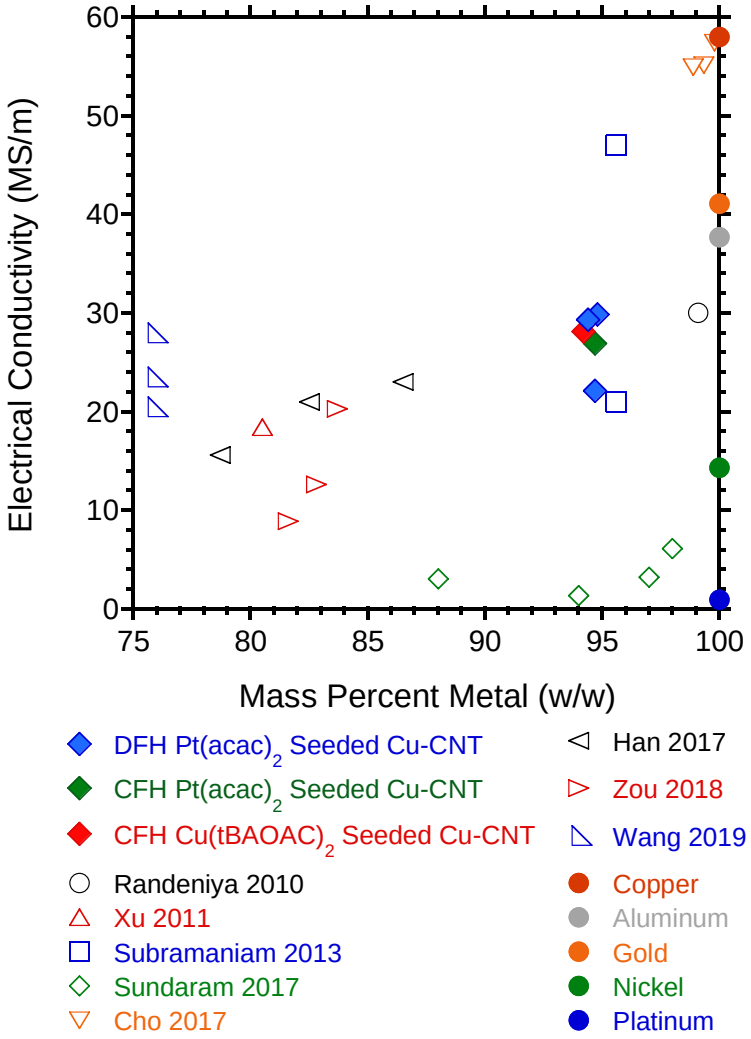

Figure 60. (a) Conductivity of top performing samples compared to previous work [93] and the state of the field: Randeniya (2010) [60], Xu (2011) [79], Subramaniam (2013) [53], Sundaram (2017) [56], Cho (2017) [77], Han (2017) [58], Zou (2018) [55], and Wang (2019) [105].

Cross-sections for EDS were produced by setting the samples in epoxy, cross sectioning with an ultramicrotome, and then coating the exposed sample surface with about 15 nm of conductive carbon. EDS is carried out in a Tescan Mira3 SEM equipped

with a Bruker XFlash 6|30 EDS under an accelerating voltage of 20 keV. EDS of a cross-section (Figure 61a) of the top-performing 11 A/g sample reveals the presence of platinum seeds (Figure 61b) through the interior volume of the final conductor. While the signal from the electrodeposited copper (Figure 60c) is much more prominent on the exterior of the hybrid conductor's surface, the microstructure of the interfacial area indicates a degree of integration due to the change in grain structure [64]. The carbon shows a complementary trend (Figure 61d), indicating that the exterior of the electrical conductor is mostly copper. However, the iron signal (Figure 61e), which arises form leftover catalyst enveloped within the CNT bundles, again indicates integration between the CNTs and copper. Finally, the nonspecific and dampened oxygen signal (Figure 61f) indicates the presence of metals rather than oxides within the annealed conductor. The spectrum from the analyzed area is presented in Figure 61g. Overall, these results demonstrate the first instance of the use of CVD to produce a platinum-interconnected Cu-CNT conductor with electrical conductivity comparable to that of traditional metals.

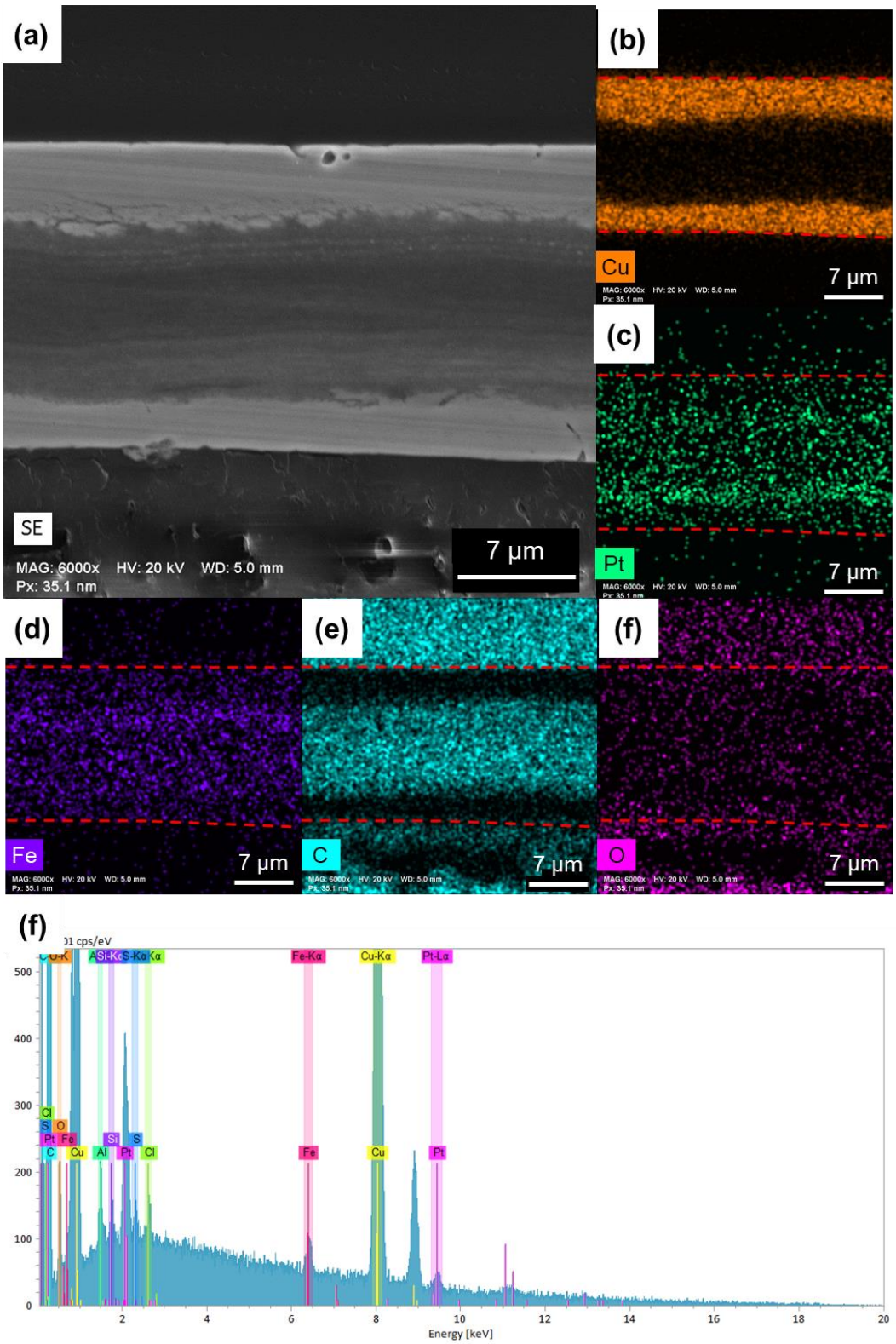

Figure 61. (a) Secondary electron image of the cross section of the 11 A/g plating sample. The EDS maps of the (b) Cu Kα, (c) Pt Lα, (d) Fe Kα, (e) C Kα, and (f) O Kα signals. (g) Spectrum from the cross-section.

6.4. Conclusions

In this work, we have demonstrated the versatility of a site-selective Joule heating driven CVD technique towards the production of nanometal interconnected CNT hybrid conductors. An in-depth study into the deposition of platinum has been carried out with the impact of various processing parameters investigated. Deposited mass was controlled by modification of precursor temperature, with temperatures up to 200°C allowing for the complete sublimation of the acetylacetonate precursor and the highest deposited masses. Decreasing the system pressure from 166 Torr to 0.175 Torr produced similar mass loadings, but a lower density of surface particles. Thus, lower pressures seem to lead to a higher degree of infiltration of the nanometal vapor into the CNT roving. Further refinement to deposited masses can be made by modifying the interval of the applied heating current to the CNT roving, with masses as low as 5 % w/w obtained through DFH-CVD and masses as high as 85 % w/w obtained through CFH-CVD. Modification of the of applied current used to Joule-heat the CNT roving led to changes in the deposited particle morphology, with transition from site-specific $Pt(acac)_2$ depositions noted at 200–250 mA giving way to more uniform coatings from 300–350 mA. Average deposited seed mass and volume were also controlled by varying the amount of precursor in the reaction chamber, leading to sparse deposition at low precursors masses and heavier coverage at higher precursor masses. Generally, the platinum group elements (platinum, palladium, ruthenium, rhodium, and iridium) led to smaller particle sizes, more uniform coatings, and better post-deposition R/L than copper or nickel. The broad applications of the Joule heating driven CVD technique may have further uses towards

catalysis, sensor, and shielding applications. Platinum seeds in particular displayed improved adhesion and interaction with the CNT roving substrate through its nanoscale particles and smooth coatings. Over the full range of masses investigated, the R/L of the seeded conductors was lower with depositions from $Pt(acac)_2$ than from $Cu(acac)_2$. Deposition from $Pt(acac)_2$ with masses less than 50 % w/w led to the greatest improvements in specific conductivity of the seeded CNT conductors. Platinum depositions from 31–86 % w/w all exhibited TCR_{300K} much closer to that of the CNT roving than bulk platinum metal, indicating good interaction between the seed metal and CNTs. Modeling of the temperature dependent resistivity data indicates more metallic type conduction in the platinum seeded conductors with a marked decrease in the tunneling barrier between conducting regions. To the best of the authors' knowledge, this is the first demonstration of the use of platinum nanometal interconnection in a bulk CNT conductor. Electroplated, densified and annealed hybrid conductors produced from samples with ~30 % w/w platinum exhibited combinations of TCR and specific conductivity better than that expected from non-interacting parallel conductors, indicating integration of the metal and CNT portions of the hybrid. Finally, electrical conductivities of up to 29.8 MS/m at room temperature were obtained, approaching conventional metals like copper (58 MS/m) and aluminum (38 MS/m).

CHAPTER 7: DISSERTATION CONCLUSIONS

Overall, this work has demonstrated the viability of Joule heating driven site-specific chemical vapor deposition to produce nanometal interconnected Cu-CNT hybrid electrical conductors. The CVD technique has demonstrated the ability to target

depositions towards hot spots by adjusting the amount of current applied to the CNT template conductor. This allows for the reinforcement of these potential sites of failure through the targeted deposition of additional conductive pathways. The CVD technique is a fast and efficient method of depositing nanometal seeds throughout a porous CNT roving template, saving time over previous methods such as organic electroplating. The deposited nanometal particles may act as interconnections in their own right, as well as seed sites for further electroplating.

Chapter 3 establishes the utility of the Joule-heating driven CVD technique for the deposition of nanometal particles. Copper nanoparticles are deposited throughout the interior volume of a porous CNT roving material from a $Cu(tBAOAC)_2$ precursor, as verified through BSE and EDS imaging. Compared to previous seeding methods, the CVD seeding method can be completed in the period of an hour or less with seeds uniquely deposited in localized regions due to the temperature differences (from the localized resistance). The distribution of the deposited seed particles may be controlled by changing the amount of applied current to the CNT roving, allowing for hot-spot site-specificity at currents of 200 mA to 300 mA or more uniform depositions of nanometal seeds at 400 mA. Electroplating of the conductors to 94.2 % w/w copper produces conductivity 569× higher and specific conductivity 13.8× higher than the as-received roving with a TCR_{300K} of 3.53×10^{-3} K^{-1}.

Chapter 4 explores the impact of the various CVD parameters on the resulting seed depositions. Longer deposition times led to heavier deposited masses at appropriate pressures. Increases in precursor temperature lead to increases in the sublimation rate, allowing for heavier deposited seed masses in a given time. Decreases in system pressure

allow for an increased mean free path of the vapor phase precursor, which lead to increased infiltration of the vapor into the CNT roving at a given seed mass. Heavier precursor masses correlate with heavier deposited masses due to an increased amount of metal available for deposition. The amount of applied current controls the deposition towards site-specificity or uniformity. Finally, the CFH-CVD process allows for improved utilization efficiency of the metal organic precursor, while the DFH-CVD process produces consistently lightweight depositions.

Chapter 5 presents a survey and comparison of potential seed metal candidates. Copper, nickel, palladium, platinum, cobalt, rhodium, iridium, ruthenium, chromium, tungsten, and silver have all been deposited from metal organic precursors in the vapor phase. Generally, metals with a lower atomic numbers that were less dense and had lower melting points tended to form larger, more discrete particles on the CNT roving with higher R/L than the dried CNT roving. Metals with higher atomic numbers, higher densities, and higher melting points tended to deposit tightly bound particles and coatings to the underlying CNT bundles with lower R/L than the dried CNT roving. In particular, the platinum group metals ruthenium, rhodium, iridium, and platinum led to improvements in R/L, with the best results from depositions of $Pt(acac)_2$. Thus, platinum was chosen for comparison to copper in optimized conductors.

Chapter 6 contains a comparison of copper and platinum seeded CNT roving. Using the various control parameters presented in Chapter 4, masses of 5 % w/w to 85 % w/w metal seeds were deposited with the Joule heating driven CVD method. Platinum depositions from 31–86 % w/w all exhibited TCR_{300K} much closer to that of the CNT roving than bulk platinum metal. Furthermore, modelling of the temperature

dependent resistivity indicates more metallic conduction with much lower tunneling barriers in the platinum seeded CNTs than the dried CNT roving, indicating good interaction between the platinum seed metal and CNTs. Platinum produces the greatest decreases in R/L and improvements to specific conductivity with 20-50 % w/w platinum seeds. CVD seeded CNT conductors with ~30 % w/w platinum are electroplated with copper, densified, and annealed produce Cu-CNT hybrid conductors with specific conductivities as high as 5772 $S \cdot m^2/kg$ and TCR (from 300–600 K) as low as $2.74 \times 10^{-3}\ K^{-1}$, indicating good interconnection of the metal and CNT portions. Room temperature electrical conductivities of 29.8 MS/m are achieved, comparable to metallic electrical conductors. High conductivity, low TCR electrical conductors such as the nanometal interconnected Cu-CNT hybrids have numerous future applications towards high efficiency motors, generators, and transformers. Such nanometal depositions may also find future use in catalytic applications.

APPENDIX A: ABBREVIATIONS

BSE, backscatter electron

CFH, continuous filament heating

CNT, carbon nanotube

Cu(acac)$_2$, copper (II) acetylacetonate

Cu-CNT, copper-carbon nanotube

Cu(tBAOAC)$_2$, bis(t-butylacetoacetato) copper (II)

CVD, chemical vapor deposition

DFH, delayed filament heating

EDS, energy dispersive x-ray spectroscopy

FIB, focused ion beam

Ir(acac)$_3$, iridium (III) acetylacetonate

IV sweep, current-potential sweep

M/L, mass per length

NICCs, nanometal interconnected carbon conductors

Ni(acac)$_2$, nickel (II) acetylacetonate

Pd(acac)$_2$, palladium (II) acetylacetonate

PFH, pulsed filament heating

Pt(acac)$_2$, platinum (II) acetylacetonate

Rh(acac)$_3$, rhodium (III) acetylacetonate

Ru(acac)$_3$, ruthenium (III) acetylacetonate

R/L, resistance per length

SE, secondary electron

SEM, scanning electron microscopy

TCR, temperature coefficient of resistance

LIST OF REFERENCES

[1] S. Reich, C. Thomsen, J. Maultzsch, Carbon Nanotubes: Basic Concepts and Physical Properties, WILEY-VCH Verlag GmBH & Co., Weinheim, 2007. https://doi.org/10.1002/9783527618040.

[2] M.S. Dresselhaus, G. Dresselhaus, P. Avouris, Carbon Nanotubes Synthesis, Structure, Properties, and Applications, 3rd ed., Springer-Verlag Berlin Heidelberg, 2001. https://doi.org/10.1080/20014091104189.

[3] M.J. O'Connell, Carbon nanotubes: Properties and application, Taylor & Francis Group, LLC, Boca Raton, FL, 2004. https://doi.org/10.1016/j.mser.2003.10.001.

[4] S. Bellucci, P. Onorato, Physical Properties of Ceramic and Carbon Nanoscale Structures, 2011. https://doi.org/10.1007/978-3-642-15778-3.

[5] S. Reich, C. Thomsen, P. Ordejón, Electronic band structure of isolated and bundled carbon nanotubes, Phys. Rev. B - Condens. Matter Mater. Phys. 65 (2002) 1554111–15541111. https://doi.org/10.1103/PhysRevB.65.155411.

[6] K.S. Novoselov, A.K. Geim, S. V Morozov, D. Jiang, M.I. Katsnelson, I. V Grigorieva, S. V Dubonos, A.A. Firsov, Two-dimensional gas of massless Dirac fermions in graphene, Nature. 438 (2005) 197–200. https://doi.org/10.1038/nature04233.

[7] S.R.P. Silva, Y. Tison, Y. Hayashi, V. Stolojan, C.E. Giusca, The Inner Shell Influence on the Electronic Structure of Double-Walled Carbon Nanotubes, Adv. Mater. 20 (2007) 189–194. https://doi.org/10.1002/adma.200700399.

[8] S. Ilani, P.L. McEuen, Electron Transport in Carbon Nanotubes, Annu. Rev. Condens. Matter Phys. 1 (2010) 1–25. https://doi.org/10.1146/annurev-conmatphys-070909-103928.

[9] O. Hjortstam, P. Isberg, S. Söderholm, H. Dai, Can we achieve ultra-low resistivity in carbon nanotube-based metal composites?, Appl. Phys. A Mater. Sci. Process. 78 (2004) 1175–1179. https://doi.org/10.1007/s00339-003-2424-x.

[10] D. Hecht, L. Hu, G. Grüner, Conductivity scaling with bundle length and diameter in single walled carbon nanotube networks, Appl. Phys. Lett. 89 (2006) 133112. https://doi.org/10.1063/1.2356999.

[11] S. Li, Z. Yu, C. Rutherglen, P.J. Burke, Electrical properties of 0.4 cm long single-walled carbon nanotubes, Nano Lett. 4 (2004) 2003–2007. https://doi.org/10.1021/nl048687z.

[12] S. Sanvito, Y.K. Kwon, D. Tománek, C.J. Lambert, Fractional Quantum Conductance in Carbon Nanotubes, Phys. Rev. Lett. 84 (2000) 1974–1977. https://doi.org/10.1103/PhysRevLett.84.1974.

[13] J.H. Lehman, M. Terrones, E. Mansfield, K.E. Hurst, V. Meunier, Evaluating the characteristics of multiwall carbon nanotubes, Carbon. 49 (2011) 2581–2602. https://doi.org/10.1016/j.carbon.2011.03.028.

[14] S. Frank, P. Poncharal, Z.L. Wang, W.A. De Heer, Carbon nanotube quantum resistors, Science. 280 (1998) 1744–1746. https://doi.org/10.1126/science.280.5370.1744.

[15] M. Monthioux, V.L. Kuznetsov, Who should be given the credit for the discovery of carbon nanotubes?, Carbon. 44 (2006) 1621–1623. https://doi.org/10.1016/j.carbon.2006.03.019.

[16] A. Jorio, G. Dresselhaus, M.S. Dresselhaus, Topics in Applied Physics Volume 111. Carbon Nanotubes: Advanced Topics in the Synthesis, Structure, Properties and Applications, Springer-Verlag Berlin Heidelberg, 2008. https://doi.org/https://doi.org/10.1007.
[17] H.M. Cheng, F. Li, X. Sun, S.D.M. Brown, M.A. Pimenta, A. Marucci, G. Dresselhaus, M.S. Dresselhaus, Bulk morphology and diameter distribution of single-walled carbon nanotubes synthesized by catalytic decomposition of hydrocarbons, Chem. Phys. Lett. 298 (1998) 602–610. https://doi.org/https://doi.org/10.1016/S0009-2614(98)00479-5.
[18] A.S. Wu, T.W. Chou, J.W. Gillespie, D. Lashmore, J. Rioux, Electromechanical response and failure behaviour of aerogel-spun carbon nanotube fibres under tensile loading, J. Mater. Chem. 22 (2012) 6792–6798. https://doi.org/10.1039/c2jm15869h.
[19] A.R. Bucossi, C.D. Cress, C.M. Schauerman, J.E. Rossi, I. Puchades, B.J. Landi, Enhanced Electrical Conductivity in Extruded Single-Wall Carbon Nanotube Wires from Modified Coagulation Parameters and Mechanical Processing, ACS Appl. Mater. Interfaces. 7 (2015) 27299–27305. https://doi.org/10.1021/acsami.5b08668.
[20] P. Jarosz, C. Schauerman, J. Alvarenga, B. Moses, T. Mastrangelo, R. Raffaelle, R. Ridgley, B. Landi, Carbon nanotube wires and cables: Near-term applications and future perspectives, Nanoscale. 3 (2011) 4542–4553. https://doi.org/10.1039/c1nr10814j.
[21] K. Liu, Y. Sun, R. Zhou, H. Zhu, J. Wang, L. Liu, S. Fan, K. Jiang, Carbon nanotube yarns with high tensile strength made by a twisting and shrinking method, Nanotechnology. 21 (2010) 045708. https://doi.org/10.1088/0957-4484/21/4/045708.
[22] N. Behabtu, C.C. Young, D.E. Tsentalovich, O. Kleinerman, X. Wang, A.W.K. Ma, E.A. Bengio, R.F. Ter Waarbeek, J.J. De Jong, R.E. Hoogerwerf, S.B. Fairchild, J.B. Ferguson, B. Maruyama, J. Kono, Y. Talmon, Y. Cohen, M.J. Otto, M. Pasquali, Strong, light, multifunctional fibers of carbon nanotubes with ultrahigh conductivity, Science. 339 (2013) 182–186. https://doi.org/10.1126/science.1228061.
[23] A. Lekawa-Raus, K. Walczak, G. Kozlowski, M. Wozniak, S.C. Hopkins, K.K. Koziol, Resistance-temperature dependence in carbon nanotube fibres, Carbon. 84 (2015) 118–123. https://doi.org/10.1016/j.carbon.2014.11.062.
[24] A. Lekawa-Raus, T. Gizewski, J. Patmore, L. Kurzepa, K.K. Koziol, Electrical transport in carbon nanotube fibres, Scr. Mater. 131 (2017) 112–118. https://doi.org/10.1016/j.scriptamat.2016.11.027.
[25] National Bureau of Standards, Copper wire tables, 3rd ed., Washington, D.C., 1914.
[26] L.F.C. Pereira, C.G. Rocha, A. Latǵ, J.N. Coleman, M.S. Ferreira, Upper bound for the conductivity of nanotube networks, Appl. Phys. Lett. 95 (2009) 123106. https://doi.org/10.1063/1.3236534.
[27] A. Buldum, J.P. Lu, Contact resistance between carbon nanotubes, Phys. Rev. B. 63 (2001) 161403. https://doi.org/10.1103/PhysRevB.63.161403.
[28] M.P. Garrett, I.N. Ivanov, R.A. Gerhardt, A.A. Puretzky, D.B. Geohegan,

Separation of junction and bundle resistance in single wall carbon nanotube percolation networks by impedance spectroscopy, Appl. Phys. Lett. 97 (2010) 163105. https://doi.org/10.1063/1.3490650.
[29] J. Lee, I.Y. Stein, M.E. Devoe, D.J. Lewis, N. Lachman, S.S. Kessler, S.T. Buschhorn, B.L. Wardle, Impact of carbon nanotube length on electron transport in aligned carbon nanotube networks, Appl. Phys. Lett. 106 (2015) 053110. https://doi.org/10.1063/1.4907608.
[30] A. Lekawa-Raus, J. Patmore, L. Kurzepa, J. Bulmer, K. Koziol, Electrical properties of carbon nanotube based fibers and their future use in electrical wiring, Adv. Funct. Mater. 24 (2014) 3661–3682. https://doi.org/10.1002/adfm.201303716.
[31] F. Xu, A. Sadrzadeh, Z. Xu, B.I. Yakobson, Can carbon nanotube fibers achieve the ultimate conductivity? - Coupled-mode analysis for electron transport through the carbon nanotube contact, J. Appl. Phys. 114 (2013) 063714. https://doi.org/10.1063/1.4818308.
[32] J. Liu, A.G. Rinzler, H. Dai, J.H. Hafner, R.K. Bradley, P.J. Boul, A. Lu, T. Iverson, K. Shemilov, C.B. Huffman, F. Rodriguez-Macias, Y.-S. Shon, T.R. Lee, D.T. Colbert, R.E. Smalley, Fullerene Pipes, Science. 280 (1998) 1253–1256. https://doi.org/10.1002/bip.1974.360131003.
[33] L.M. Ericson, H. Fan, H. Peng, V.A. Davis, W. Zhou, J. Sulpizio, Y. Wang, R. Booker, J. Vavro, C. Guthy, A.N.G. Parra-vasquez, M.J. Kim, S. Ramesh, R.K. Saini, C. Kittrell, G. Lavin, H. Schmidt, W.W. Adams, W.E. Billups, M. Pasquali, W. Hwang, R.H. Hauge, J.E. Fischer, R.E. Smalley, Macroscopic , Neat , Single-Walled Carbon Nanotube Fibers, Science. 305 (2004) 1447–1450.
[34] V.A. Davis, A.N.G. Parra-vasquez, M.J. Green, P.K. Rai, N. Behabtu, V. Prieto, R.D. Booker, J. Schmidt, E. Kesselman, W. Zhou, H. Fan, W.W. Adams, R.H. Hauge, J.E. Fischer, Y. Cohen, Y. Talmon, R.E. Smalley, M. Pasquali, True solutions of single-walled carbon nanotubes for assembly into macroscopic materials, Nat. Nanotechnol. 4 (2009) 830–834. https://doi.org/10.1038/nnano.2009.302.
[35] V.A. Davis, L.M. Ericson, A.N.G. Parra-vasquez, H. Fan, Y. Wang, V. Prieto, J.A. Longoria, S. Ramesh, R.K. Saini, C. Kittrell, W.E. Billups, W.W. Adams, R.H. Hauge, R.E. Smalley, M. Pasquali, Phase Behavior and Rheology of SWNTs in Superacids, (2004) 154–160.
[36] R.J. Headrick, D.E. Tsentalovich, J. Berdegué, E.A. Bengio, L. Liberman, O. Kleinerman, M.S. Lucas, Y. Talmon, M. Pasquali, Structure-Property Relations in Carbon Nanotube Fibers by Downscaling Solution Processing, Adv. Mater. 30 (2018) 1704482. https://doi.org/10.1002/adma.201704482.
[37] D.E. Tsentalovich, R.J. Headrick, F. Mirri, J. Hao, N. Behabtu, C.C. Young, M. Pasquali, Influence of Carbon Nanotube Characteristics on Macroscopic Fiber Properties, ACS Appl. Mater. Interfaces. 9 (2017) 36189–36198. https://doi.org/10.1021/acsami.7b10968.
[38] Y.L. Li, I.A. Kinloch, A.H. Windle, Direct spinning of carbon nanotube fiber from chemical vapor deposition synthesis, Science. 304 (2004) 276–278. https://doi.org/10.1126/science.1094982.
[39] C. Liu, Z. Yu, D. Neff, A. Zhamu, B.Z. Jang, Graphene-based supercapacitor with

an ultrahigh energy density, Nano Lett. 10 (2010) 4863–4868. https://doi.org/10.1021/nl102661q.
[40] M.D. Yadav, K. Dasgupta, A.W. Patwardhan, J.B. Joshi, High Performance Fibers from Carbon Nanotubes: Synthesis, Characterization, and Applications in Composites - A Review, Ind. Eng. Chem. Res. 56 (2017) 12407–12437. https://doi.org/10.1021/acs.iecr.7b02269.
[41] M. Miao, Yarn spun from carbon nanotube forests: Production, structure, properties and applications, Particuology. 11 (2013) 378–393. https://doi.org/10.1016/j.partic.2012.06.017.
[42] P. Jarosz, C. Schauerman, J. Alvarenga, B. Moses, T. Mastrangelo, R. Raffaelle, R. Ridgley, B. Landi, Carbon nanotube wires and cables: Near-term applications and future perspectives, Nanoscale. 3 (2011) 4542–4553. https://doi.org/10.1039/c1nr10814j.
[43] P. Liu, D.C.M. Hu, T.Q. Tran, D. Jewell, H.M. Duong, Electrical property enhancement of carbon nanotube fibers from post treatments, Colloids Surfaces A Physicochem. Eng. Asp. 509 (2016) 384–389. https://doi.org/10.1016/j.colsurfa.2016.09.036.
[44] S. Li, X. Zhang, J. Zhao, F. Meng, G. Xu, Z. Yong, J. Jia, Z. Zhang, Q. Li, Enhancement of carbon nanotube fibres using different solvents and polymers, Compos. Sci. Technol. 72 (2012) 1402–1407. https://doi.org/10.1016/j.compscitech.2012.05.013.
[45] M.S. Fuhrer, M.L. Cohen, A. Zettl, V. Crespi, Localization in single-walled carbon nanotubes, Solid State Commun. 109 (1998) 105–109. https://doi.org/10.1016/S0038-1098(98)00520-1.
[46] Y. Dini, J. Faure-Vincent, J. Dijon, A unified electrical model based on experimental data to describe electrical transport in carbon nanotube-based materials, Nano Res. 13 (2020) 1764–1779. https://doi.org/10.1007/s12274-020-2803-z.
[47] R.D. Downes, A. Hao, J.G. Park, Y.F. Su, R. Liang, B.D. Jensen, E.J. Siochi, K.E. Wise, Geometrically constrained self-assembly and crystal packing of flattened and aligned carbon nanotubes, Carbon. 93 (2015) 953–966. https://doi.org/10.1016/j.carbon.2015.06.012.
[48] J. Alvarenga, P.R. Jarosz, C.M. Schauerman, B.T. Moses, B.J. Landi, C.D. Cress, R.P. Raffaelle, J. Alvarenga, P.R. Jarosz, C.M. Schauerman, B.T. Moses, B.J. Landi, C.D. Cress, R.P. Raffaelle, High conductivity carbon nanotube wires from radial densification and ionic doping, 97 (2010) 182106. https://doi.org/10.1063/1.3506703.
[49] Y. Zhao, J. Wei, R. Vajtai, P.M. Ajayan, E. V Barrera, Iodine doped carbon nanotube cables exceeding specific electrical conductivity of metals, Sci. Rep. 1 (2011) 83. https://doi.org/10.1038/srep00083.
[50] D. Janas, K.Z. Milowska, P.D. Bristowe, K.K.K. Koziol, Improving the electrical properties of carbon nanotubes with interhalogen compounds, Nanoscale. 9 (2017) 3212–3221. https://doi.org/10.1039/C7NR00224F.
[51] C.D. Cress, M.J. Ganter, C.M. Schauerman, K. Soule, J.E. Rossi, C.C. Lawlor, I. Puchades, S.M. Ubnoske, A.R. Bucossi, B.J. Landi, Carbon nanotube wires with continuous current rating exceeding 20 Amperes, J. Appl. Phys. 122 (2017)

025101. https://doi.org/10.1063/1.4990981.
[52] J. Di, S. Fang, F.A. Moura, D.S. Galvão, J. Bykova, A. Aliev, M.J. de Andrade, X. Lepró, N. Li, C. Haines, R. Ovalle-Robles, D. Qian, R.H. Baughman, Strong, Twist-Stable Carbon Nanotube Yarns and Muscles by Tension Annealing at Extreme Temperatures, Adv. Mater. 28 (2016) 6598–6605. https://doi.org/10.1002/adma.201600628.
[53] C. Subramaniam, T. Yamada, K. Kobashi, A. Sekiguchi, D.N. Futaba, M. Yumura, K. Hata, One hundred fold increase in current carrying capacity in a carbon nanotube–copper composite, Nat. Commun. 4 (2013) 2202. https://doi.org/10.1038/ncomms3202.
[54] C. Subramaniam, A. Sekiguchi, T. Yamada, D.N. Futaba, K. Hata, Nano-scale, planar and multi-tiered current pathways from a carbon nanotube–copper composite with high conductivity, ampacity and stability, Nanoscale. 8 (2016) 3888–3894. https://doi.org/10.1039/C5NR03762J.
[55] J. Zou, D. Liu, J. Zhao, L. Hou, T. Liu, X. Zhang, Y. Zhao, Y.T. Zhu, Q. Li, Ni Nanobuffer Layer Provides Light-Weight CNT/Cu Fibers with Superior Robustness, Conductivity, and Ampacity, ACS Appl. Mater. Interfaces. 10 (2018) 8197–8204. https://doi.org/10.1021/acsami.7b19012.
[56] R. Sundaram, T. Yamada, K. Hata, A. Sekiguchi, Electrical performance of lightweight CNT-Cu composite wires impacted by surface and internal Cu spatial distribution, Sci. Rep. 7 (2017) 9267. https://doi.org/10.1038/s41598-017-09279-x.
[57] D. Janas, K.K.K. Koziol, The influence of metal nanoparticles on electrical properties of carbon nanotubes, Appl. Surf. Sci. 376 (2016) 74–78. https://doi.org/10.1016/j.apsusc.2016.02.233.
[58] B. Han, E. Guo, X. Xue, Z. Zhao, L. Luo, H. Qu, T. Niu, Y. Xu, H. Hou, Fabrication and densification of high performance carbon nanotube/copper composite fibers, Carbon. 123 (2017) 593–604. https://doi.org/10.1016/j.carbon.2017.08.004.
[59] N.W. Ashcroft, N.D. Mermin, Solid State Physics, 1st Editio, Brooks/Cole, Belmont, 1976.
[60] L.K. Randeniya, A. Bendavid, P.J. Martin, C.D. Tran, Composite yarns of multiwalled carbon nanotubes with metallic electrical conductivity, Small. 6 (2010) 1806–1811. https://doi.org/10.1002/smll.201000493.
[61] B.T. Moses, R.P. Raffaelle, P.R. Jarosz, C.D. Cress, C.M. Schauerman, J. Alvarenga, B.J. Landi, High conductivity carbon nanotube wires from radial densification and ionic doping, Appl. Phys. Lett. 97 (2010) 182106. https://doi.org/10.1063/1.3506703.
[62] R.M. Sundaram, A. Sekiguchi, M. Sekiya, T. Yamada, K. Hata, Copper/carbon nanotube composites: research trends and outlook, R. Soc. Open Sci. 5 (2018) 180814. https://doi.org/10.1098/rsos.180814.
[63] R. Sundaram, T. Yamada, K. Hata, A. Sekiguchi, The influence of Cu electrodeposition parameters on fabricating structurally uniform CNT-Cu composite wires, Mater. Today Commun. 13 (2017) 119–125. https://doi.org/10.1016/j.mtcomm.2017.09.003.
[64] P.M. Hannula, A. Peltonen, J. Aromaa, D. Janas, M. Lundström, B.P. Wilson, K. Koziol, O. Forsén, Carbon nanotube-copper composites by electrodeposition on

carbon nanotube fibers, Carbon. 107 (2016) 281–287. https://doi.org/10.1016/j.carbon.2016.06.008.
[65] P.M. Hannula, J. Aromaa, B.P. Wilson, D. Janas, K. Koziol, O. Forsén, M. Lundström, Observations of copper deposition on functionalized carbon nanotube films, Electrochim. Acta. 232 (2017) 495–504. https://doi.org/10.1016/j.electacta.2017.03.006.
[66] P. Hannula, M. Junnila, D. Janas, J. Aromaa, O. Fors, M. Lundstrom, Carbon Nanotube Fiber Pretreatments for Electrodeposition of Copper, Adv. Mater. Sci. Eng. 2018 (2018) 3071913. https://doi.org/10.1155/2018/3071913.
[67] S. Arai, T. Osaki, M. Hirota, M. Uejima, Fabrication of copper/single-walled carbon nanotube composite film with homogeneously dispersed nanotubes by electroless deposition, Mater. Today Commun. 7 (2016) 101–107. https://doi.org/10.1016/j.mtcomm.2016.04.009.
[68] L. Zheng, J. Sun, Q. Chen, Carbon nanotubes reinforced copper composite with uniform CNT distribution and high yield of fabrication, Micro Nano Lett. 12 (2017) 722–725. https://doi.org/10.1049/mnl.2017.0317.
[69] A. Rockett, The Materials Science of Semiconductors, Springer-Verlag US, 2008. https://doi.org/https://doi.org/10.1007/978-0-387-68650-9.
[70] B. Han, E. Guo, X. Xue, Z. Zhao, T. Li, Y. Xu, L. Luo, H. Hou, Enhancement of the twisted carbon nanotube fibers properties by drawing processing and acid treatment, Mater. Des. 143 (2018) 238–247. https://doi.org/10.1016/j.matdes.2018.02.004.
[71] B. Han, E. Guo, X. Xue, Z. Zhao, T. Li, Y. Xu, L. Luo, H. Hou, Fabricating and strengthening the carbon nanotube/copper composite fibers with high strength and high electrical conductivity, Appl. Surf. Sci. 441 (2018) 984–992. https://doi.org/10.1016/j.apsusc.2018.02.078.
[72] A. Agarval, S.R. Bakshi, D. Lahiri, Carbon Nanotubes: Reinforced Metal Matrix Composites, CRC Press, Boca Raton, FL, 2011.
[73] A. Lekawa-Raus, P. Haladyj, K. Koziol, Carbon nanotube fiber-silver hybrid electrical conductors, Mater. Lett. 133 (2014) 186–189. https://doi.org/10.1016/j.matlet.2014.06.177.
[74] S.I. Cha, K.T. Kim, S.N. Arshad, C.B. Mo, S.H. Hong, Extraordinary strengthening effect of carbon nanotubes in metal-matrix nanocomposites processed by molecular-level mixing, Adv. Mater. 17 (2005) 1377–1381. https://doi.org/10.1002/adma.200401933.
[75] C. Arnaud, F. Lecouturier, D. Mesguich, N. Ferreira, G. Chevallier, C. Estournès, A. Weibel, C. Laurent, High strength – High conductivity double-walled carbon nanotube – Copper composite wires, Carbon. 96 (2015) 212–215. https://doi.org/10.1016/j.carbon.2015.09.061.
[76] C. Laurent, C. Estournès, N. Ferreira, G. Chevallier, C. Josse, A. Weibel, D. Mesguich, F. Lecouturier, C. Arnaud, High strength-high conductivity carbon nanotube-copper wires with bimodal grain size distribution by spark plasma sintering and wire-drawing, Scr. Mater. 137 (2017) 78–82. https://doi.org/10.1016/j.scriptamat.2017.05.008.
[77] S. Cho, K. Kikuchi, E. Lee, M. Choi, I. Jo, S.-B. Lee, S.-K. Lee, A. Kawasaki, Chromium carbide/Carbon Nanotube Hybrid Structure Assisted Copper

Composites with Low Temperature Coefficient of Resistance, Sci. Rep. 7 (2017) 14943. https://doi.org/10.1038/s41598-017-14915-7.
[78] S. Cho, K. Kikuchi, A. Kawasaki, On the role of amorphous intergranular and interfacial layers in the thermal conductivity of a multi-walled carbon nanotube-copper matrix composite, Acta Mater. 60 (2012) 726–736. https://doi.org/10.1016/j.actamat.2011.09.056.
[79] G. Xu, J. Zhao, S. Li, X. Zhang, Z. Yong, Q. Li, Continuous electrodeposition for lightweight, highly conducting and strong carbon nanotube-copper composite fibers, Nanoscale. 3 (2011) 4215–4219. https://doi.org/10.1039/c1nr10571j.
[80] T.Q. Tran, J.K.Y. Lee, A. Chinnappan, W.A.D.M. Jayathilaka, D. Ji, V.V. Kumar, S. Ramakrishna, Strong, lightweight, and highly conductive CNT/Au/Cu wires from sputtering and electroplating methods, J. Mater. Sci. Technol. 40 (2020) 99–106. https://doi.org/10.1016/j.jmst.2019.08.033.
[81] J.W. Do, D. Estrada, X. Xie, N.N. Chang, J. Mallek, G.S. Girolami, J.A. Rogers, E. Pop, J.W. Lyding, Nanosoldering carbon nanotube junctions by local chemical vapor deposition for improved device performance, Nano Lett. 13 (2013) 5844–5850. https://doi.org/10.1021/nl4026083.
[82] R. Sundaram, T. Yamada, K. Hata, A. Sekiguchi, The influence of Cu electrodeposition parameters on fabricating structurally uniform CNT-Cu composite wires, Mater. Today Commun. 13 (2017) 119–125. https://doi.org/10.1016/j.mtcomm.2017.09.003.
[83] N.D. Cox, A. Rape, M. Pham, J.E. Rossi, A.R. Bucossi, B.J. Landi, Free-standing silver/carbon nanotube metal matrix composite thin films, J. Mater. Sci. 51 (2016) 10935–10942. https://doi.org/10.1007/s10853-016-0305-x.
[84] P.G. Collins, K. Bradley, M. Ishigami, A. Zettl, Extreme oxygen sensitivity of electronic properties of carbon nanotubes, Science. 287 (2000) 1801–1804. https://doi.org/10.1126/science.287.5459.1801.
[85] A. Lekawa-Raus, L. Kurzepa, G. Kozlowski, S.C. Hopkins, M. Wozniak, D. Lukawski, B.A. Glowacki, K.K. Koziol, Influence of atmospheric water vapour on electrical performance of carbon nanotube fibres, Carbon. 87 (2015) 18–28. https://doi.org/10.1016/j.carbon.2015.02.018.
[86] V. Skákalová, A.B. Kaiser, Y.S. Woo, S. Roth, Electronic transport in carbon nanotubes: From individual nanotubes to thin and thick networks, Phys. Rev. B - Condens. Matter Mater. Phys. 74 (2006) 085403. https://doi.org/10.1109/ASDAM.2006.331142.
[87] P. Pipinys, A. Kiveris, Variable range hopping and/or phonon-assisted tunneling mechanism of electronic transport in polymers and carbon nanotubes, Cent. Eur. J. Phys. 10 (2012) 271–281. https://doi.org/10.2478/s11534-012-0005-3.
[88] A.B. Kaiser, Electronic transport properties of conducting polymers and carbon nanotubes, Reports Prog. Phys. 64 (2001) 1–49.
[89] A.B. Kaiser, V. Skákalová, S. Roth, Modelling conduction in carbon nanotube networks with different thickness, chemical treatment and irradiation, Phys. E Low-Dimensional Syst. Nanostructures. 40 (2008) 2311–2318. https://doi.org/10.1016/j.physe.2007.10.038.
[90] Z. Yao, C.L. Kane, C. Dekker, High-field electrical transport in single-wall carbon nanotubes, Phys. Rev. Lett. 84 (2000) 2941–2944. https://doi.org/10.1007/978-3-

540-72865-8_15.
[91] P. Sheng, Fluctuation-induced tunneling conduction in disordered materials, Phys. Rev. B. 21 (1980) 2180–2195. https://doi.org/10.1103/PhysRevB.21.2180.
[92] D.B. Williams, C.B. Carter, Transmission Electron Microscopy: A Textbook for Material Science, Second, Springer Science & Business Media, New York, 2009. https://doi.org/10.1007/978-0-387-76501-3_1.
[93] A.P. Leggiero, K.J. Trettner, H.L. Ursino, D.J. Mcintyre, M. Schauer, E. Zeira, C.D. Cress, B.J. Landi, High Conductivity Copper–Carbon Nanotube Hybrids via Site-Specific Chemical Vapor Deposition, ACS Appl. Nano Mater. 2 (2018) 118–126. https://doi.org/10.1021/acsanm.8b01740.
[94] A. Devi, J. Goswami, R. Lakshmi, S. a Shivashankar, S. Chandrasekaran, I. Introduction, A novel Cu(II) chemical vapor deposition precursor: Synthesis, characterization, and chemical vapor deposition, J. Mater. Res. 13 (1998) 687–692. https://doi.org/https://doi.org/10.1557/JMR.1998.0086.
[95] R.A. DiLeo, B.J. Landi, R.P. Raffaelle, Purity assessment of multiwalled carbon nanotubes by Raman spectroscopy, J. Appl. Phys. 101 (2007) 064307. https://doi.org/10.1063/1.2712152.
[96] K.Z. Milowska, M. Ghorbani-Asl, M. Burda, L. Wolanicka, N. Ćatić, P.D. Bristowe, K.K.K. Koziol, Breaking the electrical barrier between copper and carbon nanotubes, Nanoscale. 9 (2017) 8458–8469. https://doi.org/10.1039/c7nr02142a.
[97] J.N. Wang, X.G. Luo, T. Wu, Y. Chen, High-strength carbon nanotube fibre-like ribbon with high ductility and high electrical conductivity, Nat. Commun. 5 (2014) 3848. https://doi.org/10.1038/ncomms4848.
[98] R.G. Charles, M.A. Pawlikowski, Comparative heat stabilities of some metal acetylacetonate chelates, J. Phys. Chem. 62 (1958) 440–444. https://doi.org/10.1021/j150562a017.
[99] Y. Pauleau, A.Y. Fasasi, Kinetics of Sublimation of Copper(II) Acetylacetonate Complex Used for Chemical Vapor Deposition of Copper Films, Chem. Mater. 3 (1991) 45–50. https://doi.org/10.1021/cm00013a015.
[100] J. Von Hoene, R.G. Charles, W.M. Hickam, Thermal decomposition of metal acetylacetonates mass spectrometer studies, J. Phys. Chem. 62 (1958) 1098–1101. https://doi.org/10.1021/j150567a019.
[101] D.J. McIntyre, R.K. Hirschman, I. Puchades, B.J. Landi, Enhanced copper – carbon nanotube hybrid conductors with titanium adhesion layer, J. Mater. Sci. 55 (2020) 6610–6622. https://doi.org/10.1007/s10853-020-04457-1.
[102] X. Wang, N. Behabtu, C.C. Young, D.E. Tsentalovich, M. Pasquali, J. Kono, High-ampacity power cables of tightly-packed and aligned carbon nanotubes, Adv. Funct. Mater. 24 (2014) 3241–3249. https://doi.org/10.1002/adfm.201303865.
[103] J.R.V. Garcia, T. Goto, Chemical Vapor Deposition of Iridium, Platinum, Rhodium and Palladium, Mater. Trans. 44 (2003) 1717–1728. https://doi.org/10.2320/matertrans.44.1717.
[104] M. Ghorbani-Asl, K.Z. Milowska, M. Burda, P.D. Bristowe, K.K.K. Koziol, N. Ćatić, L. Wolanicka, Breaking the electrical barrier between copper and carbon nanotubes, Nanoscale. 9 (2017) 8458–8469. https://doi.org/10.1039/c7nr02142a.
[105] G.J. Wang, Y.J. Ma, Y.P. Cai, Z.H. Cao, X.K. Meng, Overcoming the strength-

conductivity trade-off dilemma in carbon nanotube/aluminum-copper fiber by diffusion interface and chemical reaction interface, Carbon. 146 (2019) 293–300. https://doi.org/10.1016/j.carbon.2019.01.111.
[106] S.C. Lim, J.H. Jang, D.J. Bae, G.H. Han, S. Lee, I.S. Yeo, Y.H. Lee, Contact resistance between metal and carbon nanotube interconnects: Effect of work function and wettability, Appl. Phys. Lett. 95 (2009) 2007–2010. https://doi.org/10.1063/1.3255016.
[107] G.J. Wang, Y.P. Cai, Y.J. Ma, S.C. Tang, J.A. Syed, Z.H. Cao, X.K. Meng, Ultrastrong and Stiff Carbon Nanotube/Aluminum−Copper Nanocomposite via Enhancing Friction between Carbon Nanotubes, Nano Lett. 19 (2019) 6255–6262. https://pubs.acs.org/doi/abs/10.1021/acs.nanolett.9b02332.
[108] Y. Matsuda, W.Q. Deng, W.A. Goddard, Contact resistance properties between nanotubes and various metals from quantum mechanics, J. Phys. Chem. C. 111 (2007) 11113–11116. https://doi.org/10.1021/jp072794a.
[109] I. Suarez-Martinez, A. Felten, J.J. Pireaux, C. Bittencourt, C.P. Ewels, Transition metal deposition on graphene and carbon nanotubes, J. Nanosci. Nanotechnol. 9 (2009) 6171–6175. https://doi.org/10.1166/jnn.2009.1557.
[110] A. Maiti, A. Ricca, Metal-nanotube interactions - Binding energies and wetting properties, Chem. Phys. Lett. 395 (2004) 7–11. https://doi.org/10.1016/j.cplett.2004.07.024.
[111] M.M. Savalani, C.C. Ng, Q.H. Li, H.C. Man, In situ formation of titanium carbide using titanium and carbon-nanotube powders by laser cladding, Appl. Surf. Sci. 258 (2012) 3173–3177. https://doi.org/10.1016/j.apsusc.2011.11.058.
[112] Y. Zhang, N.W. Franklin, R.J. Chen, H. Dai, Metal coating on suspended carbon nanotubes and its implication to metal-tube interaction, Chem. Phys. Lett. 331 (2000) 35–41. https://doi.org/10.1016/S0009-2614(00)01162-3.
[113] J. Xie, N. Zhang, V.K. Varadan, Functionalized carbon nanotubes in platinum decoration, Smart Mater. Struct. 15 (2006) S5–S8. https://doi.org/10.1088/0964-1726/15/1/002.
[114] S. Lee, S.J. Kahng, Y. Kuk, Nano-level wettings of platinum and palladium on single-walled carbon nanotubes, Chem. Phys. Lett. 500 (2010) 82–85. https://doi.org/10.1016/j.cplett.2010.09.082.
[115] J.-W. Do, N.N. Chang, D. Estrada, F. Lian, H. Cha, X.J. Duan, R.T. Haasch, E. Pop, G.S. Girolami, J.W. Lyding, Solution-Mediated Selective Nanosoldering of Carbon Nanotube Junctions for Improved Device Performance, ACS Nano. 9 (2015) 4806–4813. https://doi.org/10.1021/nn505552d.
[116] S. Lee, S.J. Kahng, Y. Kuk, Nano-level wettings of platinum and palladium on single-walled carbon nanotubes, Chem. Phys. Lett. 500 (2010) 82–85. https://doi.org/10.1016/j.cplett.2010.09.082.
[117] Z. Sun, Z. Liu, B. Han, Y. Wang, J. Du, Z. Xie, G. Han, Fabrication of ruthenium-carbon nanotube nanocomposites in supercritical water, Adv. Mater. 17 (2005) 928–932. https://doi.org/10.1002/adma.200400839.
[118] R. Sule, P.A. Olubambi, I. Sigalas, J.K.O. Asante, J.C. Garrett, W.D. Roos, Spark plasma sintering of sub-micron copper reinforced with ruthenium-carbon nanotube composites for thermal management applications, Synth. Met. 202 (2015) 123–132. https://doi.org/10.1016/j.synthmet.2015.02.001.

[119] Q. Cao, S.J. Han, J. Tersoff, A.D. Franklin, Y. Zhu, Z. Zhang, G.S. Tulevski, J. Tang, W. Haensch, End-bonded contacts for carbon nanotube transistors with low, size-independent resistance, Science. 350 (2015) 68–72. https://doi.org/10.1126/science.aac8006.
[120] T. Weiss, V. Zielasek, M. Bäumer, Influence of Water on Chemical Vapor Deposition of Ni and Co thin films from ethanol solutions of acetylacetonate precursors, Sci. Rep. 5 (2016) 18194. https://doi.org/10.1038/srep18194.
[121] Y. Zhao, J. Wei, R. Vajtai, P.M. Ajayan, E. V Barrera, Iodine doped carbon nanotube cables exceeding specific electrical conductivity of metals, Sci. Rep. 1 (2011) 83. https://doi.org/10.1038/srep00083.
[122] W.M. Haynes, ed., CRC Handbook of Chemistry and Physics (Internet Version 2016), 96th ed., CRC Press/Taylor and Francis, Boca Raton, FL, 2016. http://www.hbcpnetbase.com/ (accessed December 7, 2015).
[123] A.D. Polyanin, A.I. Chernoutsan, A concise handbook of mathematics, physics, and engineering sciences, Taylor & Francis Group, LLC, Boca Raton, FL, 2010. https://doi.org/10.1201/b10276.
[124] J. Alvarenga, P.R. Jarosz, C.M. Schauerman, B.T. Moses, B.J. Landi, C.D. Cress, R.P. Raffaelle, High conductivity carbon nanotube wires from radial densification and ionic doping, Appl. Phys. Lett. 97 (2010) 182106. https://doi.org/10.1063/1.3506703.
[125] R. Sundaram, T. Yamada, K. Hata, A. Sekiguchi, The importance of carbon nanotube wire density, structural uniformity, and purity for fabricating homogeneous carbon nanotube-copper wire composites by copper electrodeposition, Jpn. J. Appl. Phys. 57 (2018) 04FP08-1-4. https://doi.org/10.7567/JJAP.57.04FP08.